$Pr_{1-x}Ca_xMnO_3$ for Catalytic Water Splitting - Optical Properties and In Situ ETEM Investigations

DISSERTATION

zur Erlangung des mathematisch-naturwissenschaftlichen Doktorgrades

"Doctor rerum naturalium"

der Georg-August-Universität Göttingen

———

im Promotionsprogramm ProPhys

der Georg-August University School of Science (GAUSS)

vorgelegt von

Stephanie Mildner (geb. Raabe)

aus Erfurt

Göttingen, 2015

Betreuungsausschuss:
Prof. Dr. Christian Jooss, Institut für Materialphysik
Prof. Dr. Simone Techert, Max-Planck-Institut für Biophysikalische Chemie, Göttingen

Mitglieder der Prüfungskommission:
Referent: Prof. Dr. Christian Jooss, Institut für Materialphysik
Korreferent: Prof. Dr. Michael Seibt, IV. Physikalisches Institut

weitere Mitglieder der Prüfungskommission:
Prof. Dr. Simone Techert, Max-Planck-Institut für Biophysikalische Chemie, Göttingen
Prof. Dr. Cynthia Volkert, Institut für Materialphysik
Prof. Dr. Peter E. Blöchl, Institut für Theoretische Physik, TU Clausthal
Prof. Dr. Hans Hofsäss, II. Physikalisches Institut

Tag der mündlichen Prüfung: 05.08.2015

Contents

List of Figures

CHAPTER 1

General Introduction

1.1 Preface/Motivation

Facing the steadily growing energy demand of our society, the development and establishment of renewable energy sources and methods for energy storage is an urgent need. One pathway is the use of sunlight for electricity generation, e.g. in solar cells. A possibility of storing solar energy via conversion into chemical energy (solar fuels) is offered by the generation of hydrogen via photoelectrochemical water splitting. The overall water splitting reaction according to $2\,H_2O \rightarrow O_2 + 2\,H_2$ involves the water oxidation half reaction, respectively the oxygen evolution reaction (OER), $2\,H_2O + 4\,h^+ \rightarrow O_2 + 4\,H^+$, and the proton reduction half reaction involving hydrogen evolution, $4\,H^+ + 4\,e^- \rightarrow 2\,H_2$. Apparently, the simplest way for realization is direct photocatalytic water splitting where a sunlight absorbing material in contact with an aqueous electrolyte catalyzes both half reactions via transferring the photo-generated electron and hole charge carriers to the catalyst-electrolyte interface (see Fig. 1.1a). However, recombination of photo-excited charge carriers within the photocatalyst and back reactions of the products during the water splitting reaction sequence reduce the hydrogen production efficiency. Hence, it is reasonable to spatially separate the half reactions and the photo-generated charge carrier species. This can be realized in photoelectrochemical cells (PEC)(see e.g. [1]). The simplest type of a PEC, schematically shown in Fig. 1.1b, consists of two electrodes immersed in an aqueous electrolyte, a semiconducting photoanode (photocatalyst) and a metal cathode, which are in electrical contact. Photons are absorbed by the photoanode and electron-hole pairs are generated. The photo-generated hole charges are transferred to the photoanode-electrolyte interface, where they drive the OER, while the photo-generated electrons reduce the remaining protons at the metal cathode surface. In general, the OER represents the rate determining half reaction which limits the overall water splitting efficiency because it requires the transfer of four electron holes to the water molecule. Accordingly, the optimization of the OER is in the focus of current research. [2–5]

Solar driven OER involves several steps: i) the absorption of photons, ii) the transport of the excited carriers to the electrode-electrolyte interface and iii) their transfer to the

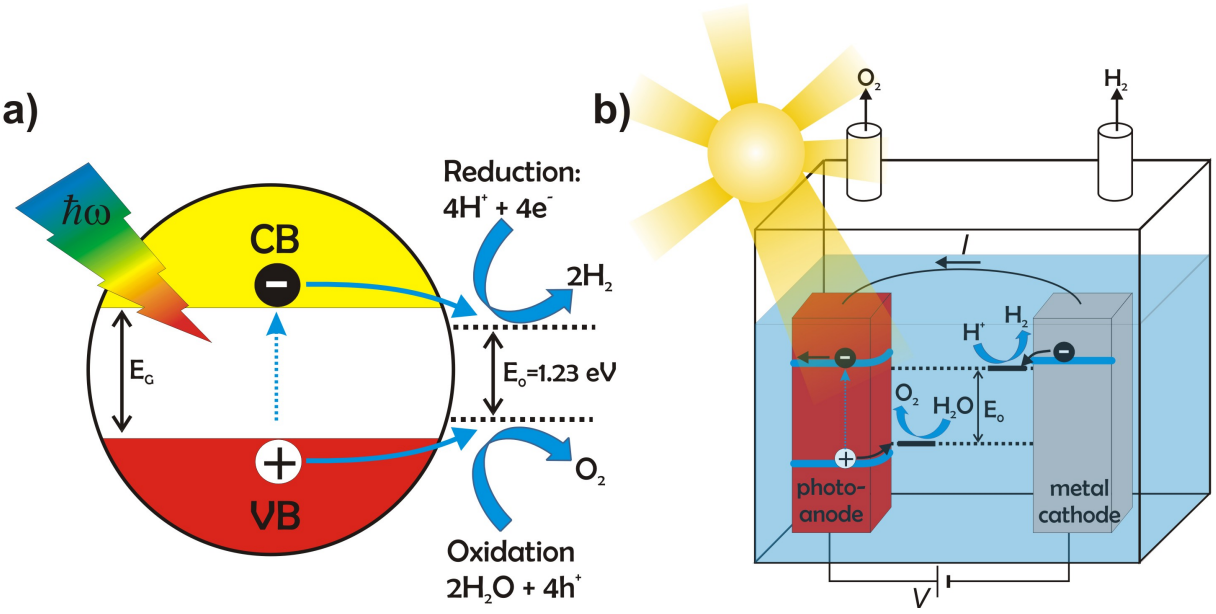

FIG. 1.1 a) Scheme of photocatalytic water splitting with a semiconducting photocatalyst. The absorption of a photon of an energy which is larger than the band gap E_G leads to the excitation of an electron from the valence (VB) to conduction band (CB). The photo-generated electrons and holes are transferred to the water molecules initiating the respective water splitting half reaction. b) Scheme of a photoelectrochemical cell (PEC) with light absorbing semiconducting photoanode and metal cathode including electrode band schemes and redox potentials of water oxidation and proton reduction half reaction.

water molecule (or intermediate {O,H}-species) over an energy barrier which depends on the electronic surface structure of the electrode material in its active state. Each of these steps has to be studied and optimized for achieving high solar to hydrogen conversion efficiencies. Furthermore, the stability of the electrode under working conditions is a major issue since high endurance catalysts are desired for cost-effective and sustainable utilization. Thus, the development of stable high-performance catalyst materials with adequate optical properties for efficient solar light harvesting is in the focus of current research.

During the past decades transition metal based ABO_3 perovskite oxides (with the transition metal occupying the B-site) have attracted scientific interest in the field of solar energy conversion and hydrogen production via (photo)electrochemical water splitting. [2, 3, 6–8] They generally reveal a high thermodynamic stability compared to their non-oxide counterparts. Furthermore, they offer a large playground for scientists because of their high variability: Their fundamental atomic structure allows for combination of various elements via A-site and B-site doping, while their basic lattice distances reveal only weak dependence on the used elements. [9]

In particular, manganese based perovskites (B$\hat{=}$Mn) represent an interesting material class because of the multiple valence states of manganese, which provides high flexibility

in the electronic surface structure of a manganite electrode. Furthermore, the analogy to the natural oxygen evolution complex in the Photosystem II of plants and algae suggests Mn-Ca-O compounds to be very promising electrode candidates for artificial photosynthesis. [10–15]
The charge carriers in manganites reveal strong correlation effects, e.g. the interaction of the charge carrier with the lattice results in the formation of polarons. Their interaction leads to cooperative behavior of the polaron carriers manifesting in long-range charge, orbital and/or magnetically ordered ground states. Due to their low transport mobilities, polaronic charge carriers are often considered to be disadvantageous for photoelectrochemical performance. [16, 17] However, in the natural oxygen evolving Mn-Ca-O cluster the charge transfer is accompanied by structural changes as well (see e.g. [18, 19]). This suggests that the involvement of lattice dynamics at the electrode/electrolyte interface and cooperative behavior of the charge carriers might also have a promoting effect on the coupled 4-hole-transfer to the water molecules during OER. Although strong correlation effects and concomitant features are well-known and frequently studied in manganites, their impact on (photo)electrochemical OER activity and electrode stability is still an open question and needs to be investigated and understood.
The polaron density in manganites can be tuned by A-site doping. Moreover, the nature of the valence and conduction bands and accordingly the character of the polarons i.e., whether dominated by Mn $3d$ or O $2p$ electronic states, strongly depends on the doping level[1]. [22, 23] This allows for a systematic study of the OER activity and electrode stability in dependence of the electronic structure.

In various theoretical works the OER activities of different oxide and perovskite surfaces have been estimated in terms of the potential energies required for the single steps of the 4-electron-transfer. [3,24,25] These works are based on the assumption of a defect-free and invariant surface with the transition metal as the active site where water molecules and intermediates are adsorbed. However, real electrode surfaces undergo structural and electronic modifications in the catalytically active state. [26] These modifications may either be undesired degradation processes reducing the OER activity or forming processes which transform the electrode into its active state. [27] For instance, oxygen vacancies generated at the surface during OER activity may act as docking sites for water adsorption and their generation and annihilation may be involved in the 4 electron-transfer. [28, 29] This requires the respective structural and electronic flexibility of the electrode surface. However, extensive changes in the oxygen stoichiometry (or likewise in the A- or B-site stoichiometry) may also lead to degradation. The tendency to form oxygen vacancies strongly depends on the electronic structure at the upper valence band edge (UVBE).

In situ studies of the electronic structure and defect chemistry at the electrode surface in its active state offer a substantial benefit for a better understanding of electrode stability and capability for OER.

[1] In literature, the properties of manganites are frequently discussed in the framework of a valence and conduction band exclusively formed by Mn $3d$ states and the contribution of O $2p$ states is disregarded. [20, 21]

In particular, analytical environmental transmission electron microscopy (ETEM) studies are of great interest since they enable the atomic-scale observation of atomic and electronic structure modifications at the electrode surface in contact with gaseous electrolyte. The addition of sacrificial substances to the gaseous electrolyte even allows for monitoring OER in the TEM via side reactions with the evolved oxygen. However, in situ TEM studies also pose a challenge concerning the comparability with real working electrochemical cells, e.g. the impact of the low-pressure gaseous electrolyte and the electron beam on OER activity needs to be elucidated.

In the present thesis epitaxially grown thin film electrodes of narrow bandwidth calcium-doped praseodymium-manganite $Pr_{1-x}Ca_xMnO_3$ (PCMO) for OER are investigated. PCMO is chosen as a model system because of the strong electron-phonon interaction, i.e., the charge carriers are small polarons. Thus, it allows to study the impact of strong correlation effects on the photoelectrochemical performance.
This thesis focuses on the following elementary steps which are involved in the operation of a PCMO electrode for OER: (i) The optical absorption behavior of small polarons in PCMO is studied as a function of temperature and electronic structure by varying the doping level (chapter 2, *Phys. Rev. B*, accepted (June 2015)). (ii) The electrochemical OER at PCMO thin film electrodes in contact with water as a function of doping is investigated via conventional cyclovoltammetry and in situ ETEM studies in a gas mixture of $He/H_2O/SiH_4$ ($p_{H_2O} = 3$ μbar) in chapter 3 [*Adv. Funct. Mater.* **22**, 3378-3388 (2012)]. Here, monosilane SiH_4 was used as a sacrificial substance for monitoring OER in TEM. (iii) The role of the electron beam as a driving force for the reactions at PCMO($x = 0.32$) TEM samples is the main subject of chapter 4 [*J. Phys. Chem. C* **119**, 5301-5310 (2015)]. Here, the comparability of conventional and in situ methods is addressed.
The combination of all elementary steps involved in a full photo-catalytic system was outside the scope of this thesis.

1.2 Scientific Background

1.2.1 Properties of $Pr_{1-x}Ca_xMnO_3$

Ca-doped $PrMnO_3$ is a perovskite manganite where the mismatch of the ionic radii[2] provokes a tilting of the MnO_6 octahedral units. This octahedral tilting leads to an orthorhombic structure with doping dependent mean Mn-O-Mn bonding angles of 152-157° and lattice parameters of $a = 5.3 - 5.44$ Å, $b = 5.3 - 5.62$ Å, $c = 7.5 - 7.64$ Å(in *Pbnm* space group). [30] The Mn-O-Mn bonding angle strongly affects the orbital overlap between the Mn-sites and the oxygen sites and, accordingly, has a considerable impact on the electronic structure and the transport and magnetic properties of PCMO. [31]

The electronic structure near the Fermi energy is dominated by Mn $3d$ and O $2p$ hybrid states. The octahedral Mn-O configuration leads to crystal-field splitting of the 5 Mn $3d$

[2]The Goldschmidt tolerance factor is $t \sim 0.94$ for PCMO $x = 0.3$.

states into 3 t_{2g} and 2 e_g states. Due to strong Hunds coupling these states are occupied in high-spin configuration, i.e. 3 t_{2g} electrons and $(1-x)$ e_g electrons with parallel spin per MnO_6-site. In undoped $PrMnO_3$ the oxidation state of the Mn-sites is 3^+ and each MnO_6 unit contains one e_g electron. With Ca^{2+}-doping x electron holes are accumulated within the e_g states leading to an increase of the average Mn oxidation state. In $CaMnO_3$ ($x = 1$) the e_g states are empty and the Mn oxidation state is 4^+.
Owing to the Jahn-Teller (JT) effect the occupation one of the two e_g orbitals results in an octahedral distortion, i.e. an elongation along the axis of the occupied e_g orbital and a compression in direction of the unoccupied e_g orbital. [32–36] The elongation is accompanied by a reduction of the Coulomb repulsion between the Mn e_g and the O-ligand electron which provokes an additional splitting of the e_g states (and to smaller extent also of the t_{2g} states). As the e_g occupation is highest in undoped $PrMnO_3$, the JT effect is most pronounced for $x = 0$ resulting in a cooperative ordering of the distorted octahedra (orbital ordering) as well as in the formation of an electronic band gap of the order of 1-2 eV. The latter provokes an optical absorption band in the VIS/NIR range (see e.g. [37,38]. The depletion of e_g states via hole doping x weakens the JT effect i.e, for $x = 1$ the distortion of the octahedra and the related e_g splitting vanishes.

The JT effect represents an example for the strong electron-lattice correlation and polaron formation governing the properties of PCMO and other perovskite manganite compounds. A polaron is defined as a quasi-particle consisting of an electron coupled with a cloud of phonons, i.e. the surrounding atoms are shifted from their equilibrium positions. [39,40] In turn, the modification of the surrounding lattice generates a potential well which reduces the electron transport mobilities in polaronic crystals. Depending on the electron-lattice interaction range and coupling strength polarons are distinguished in large and small polarons. If the interaction is long-range and the coupling is weak a large polaron is formed, i.e. the lattice distortion extends over several lattice sites. In contrary, the extension of the potential well of a small polaron, which forms as a result of strong short-range electron-lattice interaction, is in the range or smaller than the characteristic lattice spacing, i.e. the electron is trapped at a single lattice site. [40–43]. Whereas for large polarons the spread of the potential well allows for band-like transport with metal-like $\rho(T)$ characteristics in a wide temperature range, small polarons move incoherently at elevated temperatures from one localized site to another by thermally activated hopping. [42,44]. Small polaron motion at low temperatures occurs via coherent tunneling. In PCMO the charge carriers are small polarons with hopping conductivity in a wide doping range. [45]

In manganites, the presence of strong polaron-polaron interactions gives rise to various cooperative ordering effects and collective behavior based on the electronic, lattice and spin degrees of freedom. The magnetic and electronic transport properties are correlated due to superexchange and double exchange: (i) The super exchange describes the spin dependent transfer of electrons between nearest-neighbor Mn sites with equal integer valence state, e.g. the exchange of electrons in the lower JT split e_g orbitals of a Mn^{3+}-Mn^{3+}-pair. [46–48] It promotes antiferromagnetic (AFM) coupling of neighboring

Mn-sites (in a near 180° Mn-O-Mn bond), because the antiparallel spin configuration enables the electron transfer between neighboring Mn-sites with equal electronic configuration, i.e. both either unoccupied or occupied with one e_g electron, respectively. Such electron transfer is inhibited for parallel spin alignment because of Pauli exclusion principle. Thus, the antiparallel next neighbor spin configuration leads to a gain of kinetic energy which is proportional to the orbital overlap integral J.[3] Notably, the kinetic energy gain due to the super exchange between Mn^{3+} sites competes with the enhanced on-site Coulomb energy U due to the twofold e_g occupation of a Mn-site.
(ii) The double exchange predominantly concerns the intermediate hole doping range because it describes the spin dependent electron transfer within a pair of neighboring Mn-sites accommodating one e_g electron, i.e. a Mn^{3+}-Mn^{4+}-pair[4]. [49–51] If the coupling of the Mn-sites is ferromagnetic, the e_g electron can hop between the Mn sites via electron exchange with the enclosed O $2p$ orbital. This leads to a kinetic energy gain without the expenditure of additional Coulomb energy U (as in the case of super exchange). Thus, the double exchange promotes ferromagnetic spin coupling.

Based on the described exchange mechanisms the transport and magnetic properties are correlated with each other. Since the electrons also interact with the crystal lattice, the magnetic and electronic degrees of freedom are coupled with the structural and orbital degrees of freedom. Accordingly, depending on the polaron density (doping level), the tolerance factor, the orbital overlap integral J and the temperature various long-range ordered or disordered phases with different crystalline symmetries, magnetic structures and electronic properties are observed in doped manganite systems. For instance, in manganites with large Mn-O-Mn bonding angles, i.e. large orbital overlap J, such as $La_{0.67}Sr_{0.33}MnO_3$, the double exchange provokes a ferromagnetic ground state phase with metallic-like transport behavior. [52]
In contrast, PCMO reveals strong octahedral tilting and small orbital overlap J. The phase diagram of $Pr_{1-x}Ca_xMnO_3$ is presented in Fig. 1.2a). It shows orbital ordering (OO) in a wide temperature range at $x < 0.28$ and charge ordering (CO) at low temperatures for $0.28 < x < 0.9$. [30, 53] The stability of a CO ground state in the intermediate doping range can be understood in the framework of the double exchange mechanism which suggests the maximum kinetic energy when two neighboring Mn-sites share one e_g electron, i.e. at half doping. Long-range magnetic ordering of these spin aligned Mn-couples may be either ferromagnetic or antiferromagnetic due to superexchange. In PCMO doping dependent ferromagnetic and antiferromagnetic ordering is observed at low temperatures.[5]

[3] The super exchange may also provoke may also weak ferromagnetic coupling of Mn-sites depending on the Mn-O-Mn bonding angle (e.g. a Mn-O-Mn 90° corner) and the involved e_g orbitals. The preferred ground state magnetic coupling type for the various structural Mn-O-Mn arrangements and orbital occupation of the two JT split e_g orbitals can be predicted with the Goodenough-Kanamori-Anderson rules. [32]

[4] Note, hybridization with the $2p$ orbitals of the enclosed oxygen may weaken the 3+/4+ valence separation in a mixed valent Mn-pair (see below).

[5] Notably, while there are many publications on hole doped PCMO ($x \leq 0.5$) the Ca-rich compounds are scarcely studied which might be due to the reduced thermodynamic stability of the $CaMnO_3$

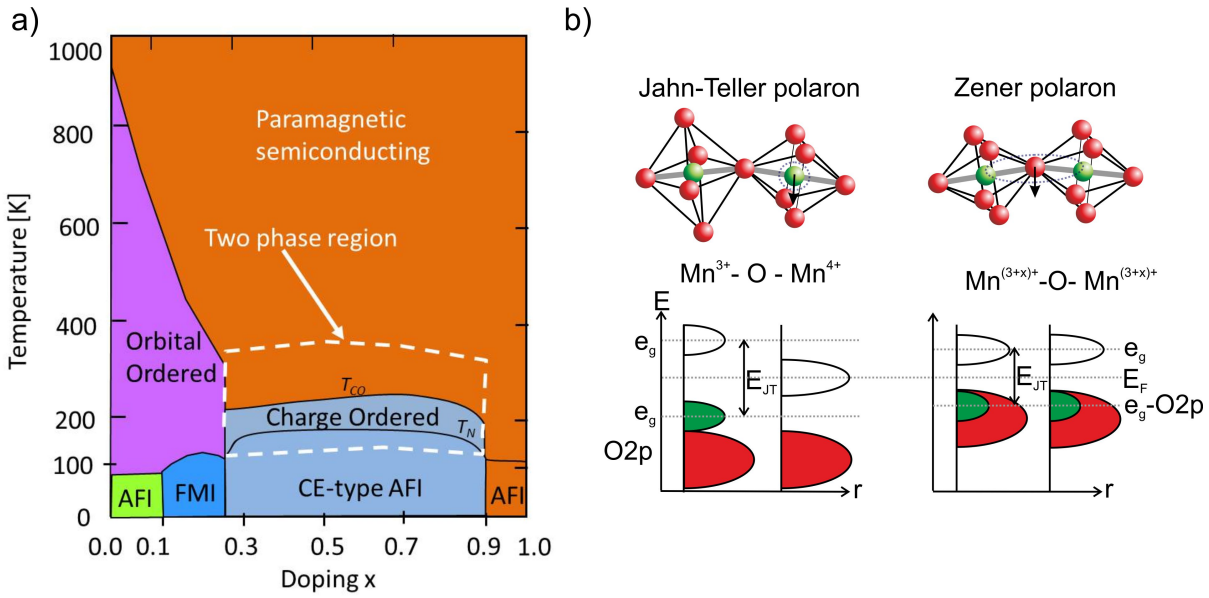

FIG. 1.2 a) Phase diagram of PCMO according to Ref. [30] revealing orbital ordering below T_{OO} for $x < 0.28$ and charge ordering below T_{CO} for $0.28 < x < 0.9$ with different magnetic ordering and electronic behavior like ferromagnetic insulating (FMI) and antiferromagnetic insulating (AFI). For $0.28 < x < 0.9$ the thermal phase transition between charge ordering and and the disordered paramagnetic semiconducting phase is smeared out over a wide temperature range where both phases coexist in spatially separated domains. The temperature range of phase separation is indicated by the white dashed box. The magnetic ordering in this doping range is CE-type antiferromagnetism below the Neel temperature T_N. b) Structural and electronic band scheme of the Jahn-Teller polaron (left) with mixed valent Mn sites and an Mn e_g dominated UVBE and of the Zener polaron (right) with equivalent Mn sites and an UVBE formed by O $2p$-e_g hybrid states.

The emerging ground state phase is determined by a subtle balance of competing phases. A perturbation of this balance by external stimuli such as electric or magnetic fields, light and pressure can induce phase transitions between ordered and disordered phases with pronounced changes in the charge carrier mobility. For instance, magnetic fields can melt the CO phase in PCMO and induce a highly conductive phase with metallic-like transport characteristics. [55] Furthermore, Fiebig et al. have shown that a laser pulse of $\lambda = 1000$ nm can induce a huge resistance drop in biased PCMO single crystals which persists until the electric field is switched off. [56]

A-site doping with Ca^{2+} offers the opportunity to control the atomic and electronic structure of PCMO in terms of tuning the polaron density, the octahedral tilting, the impact of the Jahn-Teller effect and the emerging ground state phases. [30] In addition, the degree of O $2p$ and Mn $3d-e_g$ orbital intermixing at the UVBE and, correspondingly, the electronic states involved in the small polaron formation depend on the doping level. While the UVBE in $PrMnO_3$ has significant Mn $3d-e_g$ contribution, $CaMnO_3$ is

boundary phase. [54]

classified as a charge-transfer insulator with an UVBE formed by O $2p$ states. [23]. Thus, doping allows for systematic studies of the impact of atomic and electronic structure modifications and, to some extent, for optimization of the properties of a PCMO-based electrode for (photo)electrochemical water splitting.

In recent literature, two limiting pictures of small polarons are discussed for PCMO ($x = 0.3, 0.5$) concerning the electronic character of the polaron or, respectively, the site where the small polaron is localized (Fig. 1.2b): (i)The Jahn-Teller polaron is localized at the Mn-site and hole doping leads to mixed valent Mn oxidation states, i.e. a coexistence of JT-distorted Mn^{3+} and undistorted Mn^{4+} ions. This picture implies an ionic Mn-O bonding, i.e. the O $2p$ states are fully occupied with 6 electrons and hole doping concerns only the Mn $3d$-e_g states. Accordingly, this approach involves that the UVBE is formed by Mn e_g states without significant contribution of O $2p$ states [57–59]. (ii) A covalent contribution to Mn-O bonding and the presence of O $2p$ states at the UVBE weakens the effect of Mn valence separation or even annul it, if the UVBE is solely formed by O $2p$ states. This case describes the Zener polaron where the doped hole charge is located in Mn-O-Mn dimers with ferromagnetically coupled Mn- sites of equivalent oxidation state $(3 + x)+$. The Mn-O-Mn bond is flattened within these dimer which leads to an enhanced overlap J of the Mn e_g orbitals with the interjacent O $2p$ orbital benefiting the double exchange. [60–63] The presence of Zener polaron dynamics in PCMO ($x = 0.5$) is experimentally confirmed by Wu and and Jooss et al. [60, 64]
.
Polaron formation and JT splitting has also a considerable impact on the optical properties of PCMO and other manganites. The optical excitation of polarons provokes an optical absorption in the NIR/VIS photon energy range allowing for light harvesting within the intensity maximum of the solar spectrum. The shape of the NIR/VIS absorption is characteristic for the polaron type. While small polaron absorption provokes an absorption peak at $\hbar\omega \sim 2E_P$ (E_P is the polaron formation energy), large polaron optical absorption reveals a Drude-like feature in the IR range. [59] Photon-assisted small polaron hopping is commonly considered in the framework of Holsteins two-site model. [40, 65] This will be dealt with in more detail in chapter 2. Here, the selection rules with respect to $d-d$ - transitions provoking the NIR/VIS absorption in manganites shall be shortly addressed:

Photons have an angular momentum. The absorption of a photon requires energy and momentum conservation. In the classical approach this can be understood in terms of an alternating electromagnetic field interacting with polarizable matter. The *ac*-field can only interact with the matter by inducing an electric dipole moment, i.e. changing the polarization in the matter. The probability of electronic transitions due to photon absorption depends on the symmetry properties of the involved electronic wave functions. This is described by the selection rules. While the electron spin must be conserved in the electronic transitions the angular momentum transfer on photon absorption requires a parity change between the initial and the final state. Parity conserving electronic excitations due to absorption of dipole radiation are forbidden by the dipole selection rule

(In centrosymmetric molecules, such as MnO_6 octahedra, this is also called the Laporte rule. [66]) In the quantum mechanical approach, an electronic transition is dipole-allowed if the corresponding transition matrix element $\int \psi_i^* \, \hat{\mu} \, \psi_f \, d\vec{r}$ does not vanish, i.e. the integrand $\psi_i^* \, \hat{\mu} \, \psi_f$ must have even symmetry. Since the transition momentum operator $\hat{\mu} = q\vec{r}$ has odd symmetry, the wave functions of the initial and the final state ψ_i and ψ_f, respectively, must have different symmetries. [67,68] Thus, $d-d$ transitions in octahedral compounds involving just odd electronic wave functions such as transitions between JT split states of e_g symmetry, are formally forbidden. However, intersite transfer transitions in crystals with reduced symmetry, e.g. by octahedral tilting, and/or the coupling to phonon modes of even symmetry (which cancel the inversion center in the octahedral units at least temporarily) weaken the rigor of the Laporte rule and $d-d$ transitions are visible in optical absorption spectra of manganites. Moreover, orbital intermixing with the p-orbitals of the oxygen ligands or rather electronic transitions involving a charge transfer between the Mn $3d$ orbitals and the O $2p$ ligand orbitals cancel the pure $d-d$ -like character. [69, 70]

Due to its favorable optical absorption properties in combination with the opportunity to control the structural and electronic properties by the doping level allowing for the adjustment to the OER redox potentials, PCMO seems to be a promising candidate for photocatalytic water splitting. The negative aspect of polaron formation in PCMO for the OER concerning the reduced charge carrier mobility may to some extent be counterbalanced by opportunity to induce phase transitions by external stimulation into phases with higher transport mobilities. [55, 56], In addition, the coupling of lattice dynamics to a photo-excited electronic state may lead to the formation of a metastable excited polaron state with presumably enhanced the lifetime. Moreover, the benefit of coupled electron-lattice dynamics is proven in the natural OER complex in the Photosystem II where the change of oxidation state of the manganese ions in the Mn-O-Ca cluster accompanying proton release is coupled with a change of the Mn-O bond length (see e.g. [18,19]).

1.2.2 Perovskite Oxides for Oxygen Evolution Reaction

Photoelectrodes for efficient solar driven OER have to fulfill the following requirements: (i) Semiconductor photoanodes with small band gaps < 2 eV are advantageous for efficient harvesting of sunlight since the solar spectrum has maximum intensity in the visible light range at $\sim$2.4 eV. Photoelectrodes like TiO_2, WO_3 and $SrTiO_3$ which are commonly used because of their high corrosion stability reveal band gaps of $E_g > 3$ eV. [71,72] Thus, their performance is limited by the optical absorption which is less than 10% of the sunlight. (ii) Photo-excited carriers with a long lifetime and high transport mobilities are desired in order to achieve high transfer rates to the electrode/electrolyte interface before they are trapped or recombined. (iii) The electronic structure of the photoelectrode in its active state has to fit the respective redox potentials for enabling the transfer of the excited carriers across the interface (see Fig. 1.1). For OER involving the transfer of four excited hole carriers, this requires that the UVBE lies energetically

below the water oxidation potential. The overall water splitting reaction requires a thermodynamic potential energy of 4.92 eV which implies a minimum energy of 1.23 eV per hole transfer (in case of an ideal catalyst) and limits the band gap of the photoelectrode to $E_g > 1.23$ eV. However, experiments as well as potential energy calculations of the individual reaction steps of the OER cycle have shown that a certain overpotential η is required for driving the OER. [3, 24, 25]
The overpotential is defined by $\eta = V - V_0$, i.e. the difference between the experimentally observed potential V and the thermodynamically required potential V_0. The overpotential describes the kinetic inhibition of the OER, e.g. due to insufficient diffusion of electrolyte reactants and products, retarded adsorption and electron transfer or formation of stable intermediates. [73] Hence, the required overpotential η must be provided either by the band gap of the photoelectrode or by an applied external electric potential.
The overpotential required for driving OER at a certain electrode surface is commonly used as a measure of the electrode performance, i.e., low η are desired for efficient OER. Typical values are $\eta \sim 0.4$ eV for a current flow of $j \sim 1$ mA/cm^2 across the electrode/electrolyte interface. Another quantity, which is frequently used to characterize the OER activity, is the exchange current density j_0. It describes the charge transfer rates at the at the thermodynamic OER potential V_0. High exchange currents constitute high-performance electrodes for OER. Both quantities, η and j_0, can be measured by conventional cyclovoltammetry. A detailed description of this method can be found in [73].

For perovskite oxide electrodes in alkaline electrolyte (pH > 7) the B-site is usually considered as the active surface site for OER, where the adsorption of OH-molecules leads to a reduction of symmetry breaking at the surface (see Fig 1.3a). On the basis of the redox-active B-site, the 4-step OER cycle has been elucidated in several experimental and theoretical studies of different doped and undoped perovskite oxide electrodes.[6] For instance, early investigations by Bockris et al. in 1984 combine experimental cyclovoltammetry with theoretical calculations of the potential energy of the individual reaction intermediates. [3] Recently, density functional theory (DFT) calculations have been performed in order to analyze OER at well established oxide catalysts (RuO_2, IrO_2 and TiO_2) by Rossmeisl et al. [24] and perovskite oxide catalysts by Man et al. [25] The experimental work by Suntivich et al. covers numerous doped and undoped perovskite compounds including manganites. [2] The key objective of these studies is to identify a universal descriptor allowing for prediction of the catalytic activity of a certain perovskite oxide electrode.

The individual reaction steps of the OER cycle involve the formation and subsequent reactions of {O,H}-intermediates, which are bound to the B-site with different bonding strengths. Accordingly, the energy barriers governing the individual reaction steps differ from the average thermodynamic potential of 1.23 eV per hole transfer. The step with the highest energy barrier (the rate-determining step) determines the required reaction overpotential and the minimum band gap of the photoelectrode for OER.

[6] These works consider electrochemical OER where ground state hole carriers are transferred from the conduction band (in solar driven OER, optically excited holes are transferred from the valence band)

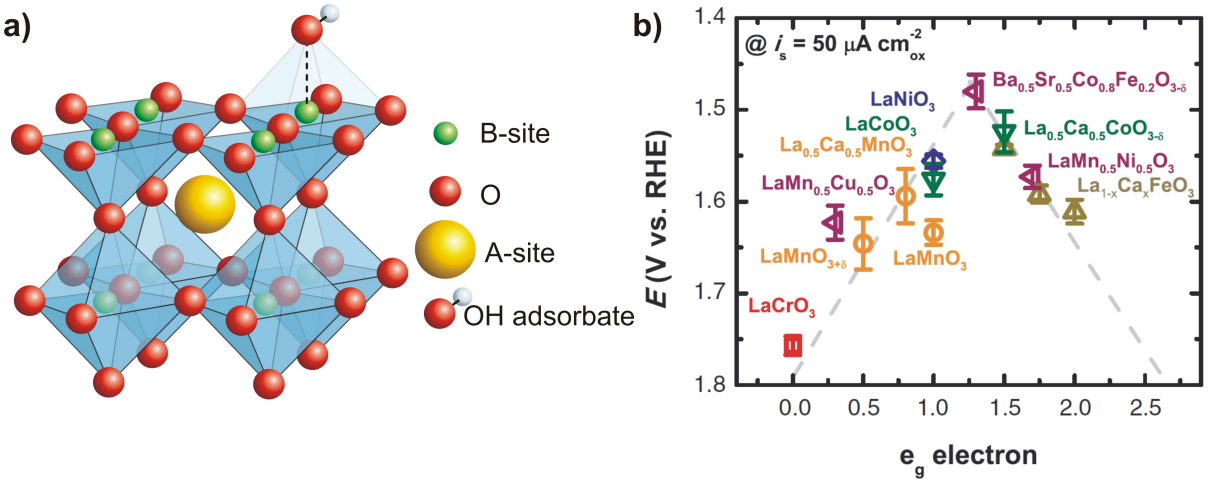

FIG. 1.3 a) Scheme of an OH adsorbate on a perovskite surface assuming the B-site as the redox-active site. According to molecular orbital theory the bonding of an OH molecule to a surface B-site is energetically favored because of the symmetry enhancement due to the recovery of the (bulk-like) BO_6 octahedral configuration instead of a BO_5 pyramidal surface configuration. b) Volcano-shaped trend of the overpotential as an indicator for oxygen evolution activity taken from Ref. [2].

In the studies mentioned above a strong correlation between the strength of B-{O,H} bond and the OER activity as well as the electrode stability has been observed. [2,3,24,25] The OER activity as a function of the bonding strength between {O,H}-species and the B-site exhibits a volcano-shaped curve: In case of weak B-O bonding the {O,H}-adsorption and bonding to the surface is the rate-determining step. Concomitantly, the thermodynamic stability of the perovskite lattice decreases with decreasing B-O-bond strength and the electrode becomes susceptible to corrosion. [3] On the other hand, too strong B-O bonding forms a barrier for subsequent reaction steps and hinders the desorption of the product. On the basis of molecular orbital theory, Bockris et al. relate the B-O bond strength to the occupation of anti-bonding d states, i.e. the higher the occupation of anti-bonding states, the lower the bonding strength. Advancing the work by Bockris et al., Suntivich et al. consider the enhanced influence of the $3d - e_g$ states[7] due to their σ-bonding to the oxygen anions. They found that the occupation of the e_g orbitals represents a universal descriptor for OER activity with highest activity at an e_g occupation close to unity (Fig. 1.3b).

In the OER reaction cycle proposed by Rossmeisl et al. and Man et al. and adopted by Suntivich et al. the sequential formation of diverse B-{O,H} intermediates involves changes of the oxidation state of the B-site, e.g. $B^{(m+1)+} - O^{2-} + OH^- \rightarrow B^{(m)+} - OOH^- + e^-$. [2, 24, 25] This requires the respective flexibility of the electronic surface structure of the electrode without leading to electrode degradation.

[7] Crystal field splitting in an octahedral metal-ligand configuration leads to a lift of degeneracy of the d states and an electronic level splitting into π-type t_{2g} and σ-type e_g electronic orbitals.

Although Bockris and Suntivich consider the surface B-ions as the active sites, they recognize a correlation between the OER activity and the degree of covalency in the B-O bond, i.e. a higher contribution of O $2p$ states to the UVBE enhances OER activity. Recent results by Mueller et al. even reveal that oxygen anions are the active surface sites for OER in many transition metal oxides. The authors suggest that oxygen vacancy formation and incorporation play a key role for OER activity and electrode stability. [29]

1.2.3 In Situ Environmental Transmission Electron Microscopy Studies of Electrodes for OER in their Active State

Ideally, catalysts for water splitting just mediate electron transfer between hydrogen and oxygen species without being directly involved in the OER cycle. However, real electrodes always undergo changes in their active state in terms of surface modifications of their electronic and atomic structure or even chemical composition. These modifications may either represent a forming process leading to surface activation or degradation leading to a deactivation of the electrode. In order to obtain a better understanding of the processes proceeding at the electrode surface during OER, in situ studies of the active state on atomic scale are required.

Recent methodical development and improvement of electron microscopy techniques enable the investigation of electrodes in contact with water with atomic resolution: Generally, the spatial resolution of TEM is related to intrinsic imperfections of electron lenses, e.g. spherical and chromatic aberrations. Aberration correction via utilization of C_S-image correctors improves spatial resolution at beam energies of 300 keV to 0.8 Å. [74–79] Owing to the development of differential pumping systems (Fig. 1.4) the study of electrodes in gaseous electrolytes with pressures up to several millibars while bearing up ultra high vacuum at the electron source is possible in environmental transmission electron microscopes (ETEM). [80,81] ETEM with scanning capability in combination with electron energy loss spectroscopy (EELS) and/or energy-dispersive X-ray spectroscopy (EDX) allows for investigating local chemical and electronic changes of electrode materials under working conditions. [82,83] With Schottky-type field emission guns and the utilization of monochromators an energy resolution of 0.18 eV can be achieved for EELS at electron beam energies of 300 keV. Moreover, specifically designed TEM sample holders allow for in situ investigation of specimens under optical, electrical or thermal stimulation. [84–89] Additionally, the injection of sacrificial gas species into the gaseous electrolyte in the ETEM enables the visualization of the studied chemical reaction, e.g. the monitoring of OER via SiO_2 growth from reaction of the evolved oxygen with sacrificial SiH_4 presented in the chapters 3 and 4.

However, along with the mentioned benefits in situ ETEM studies also imply a significant challenge in terms of the comparability with conventional methods. First, high energy electrons impinging a specimen may cause knock-on damage, i.e. atomic displacements or even desorption of lattice atoms. The extent of knock-on damage is determined by

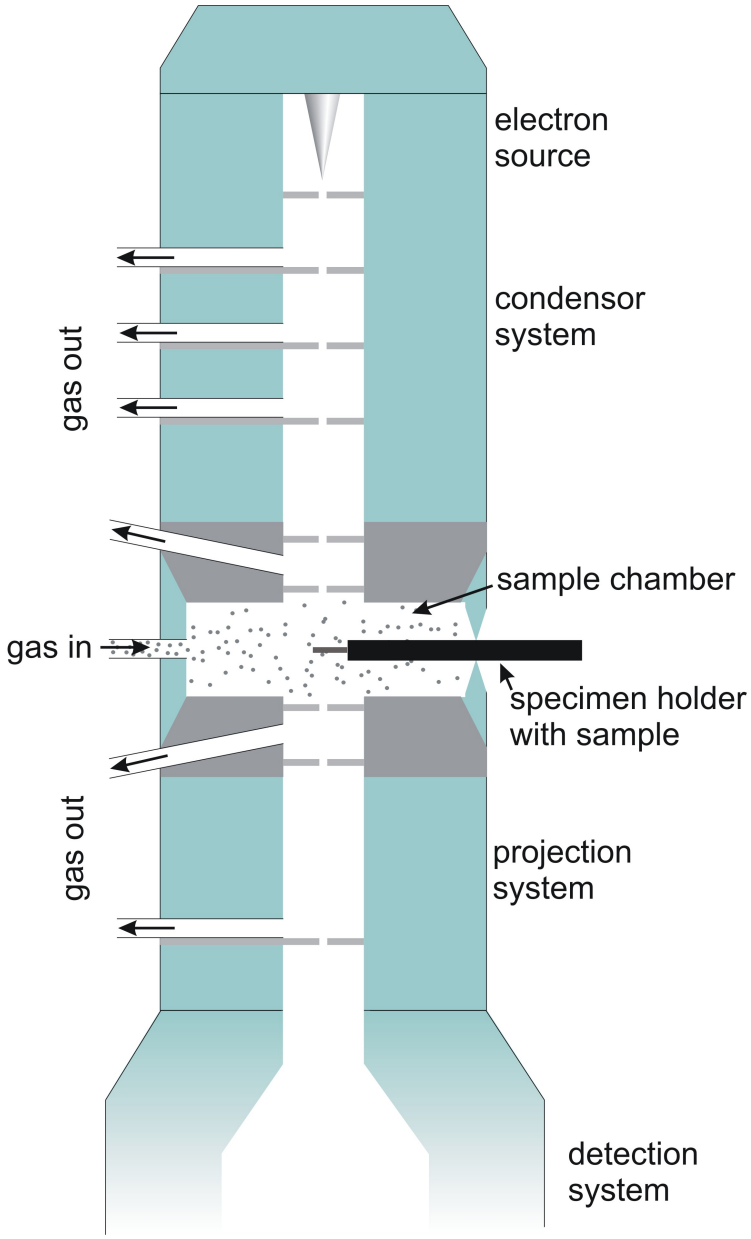

FIG. 1.4 Scheme of a differentially pumped TEM with several apertures along the optical axis allowing for maintaining a pressure gradient between the gun and the specimen chamber of up to 11 orders of magnitude.

the balance of the excitation of atomic displacements and the respective relaxations. It depends on the beam electron energy, flux and the thermodynamic stability of the TEM specimen. [90, 91] Thus, its impact can be minimized under low energy and/or low electron flux TEM conditions. PCMO turned out to be stable under 300 keV electron exposure with electron fluxes up to 10^4 $e/(\text{Å}^2\text{s})$ in high vacuum.

However, even at low electronic dose conditions the beam electrons interact with the spec-

imen, transferring energy during inelastic scattering events, e.g. electron back-scattering, plasmon and core level excitations, electron-hole pair generation, specimen heating, Auger processes, ionization or, respectively, secondary electron emission. [92] Thus, an understanding of the impact of the electron beam on the electrochemical behavior of the electrode and the gaseous electrolyte is necessary: The emission of secondary, Auger and core electrons from the specimen induces positive charges in the sample[8]. [93] In insulating samples or samples which are not sufficiently connected to ground the accumulation of positive charges induces a positive electric potential which is able to drive electrochemical reactions in the ETEM. The quantification or even control of such beam induced potentials is of high interest, but also a great challenge. A theoretical calculation of the beam induced potential in a PCMO ($x = 0.35$) TEM specimen on the basis of the secondary electron yield as well as a semi-experimental way to determine the potential via off-axis electron holography combined with electrostatic modeling are given Chapter 4.

Moreover, the reaction kinetics is likely to be different under ETEM conditions in gaseous electrolytes at pressures in the millibar range compared to conventional experiments in liquid electrolytes. Although a thin layer of liquid water is likely to deposit on the surface of the TEM specimen in water vapor environment, a significant pressure dependence of the reaction rate is expected since, according to the Nernst equation, the electrode redox potential depends on the concentration of gaseous {O,H}-species. [73]

[8] In thick specimens the absorption of beam electrons has to be considered as a source of negative charge injection. This effect can be disregarded in thin specimens.

CHAPTER 2

Temperature and Doping Dependent Optical Absorption in the Small Polaron System $Pr_{1-x}Ca_xMnO_3$

S. Mildner, J. Hoffmann, P. E. Blöchl, S .Techert and C. Jooss
Phys. Rev. B, accepted for publication on 12 June 2015
http://journals.aps.org/prb/accepted/a207dO1cP091792b16a9789604eae4a5d4927318e

ABSTRACT Small polaron optical properties are studied comprehensively in thin film samples of the narrow bandwidth manganite $Pr_{1-x}Ca_xMnO_3$ by optical absorption spectroscopy as a function of doping and temperature. A broad near infrared double-peak absorption band in the optical conductivity spectra is observed and interpreted in the framework of photon-assisted small polaron intersite hopping and on-site Jahn-Teller excitation. Application of quasiclassical small polaron theory to both transitions allows an approximate determination of polaron specific parameters like the polaron binding energy, the characteristic phonon energy as well as the Jahn-Teller splitting energy as a function of temperature and doping. Based on electronic structure calculations, we consider the impact of the hybridization of O $2p$ and Mn $3d$ electronic states on the Jahn-Teller splitting and the polaron properties. The interplay between hopping and Jahn-Teller excitations is discussed in the alternative pictures of mixed valence Mn^{3+}/Mn^{4+} sites (Jahn-Teller polaron) and equivalent $Mn^{(3+x)+}$ sites (Zener polaron). We give a careful evaluation of the estimated polaron parameters and discuss the limitations of small polaron quasiclassical theory for application to narrow bandwidth manganites.

2.1 Introduction

Polarons, i.e. quasi-particles composed by electronic charge carriers and phonons, are a key transport feature in doped manganites. Many properties of manganites such as hopping-like electric transport behavior, [94, 95] charge ordering, [60, 64] as well as colossal resistance effects [55, 96, 97] involve polaronic effects. [98, 99] A polaron forms as a consequence of a significant charge-lattice interaction, i.e. the electric charge carrier distorts its surrounding lattice resulting in the formation of a potential well. In the case of a small polaron this potential well localizes the charge carrier at a single lattice site. [43] A large polaron forms if the lattice distortion spreads over several lattice sites. [40, 42, 100]

Optical absorption spectroscopy in the near-infrared (NIR) region allows studying the properties of polaron excitations. [59, 101–103] For example, Quijada et al. investigated the temperature dependent optical properties of $La_{2/3}Ca_{1/3}MnO_3$, $La_{2/3}Sr_{1/3}MnO_3$ and $Nd_{2/3}Sr_{1/3}MnO_3$ thin films. These compounds undergo a temperature driven metal-insulator phase transition which is accompanied by a huge spectral weight transfer in the NIR range. [59] The authors observed that phases with small polaron hopping conductivity involve an absorption maximum at $\hbar\omega_{max} \approx 1-2$ eV. Phases with metal-like conductivity reveal a Drude-like feature in the infrared range, which is interpreted in the framework of large polaron transport. Similar trends in the cross over from small to large polaron optical absorption are observed by Hartinger et al. [101]
Okimoto et al. presented temperature dependent optical conductivity spectra of low bandwidth $Pr_{1-x}Ca_xMnO_3$ ($x = 0.4$) single crystals up to photon energies of $\hbar\omega \leq 1.2$ eV obtained from NIR reflectivity data. [20] Their data indicate a broad absorption feature around $\hbar\omega \approx 1$ eV which was interpreted in terms of intersite $d-d$ transfer transitions of the charge carriers. Evidence for small polaron absorption in $Pr_{1-x}Ca_xMnO_3$ ($x = 0.33$) is presented by Saucke et al. in pn manganite hetero-junctions. [104]

Commonly, the NIR optical conductivity of manganites are interpreted in the framework of transition between Mn $3d$ states where O $2p$ states near the Fermi level are not considered. [20, 105] However, recent literature proves that O $2p$ states are involved in NIR optical excitation. [69] Moreover, studies of the electronic structure of manganites reveal a strong contribution of O $2p$ states to the upper valence band edge. [28, 60, 106–108]
Among the numerous studies on the optical properties of manganites, systematic studies of the doping dependence are rare. [22] Moreover, despite the recognition that the NIR absorption in manganites carries polaron signature, [59, 101] analytical expressions for the optical conductivity of polarons provided by polaron theory, for instance in Ref. [109] and [110], are rarely applied to experimental data. To our knowledge, the only works in which polaron theory was used to fit optical spectra of manganites and extract polaron properties are the Refs. [101, 102, 111] and [112]. However, a sNote that q denotes the relative distortion of both sitesystematic study of the temperature and doping dependence of polaron properties is not provided in these works.

In order to systematically study the temperature and doping dependent optical properties of small polarons, which are formed out of a O $2p$ - Mn $3d$ (e_g) hybrid band, we present temperature dependent optical conductivity spectra as well as *dc* conductivity data of $Pr_{1-x}Ca_xMnO_3$ (PCMO) thin films in the doping range of $0 \leq x \leq 0.8$. The polaronic nature of the double peak excitation in the NIR is analyzed by quasiclassical small polaron theory. This allows for the approximate determination of the temperature and doping dependent polaron binding energy and the involved phonon energies. The observed double peak structure is discussed and interpreted in the framework of intersite polaron hopping transitions and on-site Jahn-Teller (JT) like excitations. Electronic structure calculations are presented which allow for discussion of electronic band structure effects on polaron excitation, in particular the effect of hybridization of oxygen $2p$ and manganese $3d$ states at the upper valence band edge. We critically discuss the applicability of quasiclassical

small polaron theory and derive conclusions on the coupled electron-lattice dynamics in manganites which may initiate further time resolved experimental studies.

2.2 Experimental

Epitaxial PCMO thin films ($x = 0 - 0.8$) were prepared by reactive ion-beam sputtering on single crystalline (001)-oriented MgO-substrate. Sputter targets of the selected compositions ($x = 0, 0.2, 0.35, 0.5, 0.8$) were fabricated by a solid state reaction from stoichiometric mixtures of the dry Pr_6O_{11}, $CaCO_3$, and Mn_2O_3 powders. Repeated milling and calcining lead to pure perovskite phases as revealed by X-ray diffractometry Finally, PCMO targets are cold-pressed and sintered in air at 1370 K for 48 h. The ion-beam sputtering process is performed in a gas mixture of xenon as working gas and oxygen as reactive gas with partial pressures of 10^{-4} mbar at a deposition temperature of 750 °C. The thin film samples with the doping levels $x = 0.2, 0.35$ and 0.5 have been post-annealed in air at temperatures of 800 °C ($x = 0.35, 0.5$) for 10 h and 1000 °C ($x = 0.2$) for 1 - 2 h. The thin films have a thicknesses of $t = 100 - 150$ nm. All samples with $x < 0.8$ reveal epitaxial growth with preferential (001)-orientation as well as (110)-orientation due to twinning. In contrast, the sample with $x = 0.8$ shows (112)-oriented growth on MgO under the same deposition conditions.

Temperature-dependent two-point resistance measurements are performed with a source voltage of 1 V using a closed cycle compressed Helium cryostat. For colossal magnetoresistance (CMR) measurements a Physical Properties Measurement System (PPMS) from Quantum Design is used. Field cooled resistance $R(T)$ is measured in an applied magnetic field of $B = 9$ T. The subsequent $R(T)$ heating curve is measured in zero field.

Temperature-dependent optical absorption measurements were performed in a Cary Varian 5e spectrometer with unpolarized light in a wavelength range of 250 - 3300 nm at temperatures between $T = 80$ K and $T = 300$ K. To provide temperature control the thin film samples were installed in an Oxford Fast track Microstat H2 gas flow cryogenic system cooled with liquid nitrogen. The absorption of the MgO substrate was subtracted via reference measurements of a blank substrate. The real part of the optical conductivity is determined from the measured absorption coefficient $\alpha(\omega)$ via $\sigma(\omega) = \varepsilon_0 c_0 \alpha(\omega)$ in the limit of optically dense thin films $t << c_0/n\omega$, where c_0 is the light velocity and n the refractive index. This approximation is particularly fulfilled in the NIR range.

We performed density-functional calculations [113, 114] with the projector augmented wave method as implemented in the CP-PAW code package [http://www2.pt.tu-clausthal.de/paw/]. [115] We used a local hybrid density functional, [116–118] where a fraction of the exchange in the PBE functional is replaced by an explicit Fock term. [119] The factors are 0.1 for Ca, Mn and O atoms and 0.15 for Pr. For the Mn d states this amounts to a screened U-parameter of 2.3 eV and a screened J-parameter of 0.1 eV. In the local approximation, the exchange correction is limited to the onsite terms in a local

orbital basis set.

2.3 Quasiclassical Theory of Small Polaron Hopping

The polaron state is commonly described by three coupling parameters α, λ, and γ which compare the energy scales of the electron-phonon coupling energy g, the phonon vibrational energy $\hbar\omega_0$ and the electron kinetic energy D. [120]

$$\alpha \equiv \frac{g}{\hbar\omega_0} = \sqrt{\frac{E_P}{\hbar\omega_0}},\ \lambda \equiv \frac{E_P}{D},\ \text{and}\ \gamma \equiv \frac{\hbar\omega_0}{J} \tag{2.1}$$

Small polarons are formed if the electron-phonon coupling energy g is larger than the energy of the involved phonon mode $\hbar\omega_0$ and the polaron binding energy E_P is larger than the kinetic energy D of the electrons ($2D$ denotes the electronic bandwidth), i.e. $\lambda \geq 1$. Both conditions are fulfilled in the low bandwidth manganite PCMO in zero magnetic field. [55] The adiabaticity parameter γ indicates whether the coupled electron-lattice dynamics is governed by the electron motion (adiabatic; $\gamma \to 0$) or by the lattice vibration (anti-adiabatic; $\gamma \to \infty$).

Small polaron motion is commonly discussed in the framework of the simple Holstein two-site model (Fig. 2.1) which describes a single electron in a molecule consisting of two equivalent lattice sites where the electron can hop between the two sites. In the strong coupling limit $\gamma > 1$, the electron-lattice interaction leads to a reorganization of the electronic energy levels and a lattice distortion at the occupied site. The distortion is described by the configurational coordinate q_i which characterizes the antisymmetric relaxation of the two sites. It has the value -1 and +1 if the polaron is formed on the left or right site, respectively. In the symmetric state ($q_1 = q_2 \equiv 0$), the electronic states on the two sites are degenerate. A finite electronic overlap integral $J > 0$ between the two sites lifts the degeneracy at $q_1 = q_2 \equiv 0$ by a splitting energy of $2J$. For a 3-dimensional crystal, the tight binding theory relates the overlap integral J and the electronic band width $2D$ via $J = D/Z$. In an octahedral environment the number of nearest neighbor sites is $Z = 6$.

Within the framework of the quasiclassical Holstein model, the polaron dynamics is approximated by a combination of quantum-mechanical electron dynamics and a classical vibrational field. In the adiabatic limit, the temperature-dependent resistivity due to thermally activated small polaron hopping is [103]

$$\rho(T) = \rho_0 \cdot T \cdot \exp\frac{E_A}{k_B T} \tag{2.2}$$

The activation energy E_A is related to the polaron binding energy and the transfer integral. [100]

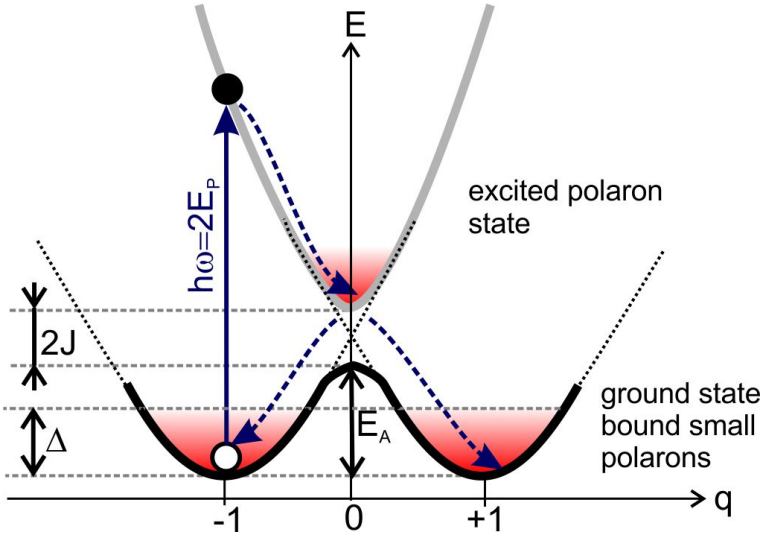

FIG. 2.1 Scheme of small polaron excitations presented in the framework of the two-site model in the adiabatic limit using parabolic potential surfaces to visualize a Franck-Condon like excitation at $\hbar\omega \approx 2E_P$ and two relaxation channels, leading to either hopping transfer or on-site relaxation. At low temperatures, the broadening of the electronic levels Δ is determined by zero-point phonon fluctuations. The potential energy of such two-site system is determined by the electronic energy gain $E_{el} \propto -g \sum f_i q_i$ (where f_i denotes the occupation of site i, $\sum f_i = 1$) and the energy expended for the distortion of the lattice $E_{dist} \propto +\hbar\omega_0 \sum q_i^2$ [Y. A. Firsov and E. K. Kudinov, Phys. Solid State 43, 447-457 (2001)]. Hence, the potential energy at each site as a function of q_i is described by parabolic potential curves depending on the occupation $0 \leq f_i \leq 1$ of the one-electron orbital. Note that q denotes the relative distortion of both sites.

$$E_A = \frac{1}{2}E_P - J \tag{2.3}$$

Figure 2.1 also illustrates the Franck-Condon-like (adiabatic) excitation of a bound small polaron from its ground state. [65] The ground state is broadened due to phonon fluctuations with the energy variance Δ. If the electronic overlap integral is small so that $D = Z \cdot J << \Delta$ is fulfilled (Eq. 2.6), the optical excitation of a small polaron requires twice the polaron binding energy E_P. From the excited state the polaron may relax to ground state either on-site or to a nearest neighbor site, resulting in a hopping transfer.

The quasiclassical theory on the basis of the Holstein model also provides analytical expressions for the frequency-dependent intraband absorption of polarons. [40, 109, 110] In the adiabatic regime, the real part of the frequency dependent optical conductivity of noninteracting small polarons is given by [Eq. 29 in Ref. [109], see also Refs. [40,110,121]]

$$\sigma(\omega, T) = \sigma(0, T) \cdot \frac{\sinh(2\hbar^2\omega_{max}\omega/\Delta^2)}{2\hbar^2\omega_{max}\omega/\Delta^2} \exp\left[-\frac{(\hbar\omega)^2}{\Delta^2}\right] \tag{2.4}$$

i.e., the absorption reveals a skewed Gaussian peak with a maximum at $\hbar\omega_{max}$. The

prefactor $\sigma(0,T)$ is the electrical *dc*-conductivity arising from phonon-assisted polaron hopping motion. Eq. 2.4 requires that the width of the absorption peak is governed by the phonon induced broadening Δ of the involved energy levels,

$$\Delta^2 = 8E_P E_{vib} \tag{2.5}$$

i.e., the effect of the electronic bandwidth $2D$ is small ($D << \Delta$). At zero-point temperature the vibrational energy E_{vib} corresponds to $E_{vib} = \hbar\omega_0/2$. In the high temperature regime ($kT >> \hbar\omega_0$) E_{vib} is equal to the thermal energy, i.e. $E_{vib} = kT$. A rough estimate for PCMO based on $\hbar\omega_0 = 40 - 70$ meV [122, 123] and $2D \sim 850$ meV (Sec. 2.5) gives $0 << \gamma < 1$, i.e. γ is near the adiabatic to antiadiabatic crossover and, thus, non-adiabatic effects have to be considered.
However, dynamical mean field calculations (DMFT) for small polaron optical conductivity show that small polaron absorption gives rise to an absorption peak in the NIR with an absorption maximum at [110]

$$\hbar\omega_{max} = \begin{cases} 2E_P, & \text{for } \Delta >> D \text{ (validity range of Eq. 2.4} \\ 2E_P - \frac{D^2}{2E_P}, & \text{for } \Delta << D \end{cases} \tag{2.6}$$

as long as $\gamma < 1$. Thus, corrections due to finite bandwidth effects have to be taken into account. In particular, E_P as obtained from Eq. 2.4 corresponds to the lower limit of the actual polaron binding energy.

2.4 Results

2.4.1 Temperature Dependent Electrical Resistivity and Optical Absorption

Figure 2.2 and 2.3 give a brief overview on the temperature and doping dependence of the electrical and optical conductivity. The electrical resistance of the undoped $PrMnO_3$ film is too high for a suitable measurement with our electrical setup. Therefore, only $\rho(T)$-measurements for $0.2 \leq x \leq 0.8$ are presented in Fig. 2.2a.
With increasing doping level the resistivity decreases. Moreover, the $\rho(T)$-trends are consistent with thermally activated hopping polaron transport behavior (Eq. 2.2). Since the activation barrier significantly changes with the onset of charge ordering and accordingly with temperature, the apparent temperature dependent activation energy is plotted in Fig. 2.2b. [55] The almost temperature independent behavior of $E_A(T)$ for $T > 200$ K and $0.2 \leq x \leq 0.5$ is characteristic of thermal activated hopping of small polarons.
The samples with $x = 0.35$ and $x = 0.5$ exhibit a pronounced CMR when a magnetic field of $B = 9$ T is applied (see inset of Fig. 2.2a). As shown in Ref. [55], the occurrence of a CMR and the presence of an ordering peak in the $E_A(T)$-characteristics at $T \sim 170 - 200$ K is an indication for the presence of the charge and orbital ordered (CO/OO) phase at

temperatures $T < 200$ K in zero magnetic field. Note that the activation energies are not very different for the hole-doped samples but significantly lower for the nominally electron-doped sample with $x = 0.8$.

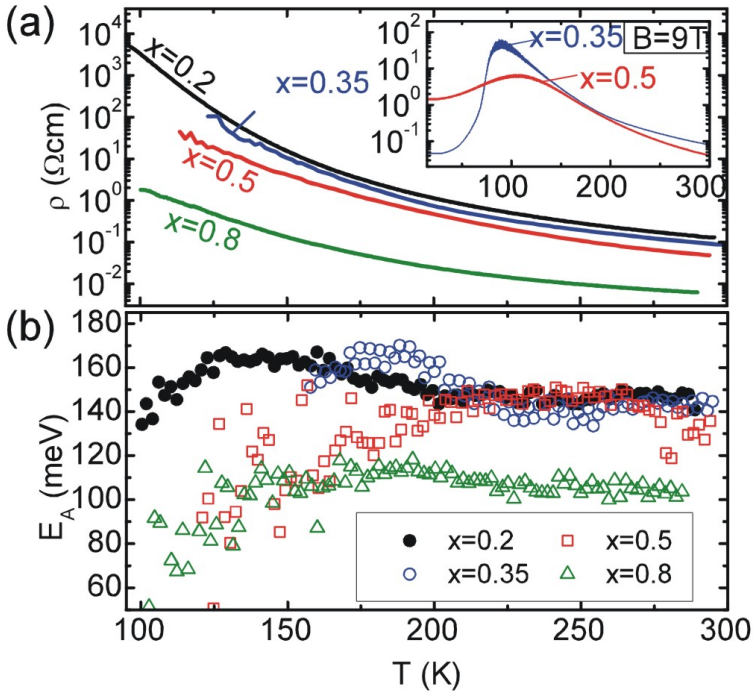

FIG. 2.2 a) Temperature dependent resistivity of PCMO $0.2 \leq x \leq 0.8$ shows insulating behavior in the whole temperature and doping range. The sample for $x = 0.35$ and $x = 0.5$ exhibit a pronounced CMR (inset) at $B = 9$ T. b) The apparent activation energies calculated from resistivity via Eq. 2.2 within finite temperature intervals of 3 K. The almost temperature-independent apparent energy at temperatures above 200 K gives the activation barrier in the paramagnetic charge-disordered state.

Figure 2.3 presents the real part of the optical conductivity $\sigma(\omega)$ at room temperature and at $T = 80$ K for the PCMO films ($x = 0 - 0.8$). For $x = 0$ we observe at least three absorption bands in the measured photon energy range: One band (labeled (B)) with small spectral weight centered at $\hbar\omega_{max} \approx 2.5$ eV and two bands (C) and (D) at $\hbar\omega > 4$ eV, i.e. in the ultraviolet (UV) range. The feature (C) appears as a weak shoulder at the low energy tail of the intense feature (D). In the doped PCMO samples ($x \geq 0$) an additional absorption band (A) appears in the NIR range. We denominate the features (A) and (B) (blue curves in Fig. 2.3b-e) as NIR transitions and the features (C) and (D) (red curves in Fig. 2.3) as UV transitions. With increasing doping level all absorption features exhibit a pronounced shift to lower photon energies. Furthermore, the spectral weight of the UV transitions seems to increase with doping level. For $x = 0.8$ the absorbance is huge for photon energies $3.5eV < \hbar\omega < 6$ eV and out of the detector range.

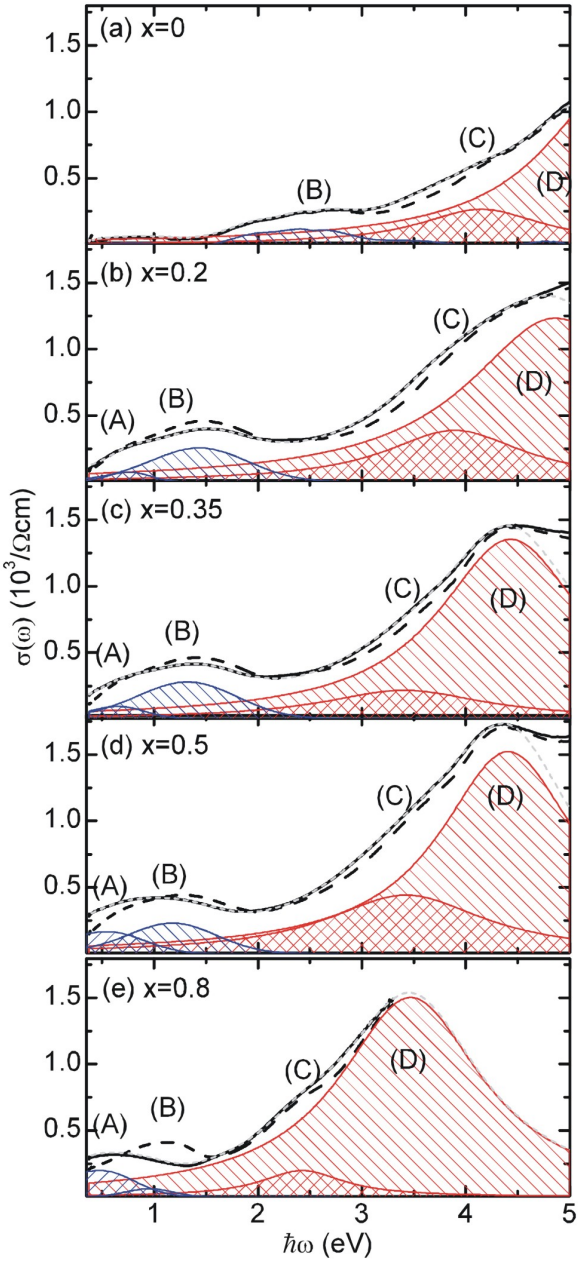

FIG. 2.3 Optical conductivity of PCMO films for increasing doping level from $x = 0$ (a) to $x = 0.8$ (e) measured at $T = 300$ K (solid black line) and $T = 80$ K (dashed black line). The red hatched curves (peaks (C) and (D)) and blue hatched curves (peaks (A) and (B)) designate fit results from application of small polaron theory Eq. 2.4 to peaks (A) and (B) an Lorentzian functions to peaks (C) and (D), respectively. In the spectra b) - e) the sums of the fit curves are illustrated by the light-gray dashed lines.

Since the polaronic nature of charge carriers emerges predominantly in the low photon energy range, we focus our investigations on the NIR transitions. However, for a reliable analysis of these transitions we have to subtract the spectral weight arising from the

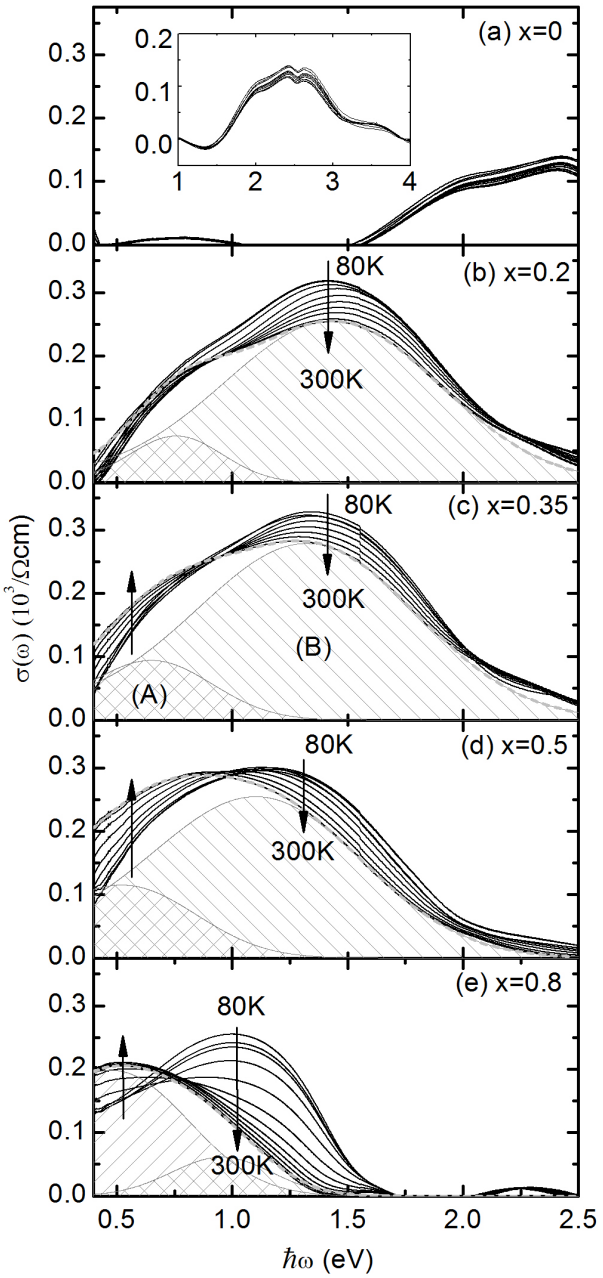

FIG. 2.4 Temperature dependence of the optical conductivity for increasing doping level from $x = 0$ (a) to $x = 0.8$ (e) after subtraction of UV absorption bands. Temperature variations from 80 K to 300 K are indicated by arrows. The inset in a) shows the whole spectral range of the NIR feature for $x = 0$. The additional marginal absorption at 0.8 eV may originate from defect states. This feature will not be considered in the following discussion. Hatched Gaussian shaped areas represent the fit of peak (A) and (B) at room temperature according to Eq. 2.4. The light-gray dashed line is the sum of the fit curves.

UV transitions which partly overlap the NIR features. For this purpose we fit Lorentz oscillator functions to the bands (C) and (D) (see Fig. 2.3). Quantitative analysis of the fit parameters derived from Lorentz fitting of the UV features has to be handled

with care because further absorption bands at higher energies, i.e. above the measured spectral range, may contribute to the spectral weight in the UV range. Thus, we restrict our analysis and discussion of the UV absorption bands to a few qualitative arguments in the Sec. 2.7 of this article.

Figure 2.4 shows the optical conductivity $\sigma(\omega)$ at various temperatures after subtraction of the UV absorption bands. The temperature dependence of the NIR absorption is negligible for $x = 0$. For $x \geq 0.2$ we observe a slight transfer of spectral weight to lower energies with increasing temperature. The transferred spectral weight increases with increasing doping level which for $x = 0.8$ is embodied by a pronounced redshift of the NIR absorption.

2.4.2 Application of the Quasiclassical Small Polaron Theory to NIR Absorption Bands

As mentioned in the introduction, we assume that the NIR features correspond to intraband and interband transitions of small polarons. Since both are expected to be phonon-assisted and the fundamental nature and shape of polaron interband and intraband transitions are very similar, [44, 124, 125] we use the quasiclassical model for small polaron intraband absorption, i.e. Eq. 2.4, for the fitting of both NIR peaks.

The temperature dependence of the excitation energies, i.e. the photon energies of the maximum absorption $\hbar\omega_{max}$ are illustrated in Fig. 2.5. Both peak positions exhibit similar temperature trends, i.e. a decrease with increasing temperature and a maximum at low temperatures ($T \approx 170$ K), which seems to shift to lower temperatures with increasing hole doping. Note that for the hole-doped samples $\hbar\omega_{max}^{(A)} \approx 1/2\ \hbar\omega_{max}^{(B)}$ at room temperature. We have, therefore, plotted $\hbar\omega_{max}^{(A)}(T)$ and $1/2\hbar\omega_{max}^{(B)}(T)$ in Fig. 2.5.

In the framework of the applied quasiclassical model (Eq. (2.4), the peak width Δ of polaron absorption feature is related to the vibrational energy E_{vib} of the involved phonon mode (c.f. Eq. 2.5). The temperature dependence of E_{vib} determined from the fit results via Eq. 2.5 is depicted in Fig. 2.6 for both NIR absorption peaks. The vibrational energies for hole doped PCMO ($x \leq 0.5$) are roughly constant at temperatures $T < \Theta_D/2 \sim 150$ K, i.e. below half of the Debye temperature Θ_D, and increase almost linearly with temperature for $T > \Theta_D/2$. Some deviations from this simple behavior are observed for $x = 0.2$ below 120 K. However, the most striking difference is the entirely different temperature dependence observed for the sample with $x = 0.8$.

Figure 2.7 summarizes the doping dependence of the fitting parameters, i.e. the excitation energy at room temperature (Fig. 2.7a), the low-temperature vibration energy at 80 K (Fig. 2.7b) and the spectral weights at room temperature (Fig. 2.7c). Since the applicability of the semi-classical model on the nominally electron doped sample ($x = 0.8$) is questionable (see also Sec. 2.5.1), we have marked the fitting parameters of

this sample by parentheses.

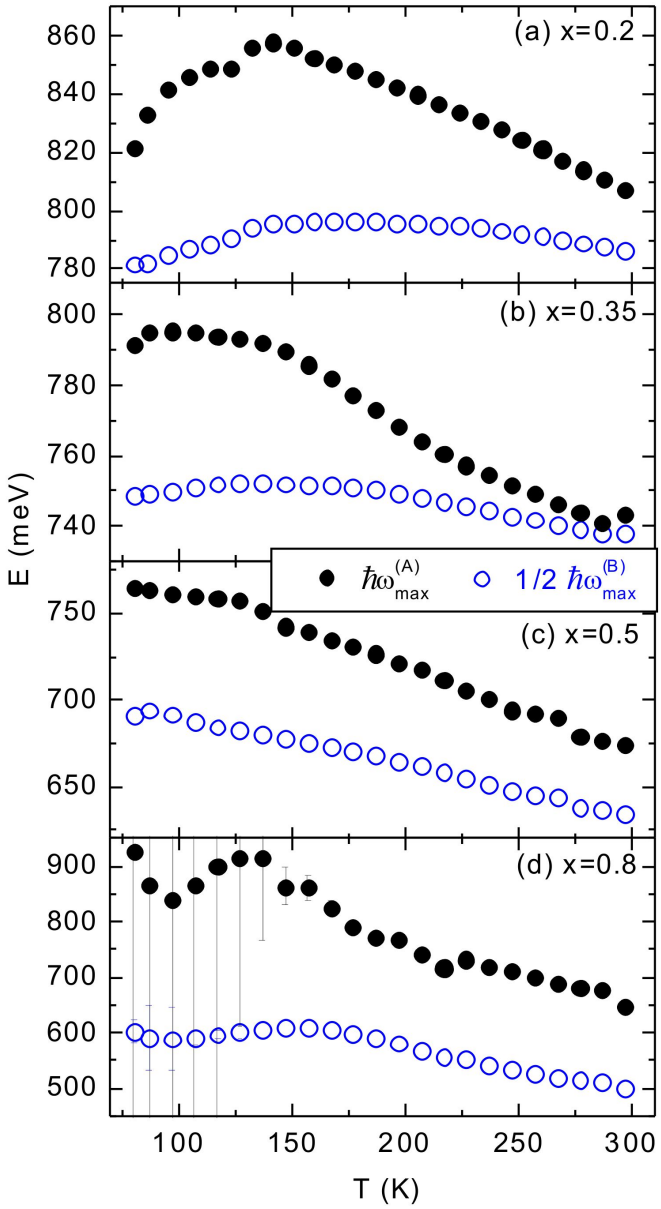

FIG. 2.5 Temperature dependence of the excitation energies $\hbar\omega^{(A)}_{max}(T)$ (solid symbols) and $1/2\ \hbar\omega^{(B)}_{max}(T)$ (open symbols). The error bars representing the fit error are included only if they are larger than the symbol size.

For the sample with $x = 0$ we assign the absorption feature ranging from 1.5 eV to 4 eV (Fig. 2.4a) to the peak (B), i.e. we expect that transitions related to peak (A) are absent (for justification, see Sec. 2.5.1). We, therefore, derive the spectral weight (SW) via integration over the optical conductivity in the energy range $1.5eV < \hbar\omega < 4$ eV, i.e.

$SW^{(B)} = \int \sigma(\omega)\, \mathrm{d}\omega$ and $SW^{(A)} = 0$. Note that the doping dependence of the spectral weights of both NIR features is very different, $SW^{(B)}$ exhibits a maximum at x = 0.35 whereas $SW^{(A)}$ increases with doping x.

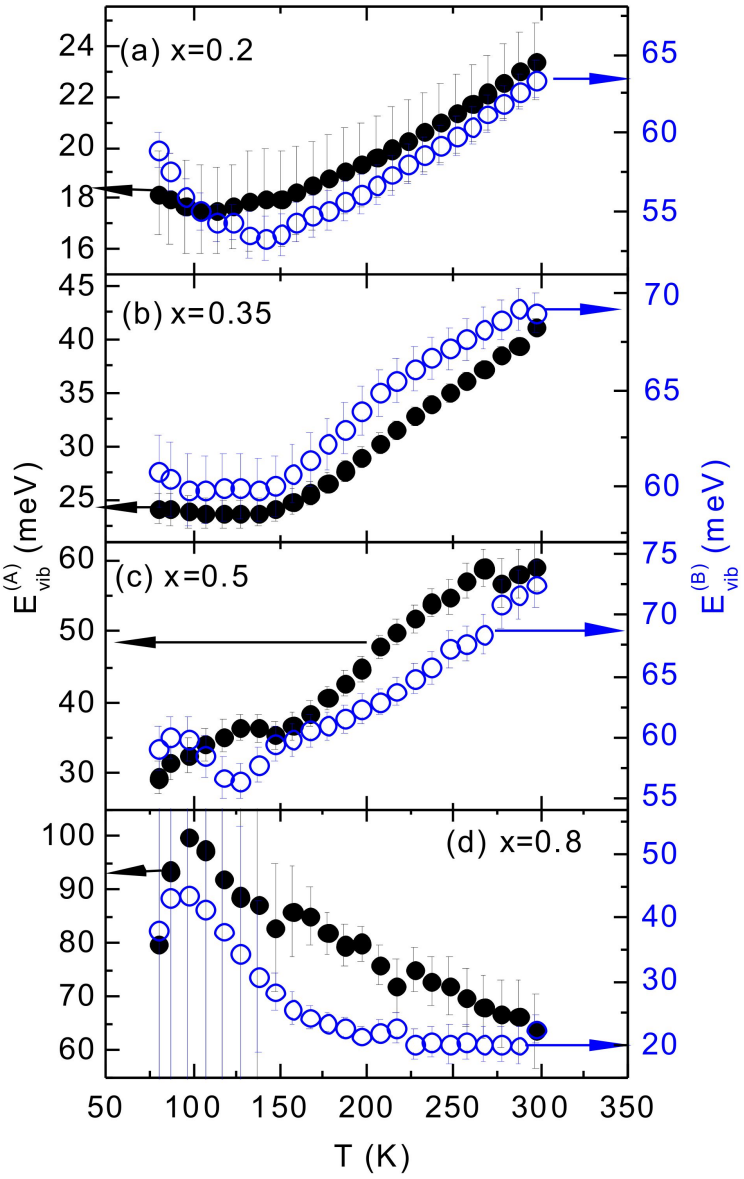

FIG. 2.6 The vibrational energies $E_{vib}^{(A)}(T)$ (solid symbols) and $E_{vib}^{(B)}(T)$ (open symbols) as a function of temperature for $x = 0.2 - 0.8$ calculated via Eq. 2.5. The significance of the fitting results is reduced for 0.8 because a substantial part of the absorption band (A) is outside the measured spectral range. Especially, the fitting of the low temperature spectra of $x = 0.8$ yields large error bars because peak (A) and (B) shift together hampering their separation in the fitting procedure.

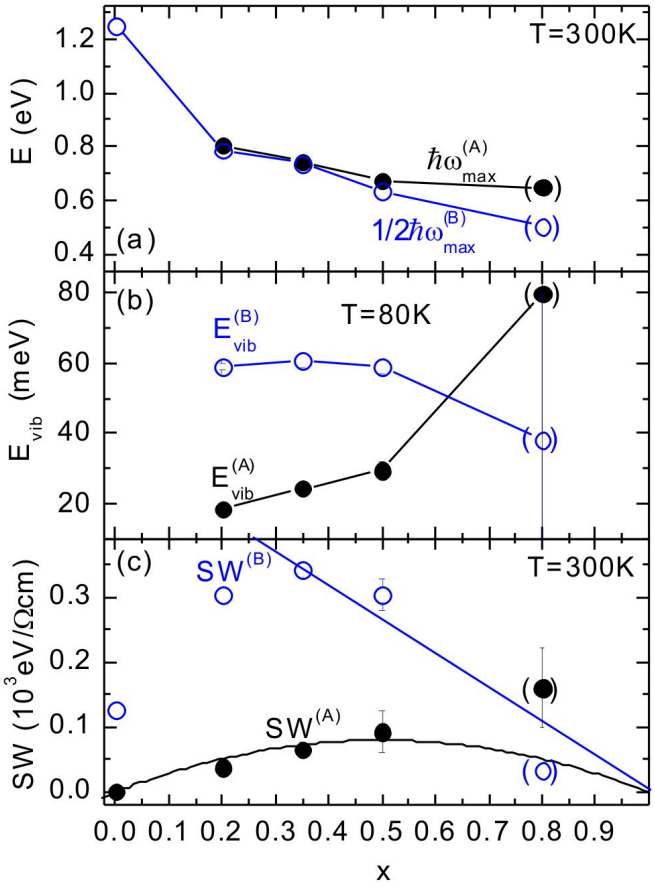

FIG. 2.7 Doping dependence of a) $\hbar\omega^{(A)}_{max}$ and $1/2\,\hbar\omega^{(B)}_{max}$ at room temperature and b) $E^{(A)}_{vib}$ and $E^{(B)}_{vib}$ obtained via fitting feature (A) (solid symbols) and feature (B) (open symbols). The value of $1/2\,\hbar\omega^{(B)}_{max}$ for $x = 0$ is deduced from the spectral center of gravity of the NIR band and the parameters for $x = 0.8$ are put in parentheses (see explanation in the text). c) Doping dependence of the spectral weights of peak (A) (solid symbols) and (B) (open symbols) at room temperature. The black line and the blue lines in c) represent theoretical doping dependencies according to $\sim x(1-x)$ and $\sim (1-x)$, respectively. These relations will be considered in Sec. 2.5. The errors of the spectral weights are estimated by the spectral weight of the respective peak fit which is outside the measured spectral range, i.e. the fit area below the measurement threshold of 0.38 eV. In a), b) and c) the error bars are only shown if they exceed the symbol size.

The onset energies $E^{(A)}_{onset}$ and $E^{(B)}_{onset}$ of peak (A) and (B) are extracted via linear extrapolation of the low energy shoulder of the fit curves according to Eq. 2.4. This is shown exemplarily for $x = 0.35$ in Fig. 2.8a. In doped PCMO samples the onset energy of peak (A) corresponds to the optical gap. The temperature dependence of the optical gap is shown in Fig. 2.8b. For $x = 0.2$ an optical gap $E^{(A)}_{onset} > 0$ appears in the entire temperature range and exhibits only a weak temperature dependence. For $x \geq 0.35$ the optical gap at room temperature is small or even disappears in case of $x = 0.5$ and $x = 0.8$. Whereas an optical gap is absent in the whole temperature range for $x = 0.8$, it reveals a strong temperature dependence in case of $x = 0.35$ and $x = 0.5$. For $x = 0.5$ we observe a

gap opening at $T \approx 200$ K. The onset energy $E_{onset}^{(B)}$ of peak (B) at $T = 80$ K as a function of doping level is shown in Fig. 2.8c. For $x = 0$ we obtain $E_{onset}^{(B)}$ via linear regression in the energy interval 1.6 eV $\geq \hbar\omega \geq$ 1.8 eV of the spectrum shown in Fig. 2.4a. Just as the optical gap, the onset energy $E_{onset}^{(B)}$ reveals a strong doping dependence, i.e. it drastically decreases between $x = 0$ and $x = 0.5$ and slightly increases again for $x = 0.8$.

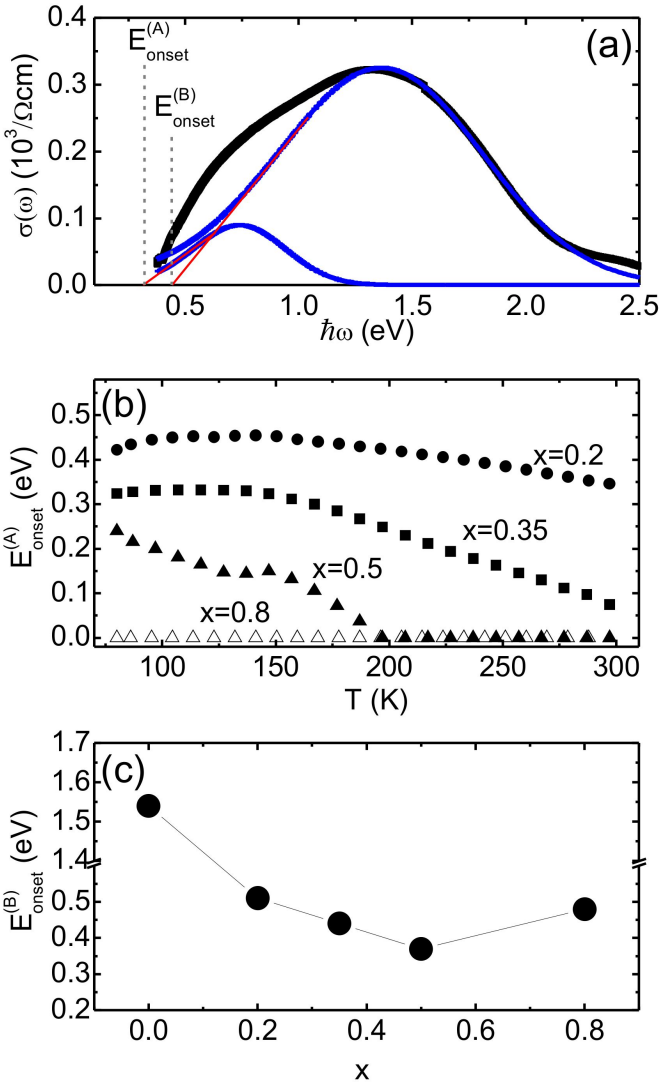

FIG. 2.8 a) Determination of the onset energies $E_{onset}^{(A)}$ and $E_{onset}^{(B)}$ via linear extrapolation of the low energy shoulder of fit curves. b) $E_{onset}^{(A)}$ as a function of temperature for $x \geq 0.2$. c) The doping dependence of $E_{onset}^{(B)}$ at $T = 80$ K. Error bars are smaller than the symbol size.

2.5 Discussion

In the investigated doping and temperature range the optical absorption spectra of PCMO reveal typical small polaron signature, i.e. peak-shaped NIR absorption bands

and the absence of large polaron characteristics in terms of a Drude-like absorption feature. [59,101] In addition, the resistivity reveals the typical properties of small polaron mobility and, thus, the application of quasiclassical small polaron theory (Eq. 2.4) in order to describe the NIR transitions seems to be reasonable. In accordance with our results, Jung et al. find two absorption bands in the NIR range of polycrystalline $La_{1-x}Ca_xMnO_3$ single crystals which they attribute to polaron hopping between Mn^{3+} and Mn^{4+} sites and on-site JT transitions at the Mn^{3+} sites. [22]

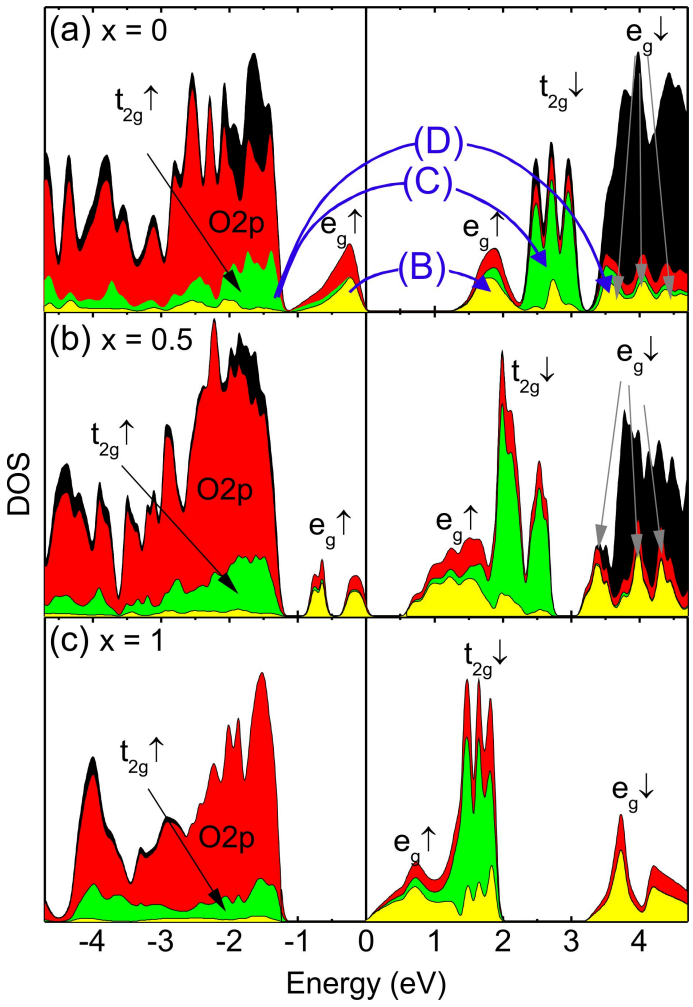

FIG. 2.9 Band structure PCMO for $x = 0$ (top), $x = 0.5$ (middle) and $x = 1$ (bottom) presented as staple diagram. It reveals oxygen states (red areas) and manganese states (t_{2g} - green and e_g - yellow) near the Fermi energy. The total DOS including Pr/Ca states is illustrated in black. The blue arrows in the band structure for $x = 0$ (top) indicate the optical transitions associated with peak (B), (C) and (D) (c.f. Fig. 2.3. We attribute the absorption peak (A) (see text) to intraband polaron hopping which cannot be illustrated in the band structure scheme.

In order to identify the relevant transitions we have performed calculations of the electronic structure for PCMO with $x = 0$, 0.5 and 1 (Fig. 2.9). A detailed description of the electronic structure calculations will be presented in a forthcoming publication.

Here, we will mainly focus on the main features with respect to the absorption spectra, i.e., the band gaps, the Jahn-Teller (JT) splitting energies and the electronic band widths of the valence band.

For $x = 0$ and 0.5 the upper valence band edge (UVBE) is dominated by O $2p - e_g(\uparrow)$ hybrid states and the JT effect leads to a center-to-center splitting E_{JT} of the majority spin O $2p - e_g(\uparrow)$ hybrid band by $E_{JT} \approx 2.1$ eV ($x = 0$) and ≈ 1.7 eV ($x = 0.5$), respectively. The band gaps amount to $E_G(x = 0) \approx 1.6$ eV and $E_G(x = 0.5) = 0.6$ eV. For $CaMnO_3$ the band gap has charge transfer character with $E_G(x = 1) \approx 1.8$ eV. The main results from electronic structure calculations and a comparison with the related experimental values is summarized in Table 2.1 in Sec. 2.5.1.

According to the electronic structure calculations shown in Fig. 2.9 and the interpretation by Jung et al. we assign the peak (B) to on-site transitions between JT-split O $2p - e_g(\uparrow)$ hybrid bands and the peak (A) in the NIR range to the photon-assisted (intersite) hopping of small polarons. UV transitions (C) and (D) are identified as transitions between non-bonding O $2p$ states at about -1 eV in Fig. 2.9 and minority-spin $t_{2g}(\downarrow)$ and $e_g(\downarrow)$ states, respectively (details in Sec. 2.7). These transitions are marked by the blue arrows in Fig. 2.9.

2.5.1 Quasiclassical Small Polaron Model for PCMO

Intraband Polaron Hopping

The assignment of peak (A) to photon-assisted small polaron hopping and the applicability of quasiclassical small polaron theory can be examined by comparing the optically and the thermally induced hopping. The prefactor $\sigma(0, T)$ in Eq. 2.4 deduced from the absorption peak (A) and the measured *dc*-conductivities $\sigma_{el}(T) = 1/\rho(T)$ (Fig. 2.2a) at room temperature are presented in Fig. 2.10a. Both conductivities agree reasonably well and reveal the same doping dependence.

Moreover, the transfer integral J can be calculated from the activation barrier E_A and the polaron binding energy $E_P = 1/2\,\hbar\omega_{max}^{(A)}$ according to Eq. 2.3. [40,100] However, in doped manganites with their high charge carrier concentration the inter-site Coulomb repulsion $E_C \approx e^2/(12\varepsilon_0\varepsilon_r a_0)$ has to be taken into account. [55,110]

$$J = \frac{1}{2}E_P - E_A + E_C \tag{2.7}$$

The estimated transfer integrals J of the order of 90 meV are shown in Fig. 2.10b. From the electronic structure calculations we obtain band width of the O $2p - e_g$ valence band of $2D(x = 0) \sim 1.1$ eV and $2D(x = 0.5) \sim 0.9$ eV which corresponds to transfer integrals $J = D/Z \sim 92$ meV and 73 meV, respectively (see Table 2.1).

The consistency of the thermal and the optical conductivities as well as the agreement of experimental transfer integrals and electronic structure calculations apparently verify the applicability of the small polaron fit model and the assignment of peak (A) to polaron hopping.

In addition, the obtained vibrational energies $E_{vib}^{(A)}(T)$ basically reveal the expected temperature trends, i.e. an almost temperature independent behavior characterized by the zero-point phonon energy for $T < \Theta_D/2 \sim 150$ K and a linear increase with a slope of roughly kT at higher temperatures indicating thermal phonon broadening of the polaron absorption bands. The deviation from this temperature trend for $x = 0.2$, i.e. the decrease of $E_{vib}^{(A)}(T)$ at low temperature may be attributed to the presence of the ferromagnetic insulating (FMI) phase at $T < 180$ K. [30] Moreover, the vibrational energies governing small polaron hopping transfer at $T = 80$ K in hole doped PCMO ($x \leq 0.5$), $E_{vib}^{(A)} = 1/2\,\hbar\omega_0^{(A)} \sim 18 - 30$ meV, are roughly consistent with a band of vibrational Mn-O-Mn tilt modes found in the energy range of $\hbar\omega_0 \sim 30 - 50$ meV in PCMO at various doping levels. [20, 122, 123, 126] These modes change the octahedral tilting angle between nearest neighbor sites and, thus, may facilitate the inter-site hopping transfer.

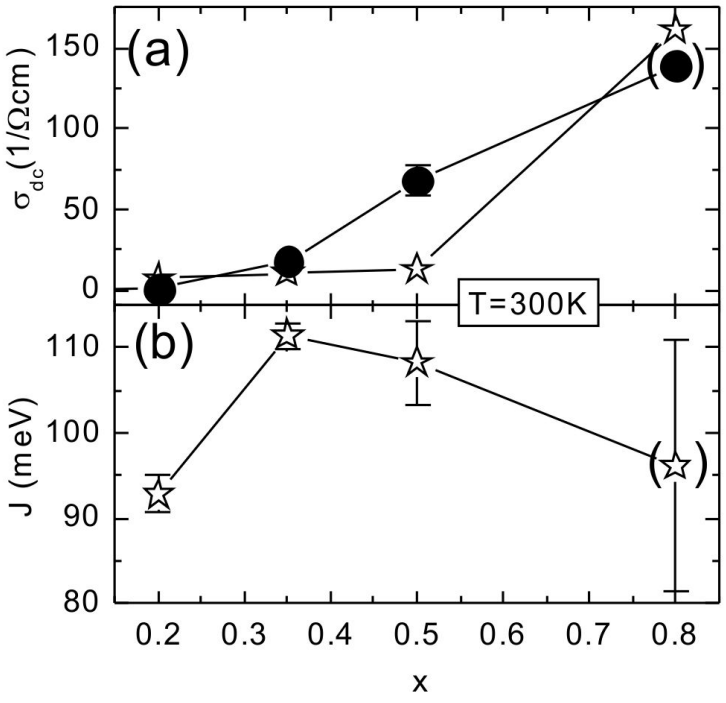

FIG. 2.10 Doping dependence of a) $\sigma(0,T)$ gained from fitting the optical conductivity (black spheres) and for comparison the *dc*-conductivity obtained via $\rho(T)$ measurement (open stars) and b) the transfer integral J determined via Eq. 2.7. Error bars are included if they exceed the symbol size. For $x = 0.8$ the reliability of J (parenthesized) is questionable.

The spectral weight of polaron hopping transitions is assumed to follow the doping

relation $\sim x(1-x)$. [22] This theoretical doping trend is illustrated as the black line in Fig. 2.7c. Polaron hopping depends on the number of occupied sites as well as unoccupied sites to which the polaron can hop. Thus, $SW^{(A)}$ should reveal a maximum at $x = 0.5$ where the probability to find an occupied site next to unoccupied site is highest. For $x = 0$ polaron hopping is absent (in accordance with our above made assumption that the peak (A) is absent) and the energetically lowest absorption band is associated with the inter-band JT transition (B). For $x \leq 0.5$ the spectral weight $SW^{(A)}$ follows the expected trend. We attribute the deviation for $x = 0.8$ to the failure of small polaron theory for fitting the electron doped system (see details below).

(a) Limitation of the small polaron theory for fitting peak (A) due to ordering effects.
The quasiclassical small polaron model (Eq. 2.4) is an effective single polaron model. However, the model disregards cooperative/ long range order effects. The variety of ordered phases like CO, OO, AFM and FM which govern the PCMO phase diagram [30,127] is not taken into account. Ordering effects have probably strong impact on the hopping energy. For instance, we attribute the decrease of $\hbar\omega_{max}^{(A)}(T)$ for $x = 0.2$ with decreasing temperature below 180 K to the presence of a FMI phase appearing at low temperatures in low doped PCMO samples. The ferromagnetic spin coupling in the FMI phase leads to a decrease of the activation energy and accordingly the polaron binding energy (Eq. 2.6). [128, 129]
The increase of $\hbar\omega_{max}^{(A)}(T)$ with decreasing temperature for $T > 180$ K is presumably due the emergence of CO/OO (Fig. 2.5). CO/OO ordering hinders the inter-site hopping transfer because of an additional energy barrier due to Coulomb repulsion. This barrier gives rise to a gap in the optical excitation spectrum in doping and temperature regimes with CO/OO ordering (Fig. 2.8b). For $x = 0.2$ the persistence of the OO phase in the entire temperature range of 80 K - 300 K leads to an optical gap of $E_{onset}^{(A)} \sim 400$ meV with marginal temperature dependence. [30, 127] In the case of $x \geq 0.35$ the CO/OO-disordered phase transition manifests in the opening of an optical gap at low temperatures.[1] Since the CO/OO-disordered phase transition is of first order accompanied by a phase separation, the change of the optical gap extends over a large temperature range. [97, 98] Despite the strong temperature induced spectral weight transfer in $x = 0.8$ no optical gap develops in this sample, although a transition to a CO phase is expected for $T < 200$ K. Note that the optical gap opening temperatures differ from the bulk charge ordering temperatures which amount to about 250 K for $x = 0.35$ and $x = 0.5$. [30, 127]
As a result of gap opening, the excitation energy $\hbar\omega_{max}^{(A)}$ for optical hopping processes increases with emerging CO/OO ordering. This effect is not considered in the small polaron theory. Hence, the determination of the polaron binding energy E_P from $\hbar\omega_{max}^{(A)}$ according to Eq. 2.6 yields enhanced values of E_P in doping and temperature regimes with CO/OO ordering compared to the effective polaron binding energy.

[1] Since negative values of the optical gap obtained via linear extrapolation of the low energy shoulder of the hopping transition are physically impossible, these values were set to zero.

(b) Limitation of the small polaron theory for fitting peak (A) due to non-adiabatic and finite bandwidth effects.
Furthermore, the applicability of the small polaron fit model is restricted to adiabatic hopping of polarons in the strong coupling regime when the peak width is determined by the phonon induced broadening, i.e. it requires $\gamma \leq 1,\ \lambda > 1,\ D << \Delta$ (see Sec. 2.3). We use the transfer integral deduced via Eq. 2.7 (Fig. 2.10b) for an estimate of γ and λ. The range of $0.4 \leq \gamma \leq 0.6$ derived for $x \leq 0.5$ suggests that the polaron ground state is formed within the adiabatic regime. However, we find $D \approx \Delta$. Thus, both limiting cases for the determination of E_P via Eq. 2.6 are not valid. The approximation $\hbar\omega_{max} = 2E_P$ underestimates E_P and thus the derived coupling parameters λ are too small. For instance, $\lambda = \frac{E_P}{6J} = 0.6$ for PCMO ($x = 0.35$) is usually attributed to weak coupling according to the $\gamma - \lambda$ phase diagram provided by Fratini et al. [110] Using the approximation $\hbar\omega_{max} = 2E_P - \frac{D^2}{2E_P}$ in Eq. 2.4 and $D \approx 430$ meV (Fig. 2.9), one yields $E_P \approx 470$ meV and $\lambda = \frac{E_P}{6J} \approx 1.1$ as an upper limit.
Furthermore, due to the underlying assumption $D << \Delta$, the contribution of the electronic band width $2D$ to the absorption peak width is disregarded in Eq. 2.4. Since $D \approx \Delta$, we overestimate the energies of the involved phonon modes and consider them only as order of magnitude estimates. With $\hbar\omega_0^{(A)} \sim 36 - 60$ meV our results are of about 20% larger than the energy of the Mn-O-Mn tilt modes found at 30 - 50 meV in PCMO. [20, 122, 123, 130]

Consequently, the adiabatic small polaron model Eq. 2.4 can be applied for yielding approximate values of the polaron binding energy and phonon modes and their relative changes as a function of temperature and doping. Polaron binding energies reported in literature are of the same order as our results, e.g. for $La_{0.7}Ca_{0.3}MnO_3$ Yeh et al. have found 0.35 eV. [131] The same polaron binding energy of 0.35 eV is reported by Loshkareva et al. for oxygen deficient $CaMnO_3$. [102]

For $x = 0.8$, the model Eq. 2.4 seemingly cannot be applied to the NIR absorption features, because the optical conductivity does not show typical small polaron behavior. In particular, the spectral weight of NIR transitions is shifted to very low photon energies at room temperature. This pronounced temperature dependence resembles somehow the small to large polaron crossover characteristics such as in $La_{1-x}Ca_xMnO_3$ and $La_{1-x}Sr_xMnO_3$. [59, 101] Since also the temperature trends of $E_{vib}^{(A)}(T)$ are not consistent with a phonon-assisted peak broadening which is proportional to kT for $T > \Theta_D/2$, we conclude that the application of quasiclassical theory of small polaron absorption is inappropriate for PCMO with $x = 0.8$.

Inter-Band On-Site Jahn-Teller Transitions

As mentioned before we use Eq. 2.4 also for fitting peak (B) identified as on-site JT transitions, even though they are inter-band transitions whose excitation energy is governed by band splitting. Our results for the excitation energy $\hbar\omega_{max}^{(B)}$ allow for an estimate of the JT energy E_0 which corresponds to the net energy gained by forming a

local JT-like lattice distortion, i.e. the balance of the electronic energy gain $-2E_0$ and the energy $+E_0$ expended for lattice deformation. [132]
Disregarding the impact of on-site Coulomb interaction U, the electronic band width $2D$ (strong coupling approximation for JT-polarons $D < E_0$) and ordering effects on the peak position of (B) we can get an estimate of the upper limit of E_0 from the excitation energy $\hbar\omega_{max}^{(B)}$. The absorption maximum at $\hbar\omega_{max}^{(B)}$ is determined by the total electronic energy difference between downshifted ($-2E_0$) and upshifted ($+2E_0$) JT split states and we can determine E_0 via $E_0 = \hbar\omega_{max}^{(B)}/4$.

In the case of undoped $PrMnO_3$ the JT excitation energy $\hbar\omega_{max}^{(B)}$ amounts to $\hbar\omega_{max}^{(B)}(x = 0) \sim 2.4$ eV (Fig. 2.7a). This corresponds to a net JT energy gain of $E_0(x = 0) \sim 0.6$ eV which is in good agreement with results obtained by other researchers for $LaMnO_3$ ($E_0 \sim 0.5$ eV). [106]
The shift of peak (B) to lower photon energies with increasing x (Fig. 2.7a) suggests that, hole doping leads to a decrease of the JT splitting energy. For the doped PCMO samples we obtain JT energies of $E_0 = 0.2 - 0.4$ eV which are comparable with literature results of doped manganites. [131] For PCMO $x = 0.4$ Thomas et al. report $E_0 \approx 0.1 - 0.3$ eV. [133]
The pronounced decrease of the excitation energy of peak (B) from $x = 0$ to $x = 0.2$ may be influenced by the cooperative ordering of JT distorted octahedra (OO phase) at room temperature. Note that in general, the JT energy tends to be slightly increased in CO/OO ordered phases (see Fig. 2.5).

With values of $E_{vib}^{(B)} = 1/2\ \hbar\omega_0^{(B)} \sim 50 - 60$ meV the vibrational energies gained from peak (B) for $0.2 \leq x \leq 0.5$ are about 50% higher than the phonon energies of symmetric JT stretching and breathing modes at $\hbar\omega_0 = 71 - 78$ meV. [20, 122, 123, 130] These modes affect the Mn-O bond length and, thus, on-site transitions between JT split states. We attribute the deviation to an overestimation of the vibrational energy by the small polaron fit model (Eq. 2.4 and 2.5) due to the disregard of the impact of the electronic bandwidth $2D$. Moreover, the values for the vibrational energies involved in the inter-band may suffer an enhanced impact of electronic bandwidth effects because the width of both, the occupied as well as the unoccupied JT band, affect the broadening of peak (B).

However, for $x = 0.8$ the application of the small polaron model (Eq. 2.4) yields characteristic phonon energies for peak (B) of the order of $\hbar\omega_0 = 2E_{vib}^{(B)} \sim 200$ meV (see Fig. 2.6d) which are significantly higher than the typical phonon energies of 30-80 meV observed in manganites. Obviously, Eq. 2.4 cannot be applied meaningfully to fit JT inter-band transitions in electron doped PCMO, because JT splitting is drastically reduced in this highly Ca-doped systems or even absent. Furthermore, the strong spectral weight increase of peak (B) with decreasing temperature (Fig. 2.4e) cannot be explained in the framework of JT transitions.

In order to compare the experimental fit results with related parameters obtained from

the electronic structure calculations, we summarize the JT excitation and onset energies, the electronic overlap integrals and the band gaps in Table 2.1.
The onset energies $E_{onset}^{(B)}$ for on-site JT transitions are correlated with the electronic band gaps. For $x = 0$ the experimental low temperature onset energy $E_{onset}^{(B)}(x = 0) \sim 1.55$ eV nicely corresponds to the theoretical band gap $E_G(x = 0) = 1.6$ eV (Fig. 2.9) whereas for $x = 0.5$ the experimental result $E_{onset}^{(B)}(x = 0.5)$ is smaller than the related theoretical band gap. However, doping trends of the band gap and the JT onset energy are consistent, i.e., both decrease with doping x (Fig. 2.8c) due to the decrease of JT the splitting energy E_{JT}.
The theoretical values of E_{JT} roughly correspond to the photon excitation energies $\hbar\omega_{max}^{(B)}$ consumed in on-site JT transitions (peak B). From electronic structure calculations, we obtain $E_{JT} \approx 2.1$ eV ($x = 0$) and ≈ 1.7 eV ($x = 0.5$) (between the band centers) which roughly matches the experimental values $\hbar\omega_{max}^{(B)}(x = 0) \sim 2.4$ eV and $\hbar\omega_{max}^{(B)}(x = 0.5) \sim 1.3$ eV (Fig. 2.7a).

x	J(theo)	J(exp)[T=300 K]	E_{JT}(theo)	$\hbar\omega_{max}^{(B)}$	$E_{onset}^{(B)}$	E_G
0	0.092	-	2.1	2.4	1.55	1.6
0.2	-	0.093	-	1.6	0.51	-
0.35	-	0.111	-	1.5	0.44	-
0.5	0.073	0.107	1.7	1.4	0.37	0.6
0.8	-	(0.096)	-	1.2	0.48	-
1	-	-	-	-	-	1.8

TAB. 2.1 Comparison of electronic and polaronic parameters: experimental (for $T = 80$ K) and DFT results for the transfer integrals J and the JT splitting energies $\hbar\omega_{max}^{(B)}$ and E_{JT}, the experimental onset energy of JT transitions $E_{onset}^{(B)}$ and the fundamental band gap E_G gained from band structure calculations. The energies are given in units of eV.

In the framework of mixed valent JT-distorted Mn^{3+} and undistorted Mn^{4+} sites, the spectral weight of on-site JT transitions $SW^{(B)}$ is assumed to decrease with hole doping x because the depletion of e_g electrons reduces the number of JT split states. Accordingly, we expect a doping dependence as $SW^{(B)} \sim (1-x)$ illustrated as the blue line in Fig. 2.7c. [22] As shown in Fig. 2.7c, the obtained $SW^{(B)}$ follows the expected trend for $x \geq 0.35$. However, for $x \leq 0.2$ our data deviate from the expected trend of $SW^{(B)} \sim (1 - x)$ and exhibit a converse behavior. This deviation suggests a doping induced change of the transition matrix element governing the spectral weight of peak (B) which we suppose to be due to doping dependent changes in the contribution of O $2p$ states to the UVBE as well as changes in the octahedral tilt (see Sec. 2.8).

2.5.2 Impact of O $2p$-Mn $3d$ Hybridization - Jahn-Teller and Zener Polarons

In the literature, two alternative pictures of the nature of small polarons in hole-doped PCMO are discussed: (i) the JT polaron describing the limiting case of a site-centered

carrier location involving mixed valence states, Mn^{3+} and Mn^{4+}. [59, 134] This limit would apply if the valence band is dominated by Mn e_g states. (ii) Zener-type polarons forming dimers of almost equivalent $Mn^{(3+x)+}$ sites, where the hole charge is located at the connecting O^- site. Such a dimer exhibits a flattened bonding angle. Zener polarons may be relevant when the UVBE is dominated by O $2p$ states. [60,61,63,64] The presence of static Zener-type polarons in the CO state of PCMO at $x = 0.5$ was confirmed by Wu et al. via structural analysis of electron diffraction patterns. [64] For $x = 0.3$ see Ref. [55].

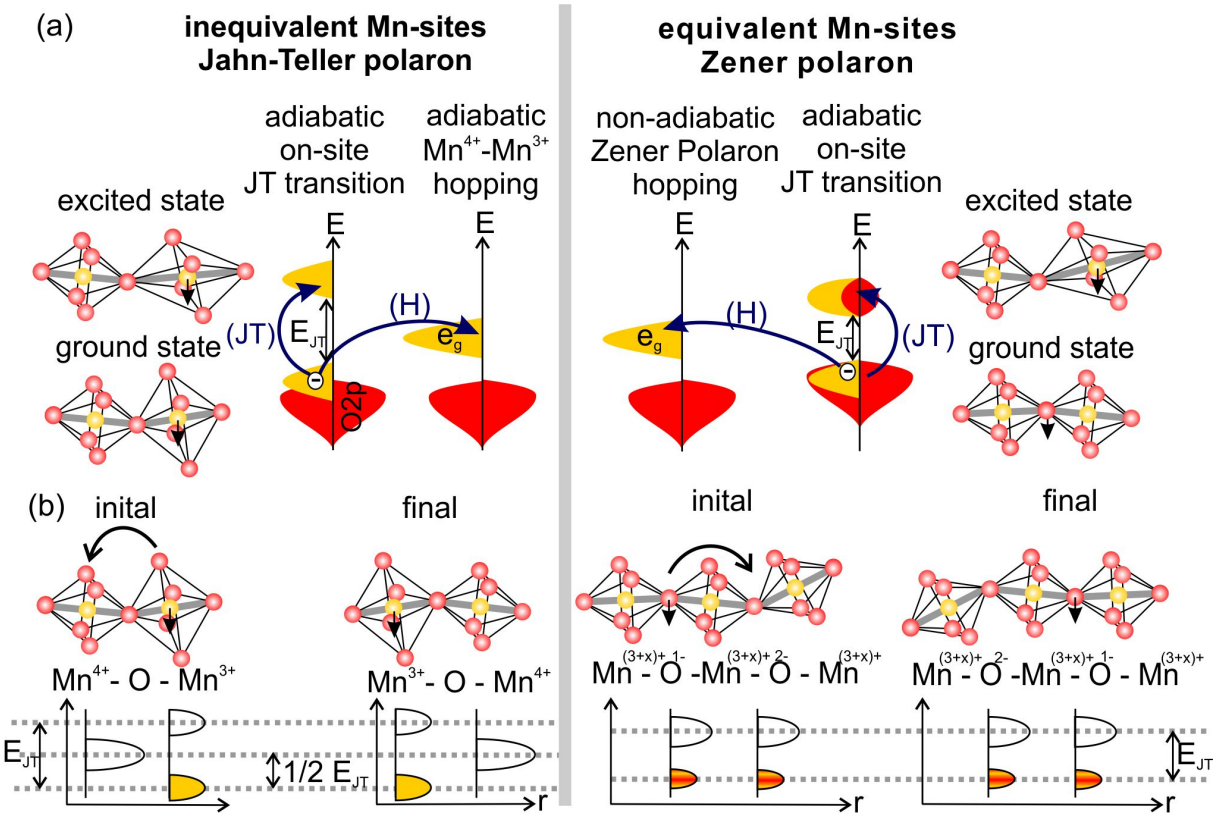

FIG. 2.11 Two alternative mechanisms leading to the double peak shape of σ_{NIR} and the relation $2E_P = 1/2\,\hbar\omega_{max}^{(B)}$ for hole doped PCMO in the limiting pictures of mixed Mn valence states (left) and equivalent Mn valence states (right): a) Electronic scheme of adiabatic JT on-site excitation representing a $d-d$ transition in the JT polaron picture (left). In the Zener polaron picture (right) the JT transition may have $p-d$ charge transfer character. Adiabatic hopping between Mn^{3+}/Mn^{4+} sites in the JT polaron picture and non-adiabatic hopping in the Zener polaron picture between equal $Mn^{(3+x)+}$ sites involving an Mn^{4+} transition state. b) Schematic lattice configuration and local electronic structure of the initial and final states for JT polaron hopping (left) and Zener polaron hopping (right). Notably, the JT energy in case of a Zener polaron (right) is reduced compared to the JT polaron (left).

Our results reveal that both, Zener and JT polaron dynamics is involved in hole doped PCMO. This is first of all suggested by the band structure in Fig. 2.9: The valence band in hole doped PCMO is JT split and simultaneously shows a strong contribution of O $2p$ states. Consequently, the polaron ground state formed after switching on the electron phonon-interaction carries an electronic structure which originates from JT split Mn

$3d - e_g$ states as well as from the O $2p$ orbitals. Second, the agreement of the vibrational energy $E_{vib}^{(A)}$ of the phonon mode coupling to hopping transfer (peak (A)) with octahedral tilt phonon modes for $x \leq 0.5$ gives evidence that Zener polaron dynamics is involved in the optically induced polaron hopping. [20, 122, 123, 130]

Indeed, the obtained values for JT transitions $2E_{vib}^{(B)}$ are larger than the stretching and breathing modes at $\hbar\omega_0 = 71 - 78$ meV. However, considering the limits of the small polaron theory (Eq. 2.4) for fitting inter-band JT transitions (discussed in Sec. 2.5.1) the vibrational energies associated with peak (B) are consistent with the assumption that JT dynamics is involved in the on-site excitation (peak (B)) in hole doped PCMO. A further indication for the relevance of JT as well as Zener polaron dynamics, is the observation that hole doping in PCMO affects both, the number of JT split states as well as the splitting energy (Fig. 2.7c and a). In the limiting case of mixed valence Mn^{3+}, Mn^{4+} (JT polaron), hole doping primarily reduces the number of JT split states, i.e. $SW^{(B)} \sim (1 - x)$ whereas the JT splitting energy $\hbar\omega_{max}^{(B)}(x)$ is expected to be constant over a large doping range. In the other limit of equal $Mn^{(3+x)+}$ valence states (Zener polaron), hole doping decreases the splitting energy but the amount of split states is independent of the doping level.

In the following, we discuss the observed correlation ($\hbar\omega_{max}^{(A)} \sim 1/2\ \hbar\omega_{max}^{(B)}$) between the polaron hopping (peak (A)) and on-site JT excitation (peak (B)) (see Fig. 2.7a) in both alternative frameworks of JT and Zener polaron like ground states. Figure 2.11 schematically shows the relevant initial and final states during on-site JT excitation and inter-site hopping transfer.

In the picture of mixed valence ground state with pure JT polarons (Fig. 2.11 left panel) the correlation of the respective transition energies $\hbar\omega_{max}^{(A)} \sim 1/2\ \hbar\omega_{max}^{(B)}$ (Fig. 2.7a) for hole doped PCMO is easily understood in the adiabatic limit. Here, an electron of a JT distorted Mn^{3+} site is excited into an undistorted next neighbor Mn^{4+} unit without JT splitting. Accordingly, the optical induced hopping evolves at $\hbar\omega \approx 2E_P = 1/2\ \hbar\omega_{max}^{(B)}$, i.e. the electronic contribution of the polaron binding energy corresponds to the gain in electronic energy due to JT distortion $\hbar\omega_{max}^{(B)}/2$. The on-site excitation evolves at $\hbar\omega \approx \hbar\omega_{max}^{(B)}$. In the non-adiabatic regime, hopping of site-centered JT polarons requires less energy, i.e. $\hbar\omega_{max}^{(A)} < 1/2\,\hbar\omega_{max}^{(B)}$ because the JT distortion follows the transferred electron more or less immediately. This is contrary to our observation that $\hbar\omega_{max}^{(A)} \geq 1/2\hbar\omega_{max}^{(B)}$.

In the picture of equivalent $Mn^{(3+x)+}$-$Mn^{(3+x)+}$ nearest neighbor sites with intermediate valence state, the hopping of hole states from one dimer to another involves initial and final states split by the JT effect (Fig. 2.11 right panel). $\hbar\omega_{max}^{(B)}$ depends on the Mn valence state and thus continuously decreases with increasing doping level as actually revealed by Fig. 2.7a. This observation strongly supports the intermediate valence scenario, depicted in the right panel of Fig. 2.11. Whether the transition state during hopping transfer involves a configuration, where the hole polaron is located at the

Mn-site and forms an Mn^{4+} intermediate, where the JT splitting is partially or totally lifted, depends on the competition between electronic and structural dynamics. In the Zener polaron picture an exact equality $\hbar\omega_{max}^{(A)} = 1/2\ \hbar\omega_{max}^{(B)}$ can be most easily understood in the non-adiabatic regime, where the transition state of the hole may involve a non JT split Mn^{4+} state (Fig. 2.11a right panel). In the adiabatic limit, the slow response of the lattice on photo-induced electron hopping leads to $\hbar\omega_{max}^{(A)} < 1/2\hbar\omega_{max}^{(B)}$.

However, the energies of the involved octahedral tilt ($\hbar\omega_0 \sim 30 - 50$ meV) and JT modes ($\hbar\omega_0 \sim 71 - 78$ meV) are in the same order of magnitude as the electronic overlap integral $J \sim 70 - 100$ meV (c.f. Table 2.1 in Sec. 2.5.1) and we expect that lattice deformation and electron transfer evolve at the same time scales. Consequently, neither the adiabatic nor the anti-adiabatic limit is fully valid. In perspective, time-resolved optical absorption experiments on the femtosecond scale may give clarification on what time scale the lattice responds the electronic excitation and to what extent adiabatic and non-adiabatic effects has to be considered.

Furthermore, the energies of the JT breathing/stretching mode and the Zener-type Mn-O-Mn tilt mode are in the same order of magnitude, i.e., both dynamics couple to electronic excitations on similar time scales. [135] Thus, they cannot be independent from each other and the potential landscape of the transition state determining the hopping excitation energy $\hbar\omega_{max}^{(A)}$ is assumed to be very complex. In optically excited states, the nature of the polaron, i.e., the coupling of the excited charge with phonon modes may even change.

In addition to changes in the speed of charge and lattice dynamics, temperature dependent deviations from the $\hbar\omega_{max}^{(A)} \sim 1/2\ \hbar\omega_{max}^{(B)}$ relation may be caused by polaron or magnetic order. For instance, CO/OO-ordering has an enhanced impact on optical inter-site hopping whereas on-site JT transition in small polaron systems are less affected by ordering effects. This leads to an increasing deviation from the observed room temperature relation $\hbar\omega_{max}^{(A)} \sim 1/2\,\hbar\omega_{max}^{(B)}$ with decreasing temperature. For $x = 0.2$, the deviation from $\hbar\omega_{max}^{(A)} \sim 1/2\ \hbar\omega_{max}^{(B)}$ can be assigned to the OO-phase which persists in the entire temperature range. [30, 127]

2.6 Summary and Conclusions

In the present article, we have applied quasiclassical small polaron theory describing the limiting case of the adiabatic strong coupling where the electronic level broadening is governed by phonons to fit doping and temperature dependent NIR absorption spectra of $Pr_{1-x}Ca_xMnO_3$ ($x = 0,\ 0.2,\ 0.35,\ 0.5,\ 0.8$) thin films. We retrieve the polaron binding energy E_P and the characteristic phonon energy $\hbar\omega_0$ coupling to the polaronic state. The double peak shape of the NIR absorption band observed for all doping levels $x > 0$ is interpreted as a result of optically induced inter-site polaron hopping and on-site transitions between Jahn-Teller (JT) split states. The obtained JT splitting energy

decreases with hole doping concentration as expected for an increasing Mn valence state according to $Mn^{(3+x)+}$ and thus supports the presence of an intermediate Mn valence state in doped PCMO. The presence of nearly equal $Mn^{(3+x)+}$ valence states in the ground state is further proven by electronic structure calculations of the electronic band structure which reveal a valence and conduction band formed by O $2p - e_g$ hybrid states which are split due to the JT effect for $x = 0,\ 0.5,\ 1$.

The application of quasiclassical small polaron theory to both types of phonon-assisted transitions gives a number of interesting qualitative insights into the interplay of JT and Zener polaron type of dynamics as well as rough quantitative estimates of key polaron parameters. The obtained polaron binding energies are of the order of $E_P \sim 300 - 450$ meV and tend to decrease with increasing doping x. The estimated vibrational energies coupling to the hopping transfer $\hbar\omega_0^{(A)} \sim 36 - 60$ meV and on-site JT transitions $\hbar\omega_0^{(B)} \sim 100 - 120$ meV are significantly larger than the characteristic Mn-O-Mn tilt and Mn-O stretching modes in PCMO, because the effect of a finite electronic bandwidth is disregarded in the applied analytical approximation.

Combining temperature dependent *dc*-resistivity measurement which provide the determination of the activation energy E_A with optical absorption spectra allows for an estimate of the electronic overlap integral J and the electronic band width $2D$. The obtained values $J \sim 100$ meV are roughly consistent with the theoretical calculations in Sec. 2.5. Absolute values for E_P, E_0, $\hbar\omega_0^{(A)}$ and $\hbar\omega_0^{(B)}$ need some corrections because $Pr_{1-x}Ca_xMnO_3$ does not perfectly fulfill the adiabatic strong coupling limit with phonon governed peak broadening. Finite band width and non-adiabatic effects in $Pr_{1-x}Ca_xMnO_3$ result in an underestimation of E_P and an overestimation of the characteristic phonon energies.

Ordering effects like charge, orbital or magnetic ordering, which are not considered in the quasiclassical small polaron model, has been found to affect the apparent polaron hopping energy. Charge and orbital ordering can generate an additional barrier for next neighbor polaron hopping and can lead to the opening of an optical gap whereas ferromagnetic ordering in $Pr_{1-x}Ca_xMnO_3$ ($x = 0.2$) at low temperatures facilitates hopping transport and may give rise to a decrease of the polaron binding energy E_P.
Our experimental and theoretical work advances the current research on the optical properties of polarons by giving a systematic study of the temperature and doping dependence of the polaron properties. Our results give evidence for the involvement of O $2p$ - Mn $3d - e_g$ states in the polaron absorption and prove the relevance of Zener as well as Jahn-Teller polaron dynamics in the NIR double peak absorption.

Acknowledgments The work was financially supported by the DFG via the SFB 602 project A20 and the SFB 1073 projects B02 and C02. We are grateful to H. Stein for preparation of the $PrMnO_3$ thin film and G. and L. Busse for experimental support with optical absorption spectroscopy.

2.7 APPENDIX I: Properties and Doping Trends of UV-Transitions

On the basis of the presented electronic structure calculations (Fig. 2.9) the peaks (C) and (D) in the UV range are identified as transitions from lower O $2p$ states ($\sim 1-2$ eV below the Fermi energy) into minority t_{2g} and e_g states of predominant $3d$ character. Transitions with t_{2g} final states (peak (C)) produce low spectral weight because t_{2g} orbitals are π-type and reveal a small orbital overlap with O $2p(\sigma,\pi)$ - orbitals. Thus, the transfer integral governing $\sigma,\pi \leftrightarrow \pi$ transitions is small. [69] Moreover, weak $\pi-\sigma$ type transitions into majority e_g states may be involved at the low energy tail of the UV-feature. In contrary, the spectral weight of peak (D) arising from transitions into σ-type minority e_g states which have large orbital overlap with O $2p(\sigma)$ orbitals is huge. The redshift of the UV absorption bands with increasing hole concentration observed in Fig. 2.3 reflects the trend in the theoretical results (Fig. 2.9) which is probably a consequence of the decrease of Hunds coupling energy E_H, on-site exchange interaction U and JT splitting E_{JT} accompanying the depletion of conduction electrons.
The temperature dependence of UV transitions is marginal in the measured temperature and doping range. Only peak (C) exhibits weak temperature dependence, i.e. its intensity increases with temperature which indicates that the optical transition O $2p \rightarrow t_{2g}$ underlying peak (C) is phonon-assisted.

2.8 APPENDIX II: Optical Matrix Elements for On-Site Jahn-Teller Transitions

We assume that the pronounced contribution of O $2p$ states to the UVBE and hybridization with e_g found in the electronic structure calculations may significantly affect the optical matrix element governing on-site JT transitions. Optical $d-d$ transitions in crystals with octahedral symmetry are generally dipole forbidden and should provoke weak intensity a factor 100-1000 smaller than intensities associated with spin and dipole allowed O $2p$-Mn $3d$ transfer transitions (UV-transitions, peak (C) and (D)). [69, 102] However, this is experimentally not observed in our and also other optical absorption studies which reveal rather high intensities for on-site JT transitions in manganites, i.e. even almost comparable with the intensity of UV absorption differing by at most one order of magnitude. [59, 69, 106, 111] The relevance of O $2p$ states at the UVBE in combination with a coupling to symmetry lowering vibrational Mn-O-Mn tilt modes, which is the fundament for the formation of Zener polarons, may enable dipole and spin allowed excitation channels and can lead to pronounced absorption intensities of JT transitions in agreement with experimental observations. Without coupling to phonon modes with u-symmetry, the on-site JT transition remains parity forbidden even if O $2p$ states with u-symmetry are contributing because the JT split occupied and unoccupied electronic bands have the same symmetry. A possible scenario explaining the high intensity of JT transitions may be a different coupling of the Mn-O-Mn tilt mode to an occupied compared to an unoccupied

JT split O 2p-Mn e_g state. This effect can also change the degree of O 2p contribution to both JT split states. In this case, the on-site JT excitation has $p-d$ charge-transfer contribution which is dipole allowed.
We further assume that the optical matrix elements change with the hole concentration due to a doping dependent lattice distortion [30] and O 2p - e_g reorganization at the UVBE which cannot be understood in the framework of rigid bands. [136] As a consequence the spectral weight of on-site JT transition as a function of doping may deviate from the simple relation $\sim (1-x)$ which is just based on the electron depletion of rigid bands with increasing doping level. This is consistent with our result for $SW^{(B)}(x)$ (Fig. 2.7c).

CHAPTER 3

In Situ Electrochemical Electron Microscopy Study of Oxygen Evolution Activity of Doped Manganite Perovskites

---

S. Raabe, D. Mierwaldt, J. Ciston, M. Uijttewaal, H. Stein, J. Hoffmann, Y. Zhu, P. Blöchl, and C. Jooss
Advanced Functional Materials **22**, 3378 - 3388, August 21, 2012
DOI: 10.1002/adfm.201103173

ABSTRACT Fundamental studies of catalysts based on manganese oxide compounds are of high interest since they offer the opportunity to study the role of variable valence state in the active state during O_2 evolution from H_2O. This paper presents a study of doping dependent O_2 evolution electrocatalysis of Pr-doped $CaMnO_3$ via in situ environmental transmission electron microscopy (ETEM) combined with ex situ cyclic voltammetry studies. ETEM studies of heterogeneous catalysis are a challenge, since the reactions in the H_2O vapor phase cannot directly be observed. It is shown that the oxidation of silane by free oxygen to solid SiO_{2-x} can be used to monitor catalytic oxygen evolution. Electron energy loss spectroscopy (EELS) as well as the in situ X-ray absorption study of near edge structures (XANES) in H_2O vapor reveals that the Mn valence is decreased in the active state. Careful TEM analysis of samples measured by ex situ cyclic voltammetry and an in situ bias-controlled ETEM study allows us to distinguish between self-formation during oxygen evolution and corrosion at the $Pr_{1-x}Ca_xMnO_3$ -H_2O interface. Including density functional theory (DFT) calculations, trends in O_2 evolution activity and defect chemistry in the active state can be correlated to doping induced changes of the electronic band structure in A-site doped manganites.

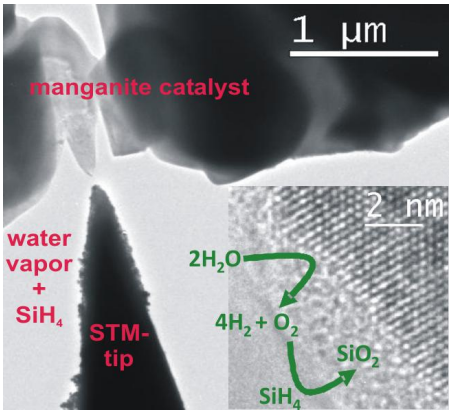

3.1 Introduction

Oxygen evolution catalysis still represents the bottleneck for electro- or photo-chemical water splitting. Here, the outstanding problem is control of the multi-electron transfer reaction in oxygen evolution from water, which requires the transfer of four holes for the liberation of one molecule of oxygen. The hole transfer to H_2O and the intermediates formed during the oxidation process requires a minimum energy of $\Delta E_0 = 1.23$ eV per carrier (superscript 0 indicates thermodynamic equilibrium value at standard conditions if no other conditions are explicitly stated otherwise).

The hole transfer can only be performed at low overpotentials if the catalyst can adjust the energy level of the donor states to the oxidation potential of H_2O and all subsequent transition states. [137] This requires a sufficiently complex atomic and electronic structure in the active state without suffering corrosive decomposition. The recent studies of structure and functionality of the $CaMn_4O_x$ - based oxygen evolution center in natural photosynthesis [15, 138–141] have provided insights into the pathway how nature solved the oxygen evolution challenge. The possibility that Mn-O compounds develop flexible mixed Mn valence states which strongly influence the Mn-O bonding strength and the charge transfer is believed to be crucial in the evolutionary selection of Mn sites for O_2 evolution. [12] Although there is agreement about this general picture, many details such as the detailed arrangement of mixed Mn valencies are not understood. [142]

Materials design of transition metal oxide catalysts relies heavily on the tailoring of electronic band structure and band occupation in the equilibrium state of the catalysts, in order to aim for optimum adjustments of the band edges to the oxidation potentials (see e.g.) [9, 143, 144].

Early mechanistic studies of perovskite oxides by Bockris and Otagawa suggested a correlation of catalytic activity with bonding strength between the B-site transition metal and oxygen due to occupation of anti-bonding d-states. [3] These trends have been recently reanalyzed by systematic DFT studies. [24,25,145] Based on the assumption that O_2 evolution from H_2O happens by a sequence of reaction intermediates $H_2O^* \rightarrow HO^* \rightarrow O^* \rightarrow HO_2^* \rightarrow O_2$ (g) (* indicates bonding of an O atom to the active B-site), the main conclusion is that the B-O bonding strength represents a universal descriptor for the catalytic activity of O_2 evolution. [146] This confirms the trends observed by Bockris and Otagawa that the activity increases from $LaCrO_3$ (d^3, strong O* binding) over $LaMnO_3$ (d^4), $LaFeO_3$ (d^5), $LaCoO_3$ (d^6) to $LaNiO_3$ (d^7, weak O* binding). A recent study by Suntivich et al. [2] demonstrates a volcano type relation between O_2 evolution activity and occupation of the anti-bonding Mn $3d - e_g$ states for different B-site cations. This correlation differs from the one emphasized earlier, namely that between activity and the complete d-occupation on the Mn-ion. Placing the focus specifically onto the occupation of the Mn e_g states can be rationalized via the larger hopping integral along the σ - anti-bond as compared to the π-bonding t_{2g} states. However, despite the significant progress in description of trends in the correlation between O_2 activity and electronic

structure of complex oxides, many effects remain elusive. In particular, the effects of A-site doping on the band structure as well as the real non-equilibrium electronic and atomic structure in the active state are not well understood.

Based on their rich electronic phase diagrams and inspired by the role of flexible Mn valence in the natural oxygen evolution center, doped manganites $AMnO_3$ are particularly interesting model systems for fundamental studies of active states in O_2 evolution. A-site doping via hetero-valent substitutions can tune the charge carrier concentration in the d-band between d^4 (Mn^{3+}) and d^3 (Mn^{4+}). For example, in $Pr_{1-x}Ca_xMnO_3$, $La_{1-x}Sr_xMnO_3$ and $La_{1-x}Ca_xMnO_3$, mixed Mn valence states can appear at intermediate doping [147] with a transition from overall p-doping at $x < 0.5$ to overall n-doping at $x > 0.5$. Due to electronic and electron-lattice correlation effects, doping can drastically alter the electronic band structure. Indeed, changes in A-site doping can induce transitions between phases with different band structure and magnetic properties sensitive to charge, orbital and polaron ordering. [52] At phase boundaries, such systems are very sensitive to external fields which can e.g. induce colossal resistance effects in electric fields. [60, 97] Furthermore, studies of the active state must take into account the defect distribution and its evolution during the operation of the catalyst: Defects such as oxygen vacancies change the surface atomic structure and doping. They can thus affect the Mn-O bond strength during activity but also may induce catalyst corrosion.

Here, we present an explorative electrochemical study combined with in situ environmental TEM (ETEM) investigations of $Pr_{1-x}Ca_xMnO_3$ ($x = 0.0 - 1.0$) as a manganite model system for oxygen evolution catalysis with tunable Mn valence state. Our results give insight into the effects of A-site substitution and oxygen vacancy formation on the active state and the origin of electrode corrosion. High resolution ETEM based on aberration image C_S-correction is a relatively new method. High resolution imaging (e.g. [80]) and observation of change of particle shape in gas has been demonstrated [81], but only a few studies were published on in situ ETEM observations of catalytic processes. [148–150] The influence of the electron beam on the catalyst is not well understood. Inelastic scattering of electrons in the catalyst can induce atomic displacements (knock-on damage) as well as electronic excitations (electron-hole pairs, secondary electron emission). A well known consequence of secondary electron emission in semiconductors is the formation of a positive electric potential. [151]

Combining different control experiments, in particular, application of an electric bias to the catalyst during in situ ETEM experiments and during in situ X-ray absorption near edge spectroscopy (XANES), we can develop insights into the effect of the electron beam on catalytic activity. Furthermore, we discuss the interplay between atomic and electronic changes in the active states and what controls the transition into corrosive decomposition of the catalyst.

3.2 Results

3.2.1 Voltammetry Study of Oxygen Evolution and Electrode Reduction

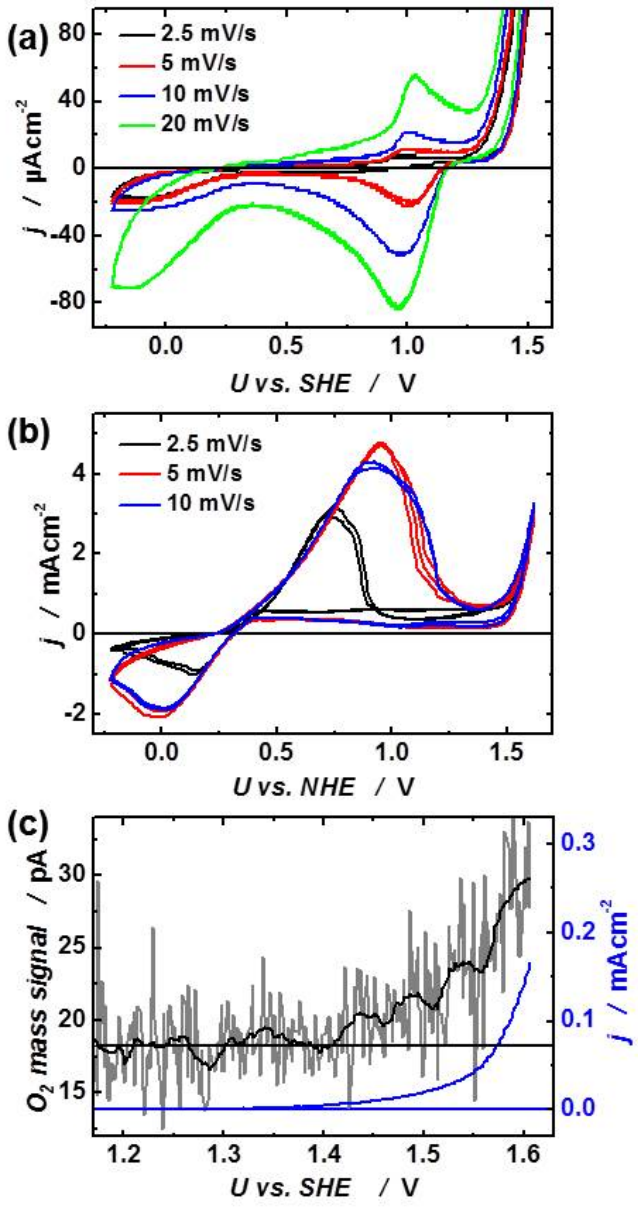

FIG. 3.1 Cyclic voltammetry (CV) of single-crystalline $Pr_{1-x}Ca_xMnO_3$ thin films. (a) Current density (j)-potential (U) curves for $x = 0.5$ and sweep rates from 2.5 mV/s to 20 mV/s. (b) CV for $x = 0.8$, cycles 8-9 at 10mV/s, cycles 11-12 at 2.5 mV/s, cycles 19-21 at 5 mV/s (c) Correlation between $j - U$ curve and O_2 mass signal at 2 mV/s for $x = 0.5$.

We have performed systematic cyclic voltammetry (CV) studies of oxygen evolution at $Pr_{1-x}Ca_xMnO_3$ (PCMO) thin film electrodes of different doping levels x. All CV studies are performed at 400 nm thick crystalline PCMO film electrodes on Pt/MgO with dominant [001] orientation. At all doping levels $0 \leq x \leq 0.8$, oxygen evolution is observed for a positive potential above E^0 ($H_2O \rightarrow 1/2\ O_2$) = 0.82 eV at pH = 7.

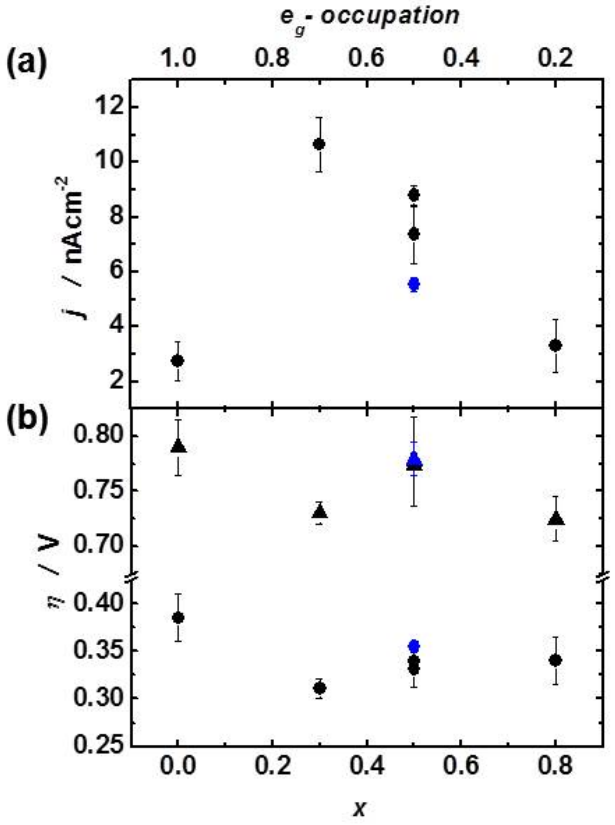

FIG. 3.2 (a) Exchange current density for oxygen evolution and (b) overpotential η for $j = 1\ \mu A/cm^2$ (circles) and $j = 930\ \mu A/cm^2$ (triangles) of PCMO thin film electrodes as a function of doping x. Black symbols represent data of the second $I-U$ - cycle while blue symbols show data of the seventh $I-U$ - cycle.

Figure 3.1 shows representative CV series measured at two different doping level $x = 0.5$ and $x = 0.8$, respectively. For $x = 0.5$, there is an additional reversible peak at $E^0 \approx 1$ eV (Figure 3.1a). The relatively small separation between the anodic and cathodic current peak, the strong sweep rate dependence as well as the weak dependence on the $I-U$-cycle number (see Figure 3.2) indicate a reversible surface oxidation/reduction. As also confirmed by TEM inspection, the electrode is entirely stable at $U = 1.43$ V vers. SHE over a period of 90 min (see supporting information Figure 3.9). In contrary, at $x = 0.8$, an irreversible process centered at about +0.35 eV is observed (Figure 3.1b). It is associated with high cathodic and even higher anodic current densities. Peak areas and separation

significantly increase with cycle number and thus clearly outweighing the sweep rate dependency. This indicates fast electrode corrosion related to diffusion controlled phase transition. The chemical analysis of corroded electrodes by energy-dispersive X-ray spectroscopy (EDX) reveals an A-site dissolution at the electrode surface which manifests in the formation of an amorphous MnO_x surface (see supporting information Figure 3.9d).

The exchange current density for oxygen evolution at thin film electrodes is of the order of a few nA/cm^2 and shows a doping dependence with a maximum of $j_0 \sim 11$ nA/cm^2 at $x = 0.32$ (Figure 3.2a). The overpotential η required for O_2 evolution approximately agree to the values observed by other authors. [2,3] For A-site doping, the overpotential η exhibits a significant decrease from $x = 0$ to $x = 0.32$ and no significant trend for higher doping (Figure 3.2b). The substitution x of Pr^{3+} by Ca^{2+} can be translated into a Mn $3d - e_g$ occupation which is presented in Figures 3.2a and b as well and will be discussed in Section 3.3. For further details of electrochemical analysis, see supporting information, i.e., Figures 3.8, 3.9 and 3.10.

3.2.2 In Situ Study of Activity via Environmental TEM

ETEM observation of catalytic activity of a material which catalyzes reactions in the gas phase is difficult, because small changes of the chemical composition of the gas must be monitored by mass spectroscopy. We found that the O_2 evolution can be monitored in the presence of small amounts of SiH_4 to the H_2O/He gas mixture. During oxygen production, SiH_4 is consumed and solid SiO_{2-x} grows on top of the active crystalline surface of the catalyst. As will be evidenced in detail in the following paragraphs, we find that electron beam induced SiO_{2-x} formation at crystalline PCMO edges in contact with SiH_4/H_2O vapor is due to electrocatalytic O_2 evolution, where the required positive potential develops due to secondary electron emission. Thus, the growth rate of the SiO_{2-x} layer is a direct measure of catalytic activity for O_2 evolution.

In high vacuum, PCMO ($0 \leq x \leq 1$) is fully stable against beam damage in electron fluxes of more than 10^6 $e/(Å^2 s)$. Figure 3.3a reveals a high-resolution TEM image of a crystalline PCMO ($x = 0.32$) sample edge before injection of H_2O vapor at [001] zone axis. PCMO has space group Pbnm over the entire doping range which corresponds to the charge disordered phase and has been confirmed by electron diffraction. In some thin areas near the edge to the vacuum, the sample reveals a 2 x 2 superstructure, which provides evidence for an oxygen deficiency and a related oxygen vacancy ordering.

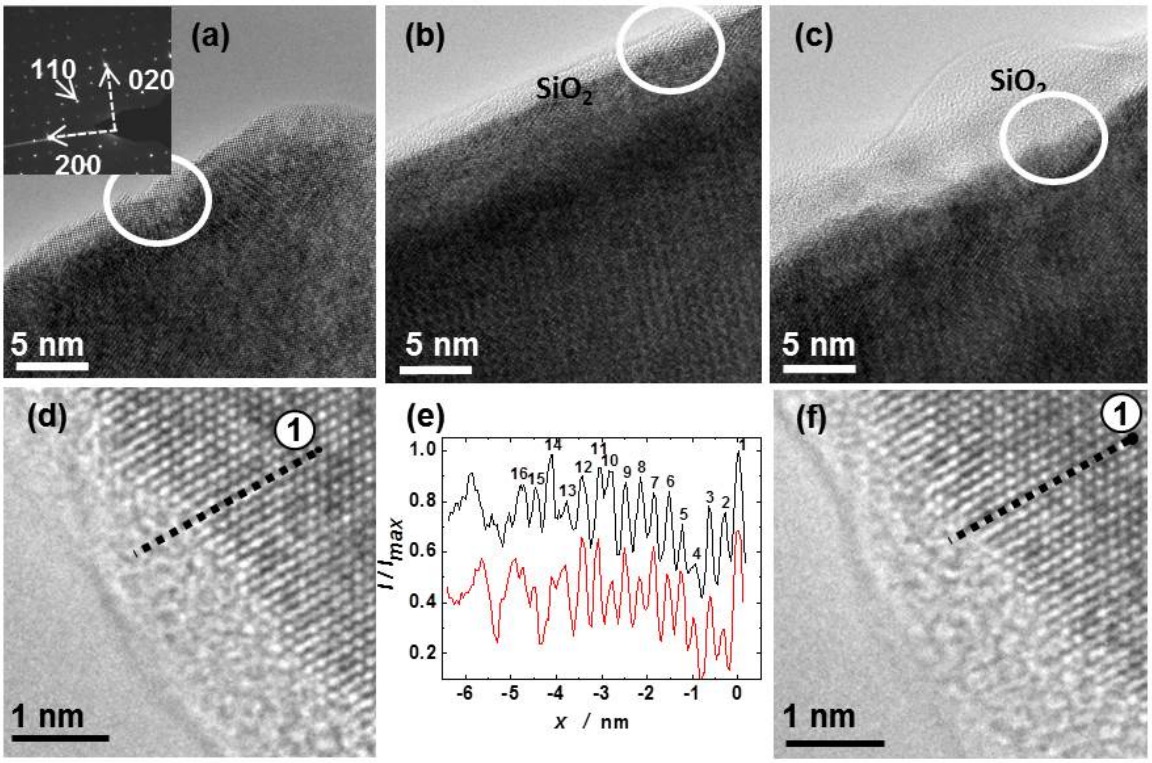

FIG. 3.3 ETEM study of crystalline PCMO $x = 0.32$ during electron and water exposure. (a) High-resolution bright field TEM image acquired in high vacuum showing the pristine state of a grain at [001] zone axis with the crystalline area fully extended to the edge. The inset shows a electron diffraction pattern of the same area near [001] zone axis showing Pbnm Bragg reflections with a 2 x 2 superstructure. The same section as in (a) is shown during an ETEM experiment in water vapor, where the growth of an amorphous SiO_{2-x} layer indicates oxygen evolution activity of the edge (b) 20 s and (c) 70 s after start of the electron beam stimulation. The gray circle is a marker for a specific edge location. (d-f) Interplay between catalysis and corrosion at another area of the same sample. (d) and (f) High-resolution TEM images of a grain at [201] zone axis after 300 s and 310 s of electron beam exposure in water vapor and resulting SiO_{2-x} coverage. (e) Intensity modulation along the same line depicted in (d) and (f). The first atomic column of this line is labeled as "'1"'. The distance between atomic columns along the lines corresponds roughly to half of the b lattice constant (0.285 nm). The change from a periodical to a more or less statistical oscillation indicates the crossover from well-crystalline PCMO to corroded amorphous PCMO followed by SiO_{2-x}, respectively.

After injecting the H_2O/He mixture with H_2O partial pressure of $\sim$ 0.013 mbar into the sample chamber, the sample is equilibrated for 30 min in the gas without electron exposure to account for thermal drift induced by convective cooling. Electron beam illumination of a crystalline PCMO sample area with 10^4 $e/(Å^2 s)$ induces immediate growth of an amorphous SiO_{2-x} layer at crystalline edges (Figure 3.3b,c, see movie M1 in the supporting material). Simultaneously, the 2 x 2 superstructure gets more pronounced and is extended over a much wider area. The thickness of the SiO_{2-x} layer rapidly increases within minutes to several nanometers (Figure 3 b-c). Above a thickness of $\sim$ 10 nm, the growth rate drastically slows down. A subsequent analysis of this layer

by electron energy loss spectroscopy (EELS) as well as by EDX clearly indicates that the layer consists of SiO_{2-x} formed by oxidation of gaseous SiH_4. The SiO_{2-x} growth is observed all over the electron irradiated crystalline PCMO regions including the top and bottom surfaces. However, the spatial distribution within the irradiated region is inhomogeneous most likely due to surface topology and its impact on the SiO_{2-x} nucleation.

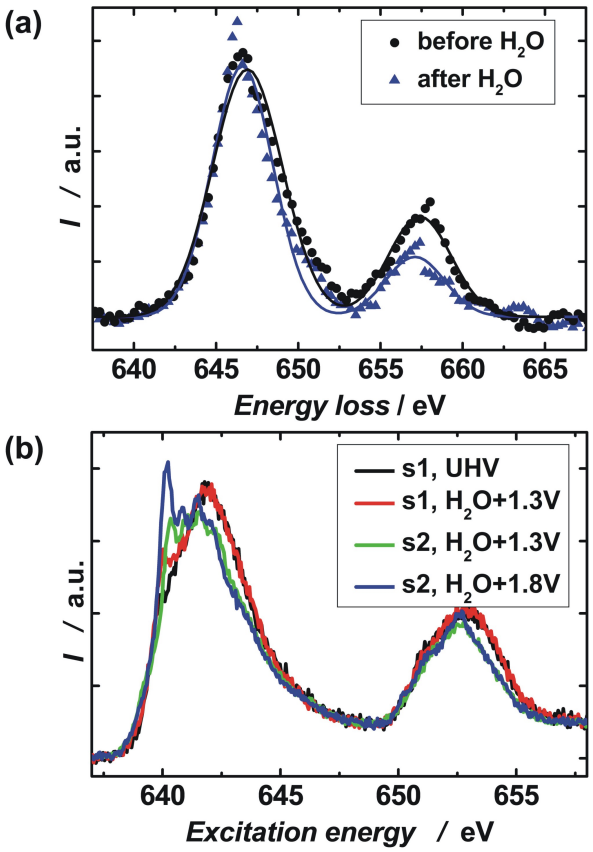

FIG. 3.4 Change of the Mn L-edges in the active state of PCMO $x = 0.32$ revealed by in situ ETEM (a) and in situ XANES (b) experiments.(a) Core loss EELS spectra after Hartree-Slater background subtraction before and after electrocatalytic O_2 evolution. Both spectra are acquired in high vacuum mode before switching to and after switching back from ETEM operation mode and stimulating the sample in 0.013 mbar H_2O vapor with 10^4 $e/(Å^2s)$. The L_3/L_2 ratio increases from 2.5 to 4.8. (b) In situ XANES study of two PCMO films s1 and s2 with $x = 0.32$ in UHV and in contact with H_2O vapor at different positive bias. The increase of intensity at the L_3 edges at about 640.3 eV indicates an increasing fraction of Mn^{2+}. [152]

The SiO_{2-x} formation can entirely be suppressed by reducing the electron exposure below 10^3 $e/(Å^2s)$ and was neither observed by illumination of the Cu grid nor at amorphous PCMO edges for any intensity of illumination. A control experiment at an amorphous

edge of the same grain as shown in Figure 3.3 is presented in the supporting information (Figure 3.11). Therefore, oxidation of SiH_4 takes place only on top of regions with crystalline PCMO, while regions with amorphous PCMO remain inert. This rules out that SiH_4 is directly oxidized by a direct reaction with H_2O vapor and suggests that SiO_{2-x} growth can be used as an indicator for local O_2 evolution activity of the catalyst material (see also supporting information Figure 3.15).

In its active state during O_2 evolution, PCMO undergoes structural and electronic changes which have been studied via EELS in the ETEM and via in situ XANES in water vapor (see Figure 3.4). Changes in electronic structure are visible in the Mn core loss spectra which are acquired by EELS at distances between 3 nm and 30 nm from the interface to SiO_{2-x} . The peak ratio of the Mn-L_3 and Mn-L_2 lines is used to calculate the Mn valence (see supporting information for details). In the ETEM experiment (Figure 3.4a), the L_3/L_2 peak ratio increases from the virgin state in high vacuum to the state measured directly after performing active O_2 evolution in H_2O vapor and switching back to high vacuum mode. The increase of the L_3/L_2 peak ratio is measured all over the electron-beam exposed area and indicates a reduction of the Mn mean valence from $+3.2 \pm 0.7$ (virgin state) to values around $+2.0 \pm 0.9$ (post mortem analysis of active state). The measured Mn valence in the virgin state corresponds to the valence of + 3.3 which is expected from the hole doping at $x = 0.32$.

A mean valence close to 2+ without changes in the cation composition corresponds to the formation of Mn^{2+} in electron-doped $Pr_{0.68}Ca_{0.32}MnO_{3-\delta}$ with $\delta \approx 0.5$ during catalytic activity. The transition to the Brownmillerite phase via progressive oxygen vacancy creation and ordering in the major part of the stimulated area is also supported by increase of area with 2 x 2 superstructure. In order to rule out that oxygen vacancy formation is mainly due to the effect of high energy electrons in the ETEM, XANES measurements of the change of the Mn L_3/L_2 edges of PCMO films ($x = 0.32$) in contact with H_2O vapor were performed. In addition, the change of the Mn L-edge in contact with H_2O vapor and under application of a positive bias is monitored (Figure 3.4b). The shift from 641.9 eV to a lower excitation energy of 640.3 eV confirms the decrease of Mn valence state through an increase of the fraction of the Mn^{2+} species. Although the excitation conditions are very different, the same trend in Mn valence change is observed via both in situ methods, where the electrodes are in contact with H_2O vapor. It is most likely that the observed Mn valence decrease is an intrinsic feature of the active state of PCMO at $x = 0.32$. The formed phase which is similar to oxygen deficient Brownmillerite is quite stable in the active state and can be well separated from corrosion process.

3.2.3 In Situ Study of Catalyst Corrosion Via Environmental TEM

The combination of electron beam exposure at 10^4 $e/(Å^2 s)$ and water environment causes corrosive degradation of PCMO at the interface to SiO_{2-x} which is rather slow for $x = 0.32$ and fast for $x \geq 0.75$. Dynamic observations are shown in the supporting information (movies M2 for $x = 0.32$ and M3 for $x = 0.95$). Analyzing the time

evolution of a row of atomic columns (Figure 3.4d-f), the periodic oscillations which indicates well-crystalline PCMO ($x = 0.32$) are reduced by two atomic columns in 10 s via amorphization. Notably, the growth of the SiO_{2-x} layer is $\sim$ 10 nm/min, much higher than the interface recession of $\sim$ 1.8 nm/min. The ratio of the rates of SiO_{2-x} formation to PCMO degradation indicates catalytic turnover numbers of about 10 under the specified ETEM conditions. Thus, reduction of the PCMO ($x = 0.32$) is not a main source of oxygen for SiO_{2-x} formation.

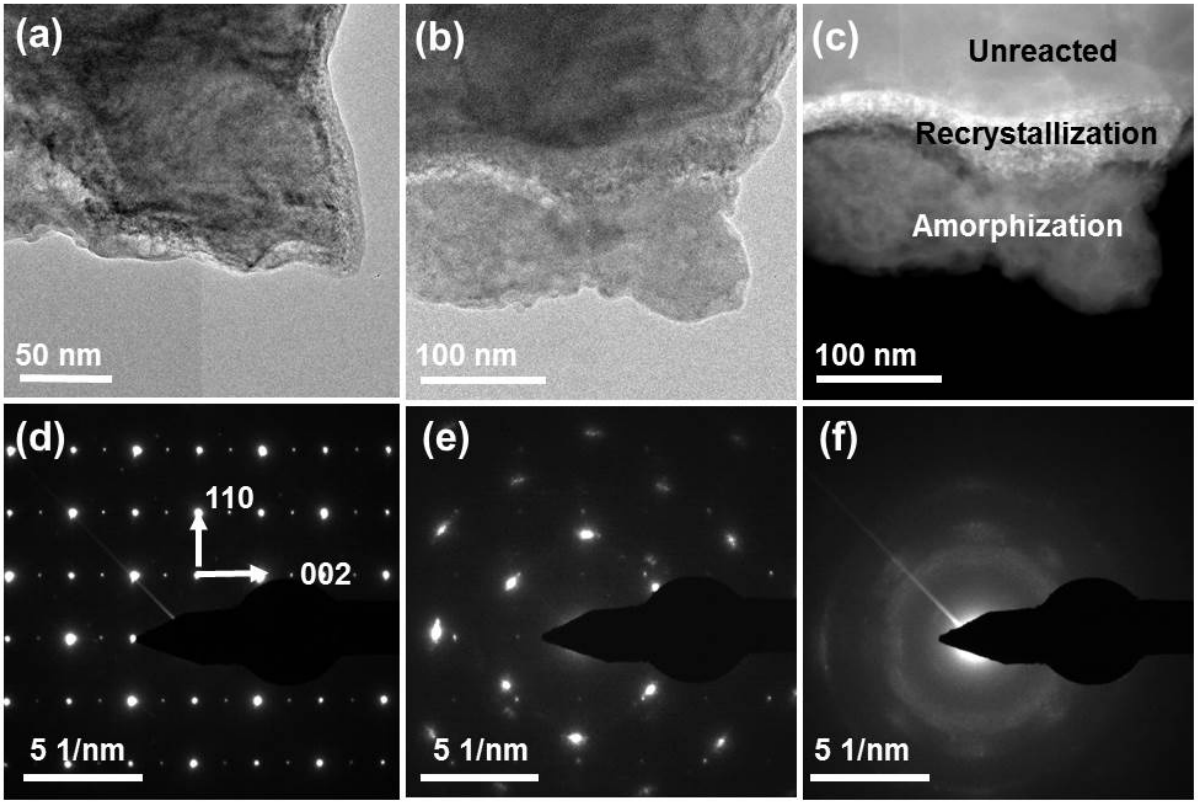

FIG. 3.5 Corrosive behavior of PCMO $x = 0.95$ bulk exposed to H_2O vapor during stimulation with 300 kV electrons. (a) Bright field TEM image before gas injection shows a crystalline sample edge in the [-110] zone axis. The corresponding diffraction image (d) reveals Pbnm structure. Bright field TEM image (b) and annular dark field STEM image (35-70 mrad collection angle) (c) of the same area after exposure with 2 min electron flux of 10^4 $e/(Å^2s)$ in 0.013 mbar H_2O. A pronounced corrosion due to recrystallization and subsequent amorphization is observed. Unreacted and amorphous regions are separated by recrystallized domains. Only one small nucleus of SiO_{2-x} is observed (white circle). (e) The diffraction pattern of the recrystallized domains reveals a crystal symmetry inconsistent with the initial Pbnm symmetry and is most likely Mn rich cubic phase. The observation that the recrystallized region exhibits a unique crystal orientation and symmetry with broadened peaks combined with the strong inhomogeneity of contrast in the STEM images indicates an initiating chemical decomposition. (f) The diffraction pattern of the amorphous regions.

In strong contrast, non-doped $PrMnO_3$ and PCMO electrodes with high Ca concentration ($x = 0.8$, 0.95 and 1) undergo drastic corrosion processes in ETEM experiments at the same H_2O partial pressure and electron flux. As a typical example, Figure 3.5 shows

the results for $x = 0.95$. Crystalline edges remain completely stable under electron irradiation of more than 10^6 $e/(Å^2s)$ in high vacuum (Figure 3.5a). Exposure to water with partial pressure of ~ 0.013 mbar under an electron flux of 10^4 $e/(Å^2s)$ causes first re-crystallization toward an intermediate phase with a crystal symmetry incompatible with perovskite structure and subsequently a transition to a nearly amorphous phase with some nanocrystalline grains (Figure 3.5b,c). The diffraction spots originating from the recrystallized phase are significantly broadened compared to the sharp reflections of the initial crystal phase (Figure 3.5d,e). This broadening may be interpreted in terms of an initiating chemical decomposition.

This is confirmed by the contrast variations within the recrystallized domain in the annular dark field STEM image in Figure 3.5c. It is acquired at a scattering angle of 35-70 mrad and is thus a mixture of diffraction contrast and Z-contrast. Local EELS analysis of corroded recrystallized as well as amorphous regions shows presence of Pr, Ca, Mn and O, but the Ca/Mn ratio is decreased by 30-40% after water exposure. This indicates a substantial A-site depletion and decomposition of Ca-rich compounds in water vapor. In the early stages of the electron- beam driven reaction, small nuclei of SiO_{2-x} start to grow but quickly disappear during the progression of the corrosion process. With a rate of $\sim$ 80 nm/min, the corrosion front in the $x = 0.95$ samples moves 80 times faster than for $x = 0.32$ and no catalytic turnover is obtained.

3.2.4 Bias Control of Processes via an Electrochemical Cell

Our hypothesis that an electron beam induced positive electric potential due to secondary electron emission drives the electrocatalytic activity of PCMO as well as the corrosive degradation can be directly proven by application of an electric bias to the PCMO electrode. In order to perform this electrochemical ETEM experiment under well controlled conditions, we have used a TEM sample holder with a piezo-controlled nanotip, where an electric potential can be applied to the TEM sample (Figure 3.6). The so formed electrochemical cell is composed of a PCMO working electrode ($x = 0.95$), a Pt/Ir tip as counter electrode and the $He/H_2O/SiH_4$ gas mixture as an analogue to an electrolyte. In order to minimize the resistance between both electrodes, the tip is carefully set into contact with the working electrode (Figure 3.6a,b). At a negative voltage of about - 1 V, neither SiO_{2-x} formation nor corrosive recrystallization/amorphization processes are observed (Figure 3.6c,d) although the same electron flux was applied for stimulation as in Figure 3.5. As confirmed by electron diffraction (Figure 3.6d), the Pbnm crystal structure remains entirely intact. The observed change in the shape of the electrode during the ETEM experiment at - 1 V is due to mechanical contact forces between the tip and the sample.

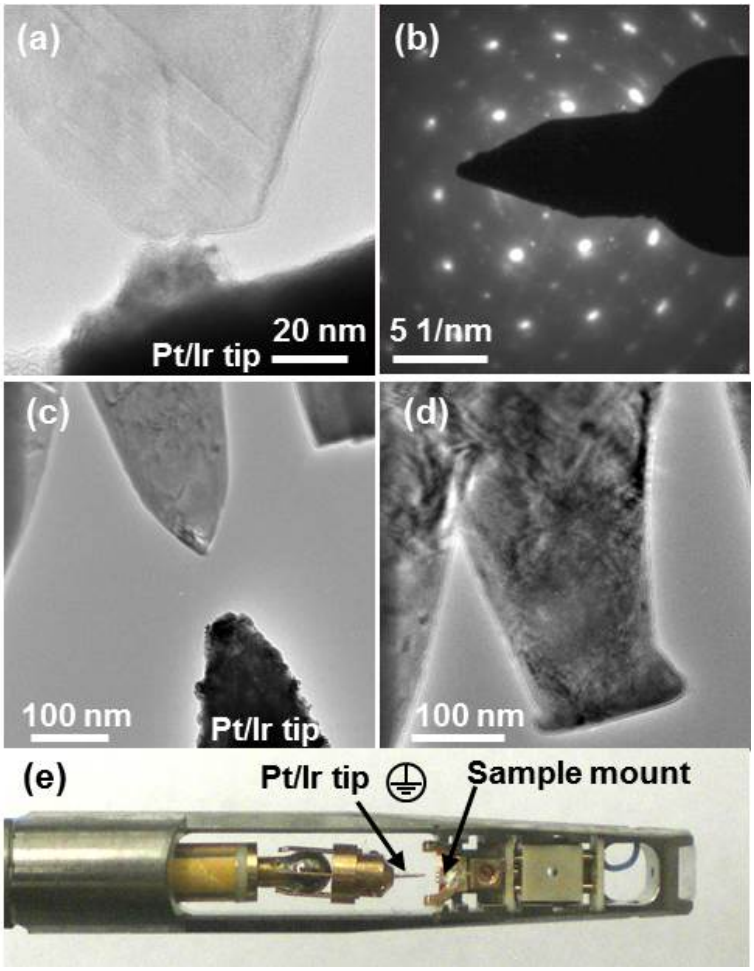

FIG. 3.6 Two electrode electrochemical cell in the ETEM with PCMO $x = 0.95$ working electrode and Pt/Ir as a counter electrode. (a) Bright field overview TEM image shows the two electrode configuration with a well-crystalline PCMO ($x = 0.95$) grain at [001] zone axis in the virgin state just before and (b) during contact with the Pt/Ir tip. (c) Bright field image of the same grain after H_2O and electron expose with applied bias of -1V. The absence of SiO_{2-x} growth indicates that oxygen evolution is suppressed at negative bias. (d) Diffraction pattern after reaction in gas. Neither recrystallization nor amorphization is observed and the perovskite structure of the electrode remains entirely intact. (e) Sample holder with piezo-controlled nanotip which is used to set up the electrochemical cell (see section 3.5).

3.3 Discussion

3.3.1 Band Structure Trends in O_2 Evolution Activity

Understanding catalytic O_2 evolution requires detailed understanding of the strengths of Mn-O and O-O bonding at the surface as well as of the charge transfer processes of hole carriers between the electrode surface and the adatoms. The full theoretical description of such processes including surface states in the active state of the catalyst is far beyond the scope of this work. We focus here on the effect of A-site doping on the bulk band structure of PCMO in order to discuss the observed doping trends. The main

features are schematically shown in Figure 3.7 taken into account experimental data as well as DFT calculations (for details see supporting information, Figures 3.12 and 3.13).

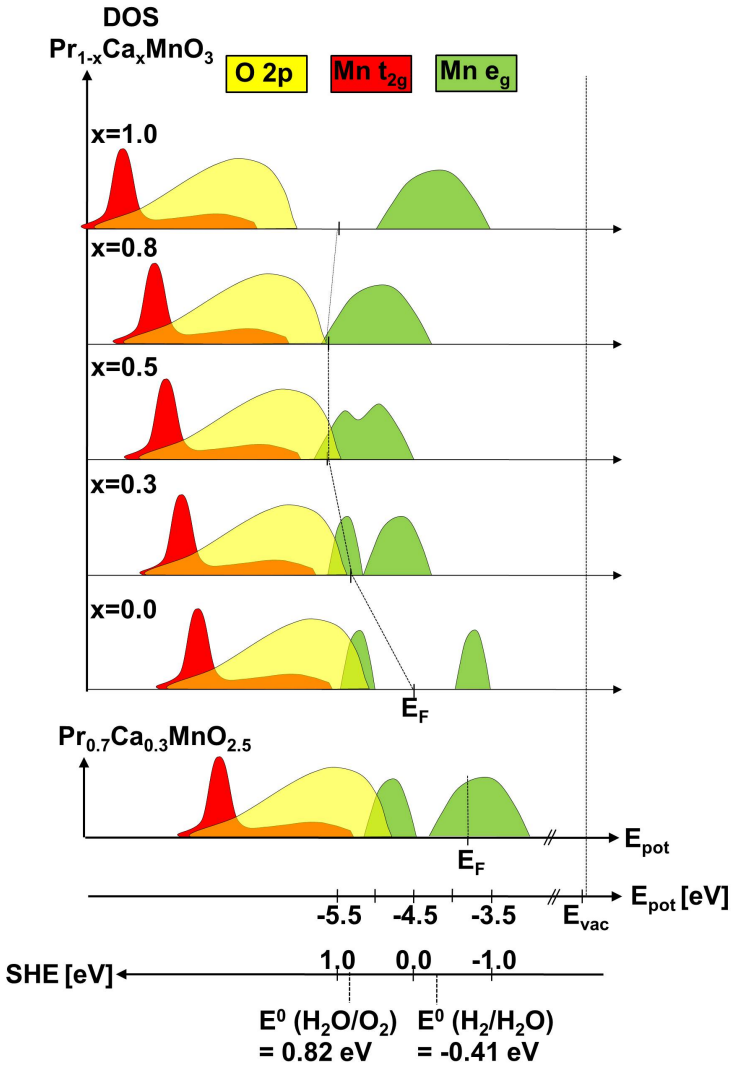

FIG. 3.7 Schematic evolution of the band structure of $Pr_{1-x}Ca_xMnO_3$ based on DFT calculations and literature results (see supporting information Fig. 3.12 and Fig. 3.13). The schematic representation mainly focuses on change in the work function (Fermi level), the splitting and shifts of the Mn $3d - e_g$ majority states due to the Jahn-Teller effect, the shift in the O $2p$ states and the resulting overlap of Mn $3d$ and O $2p$ states. The energy scale is shown with respect to the vacuum level and to the electrochemical SHE. Potentials E^0 for oxygen and hydrogen evolution at pH = 7 are also indicated.

$CaMnO_3$ is a charge-transfer insulator, i.e. the valence band top is made from O $2p$ states, while the conduction band is dominated by Mn $3d - e_g$ states. [106, 107, 153] In contrast, $PrMnO_3$ resembles a Mott insulator, where however, the band gap is between the lower and upper Mn $3d - e_g(\uparrow)_1$ and Mn $3d - e_g(\uparrow)_2$ bands which are split by a static cooperative Jahn-Teller effect. Therefore, the upper valence band edge and the lower

edge of the conduction band are both dominated by anti-bonding Mn $3d - e_g(\uparrow)$ states.

If a rigid band approximation applies for different doping levels the substitution of Pr^{3+} by Ca^{2+} leads to hole doping of the lower e_g-band in $Pr_{1-x}Ca_xMnO_3$ visible in a shift of the work function φ. However, the available data for φ in PCMO in the doping range $0 \leq x \leq 1$ (see supporting information 3.13) show a small drop between $x = 0$ and $x = 0.3$ which reflects the disappearance of the band gap for $0.3 \leq x \leq 0.7$ at room temperature. [21] In this doping range, a low-temperature charge/polaron ordered phase is present, where the lower e_g band is further divided. In the charge ordered state, the opening of a gap of 0.25 ($x = 0.3$) to 0.15 ($x = 0.5$) eV is observed. [136] The nearly constant φ value up to $x = 1$ indicates a reorganization of the top valence band edge with an increasing weight of O $2p$ states which ends in the establishment of an charge transfer insulator at $x = 1$.

Our study of the trends in catalytic O_2 evolution activity as a function of A-site doping show interesting correlations to specific changes in the electronic band structure. We observe an increase of the exchange current density and decrease of the overpotential for increasing e_g occupation (Figure 3.2) with the exception of $x = 0$ which requires much larger overpotentials. It is shown for several perovskite oxides in the study of Suntivich et al. [2] that Mn $3d - e_g$ occupation is a good descriptor for the Mn-O bonding strength which determines the left side of the volcano. [24] Except for $x = 0$, the trend in our data agrees with this statement (see supporting information 3.14). In this doping range ($0.3 \leq x \leq 0.8$), a "metal-like" Mn $3d - e_g$ - O $2p$ conduction band is formed at the Fermi level and its occupation can be continuously changed with x. In contrast, for undoped $PrMnO_3$ with the highest nominal e_g filling, the e_g band is split due to a cooperative Jahn-Teller effect and orbital ordering (Figure 3.7). The splitting significantly reduces the energy of the occupied Mn $3d - e_g(\uparrow)_1$ states. Such strong changes in the band structure indicate that a picture, where the strength of the Mn-O bond simply depends on the occupation of an otherwise rigid e_g band has serious limitations when correlation effects become important.

Most favorable electrocatalytic properties are observed for p-doped PCMO in a doping range $0.3 \leq x \leq 0.5$, where hole carriers are polarons with relatively high mobility and have mixed Mn $3d - e_g$ and O $2p$ character. From the highest j_0 in that doping range, we conclude that such mobile hole states in more or less covalent Mn-O bonds can establish the most efficient charge transfer across the PCMO-H_2O interface.

3.3.2 Electron Beam Driven O_2 Evolution Catalysis in the ETEM

The two major excitation effects of 300 keV electron beam are related to inelastic scattering at atomic nuclei and electrons. The former can generate element specific atomic displacements (knock-on damage) above a critical acceleration voltage and above a critical electron flux (see e.g. [154]). The latter can generate electronic excitations

such as electron-hole generation and secondary electron emission. Emission of secondary electrons can leave holes behind them. Depending on the mobility of charge carriers in the material secondary electron emission thus can generate a positively charged area at samples with potential up to several 10 V. [151] For PCMO under an electron flux of 10^4 $e/(\text{Å}^2\text{s})$, we estimate a potential of the order of $\sim$ 1 V, a value which is also evidenced by the observation that electrochemical activity can be fully suppressed by a negative bias of 1 V. A quantitative modeling of the induced positive space charge layer is beyond the scope of this paper and will be published elsewhere. [155] Depending on the exact value of the oxidation potential E($H_2O \rightarrow O_2$) under ETEM conditions, the beam induced positive potential is thus able to shift hole states to a positive overpotential and thus drive the electro-catalytic O_2 evolution.

Electron beam driven SiO_{2-x} growth represents a direct solid state indicator for electrocatalytic activity of crystalline PCMO edges. Under ETEM conditions, the SiH_4 oxidation is correlated to electrocatalytic oxygen evolution at PCMO electrodes using the $H_2O/He/SiH_4$ gas mixture as an electrolyte. Direct SiH_4 oxidation either via deoxygenation of PCMO or via reaction of H_2O can be directly excluded since SiO_{2-x} growth does not happen under electron beam stimulation if PCMO corrosion becomes significant or at an inactive PCMO edge (e.g. amorphous areas due to TEM sample preparation). The electrocatalytic O_2 evolution is also visible by the increase of the O, O_2 and H_2 mass signals when the electron beam is shifted from vacuum to a catalytic active sample edge (see supporting information 3.15).

3.3.3 The Active State of the Catalyst

Oxygen vacancies at oxide catalyst surfaces often play an important role for catalytic activity (see e.g. [24]), since they influence coordination, bonding strength, doping and electronic states at the surface. Our observation of Mn valence decrease during oxygen evolution activity (ETEM) and under similar conditions in in situ XANES gives direct evidence that oxygen vacancies (V_O") are formed during oxygen evolution activity. The observation of Mn^{2+} in ETEM correlates with pronounced 2 x 2 superstructures which are typically observed in oxygen deficient manganites. [156]

CV measurements show the presence of a reversible redox process at the surface of PCMO electrodes in the doping range $0.3 \leq x \leq 0.5$ near E^0 (Mn^{4+}/Mn^{2+})$\approx$ 0.76 eV vers. SHE [157] at pH = 7. By taking into account our in situ observations of the Mn L edges, this indicates a near surface vacancy formation process according to $Pr_{1-x}Ca_xMn^{3+x}O_3 + 2e \leftrightarrow Pr_{1-x}Ca_xMn^{2+x}O_{2.5} + V_O" + \frac{1}{2}O_2$ at a redox potential of E_P^0 (Mn^{4+}/Mn^{2+}) $\approx$ 1 V vers. SHE. Compared to E^0 for MnO_2/MnO this is slightly enhanced due to the increased stability of the perovskite structure. [158] The observed initial decrease of the current density in chronoamperometry measurement at U = 1.43 V vers. SHE (supporting information Figure 3.9) by a factor of 3 can possibly be attributed to surface oxygen vacancy formation. Since the creation of oxygen vacancies leads to doping by two electrons per vacancy, a significant decrease of the work function

is expected by incorporation of oxygen vacancies. Indeed, Beyreuther et al. observe a decrease of φ by 1 - 1.7 eV in $La_{0.7}Ca_{0.3}MnO_{3-\delta}$ and $La_{0.7}Ce_{0.3}MnO_{3-\delta}$ for $\delta \approx 0.5$ - 0.7. [159] Because oxygen vacancies represent electron donors, their formation energy increases with the energy difference between the upper edge of the O $2p$ band and the Fermi level.

The presence of a band gap, such as for $CaMnO_3$, therefore hamper the oxygen vacancy formation and may facilitate phase separation into Ca-rich and Mn-rich phases with a subsequent corrosive decomposition of the oxide. In contrast, the "metal like" valence band at intermediate doping can be continuously filled up with electrons. The resulting increase of E_F may slow down the electrode reduction and facilitate O_2 evolution activity by an increasing Mn $3d - e_g$ occupation (Figure 3.7 lower panel).

Although under ETEM conditions, the determination of equilibrium potentials for a redox reaction measured versus a reference electrode is not possible, our experiments show similar trends in ex situ and in situ experiments. We therefore suggest that both the formation of oxygen deficient phases as well as oxygen evolution from water splitting can be driven by the positive overpotential η which develops under electron beam stimulation.

3.3.4 Corrosion Phenomena

Many perovskites are only stable during water splitting in alkaline media. Under electrochemical stimulation at pH = 7 oxygen evolution via water splitting can be counteracted by corrosive phase changes. Parallel trends are observed in CV and ETEM experiments, showing pronounced corrosion in Ca rich samples. In the CV and chronoamperometry experiments, we observe dissolution of Pr/Ca cations in the electrolyte after cycling to sufficiently negative potential with respect to E_p^0 (Mn^{2+}/Mn^{4+}). A-site cation dissolution and electrode corrosion is typically observed for other perovskites in a range of E^0 ($LaBO_3/La^{3+}$) $\approx$ 0.2 - 0.35 eV vers. SHE. [160] The presence of a MnO_x surface layer at the corroded electrodes (see supporting information Figure 3.9d) suggests a reaction according to $AMnO_3{+}3H_2O \leftrightarrow A^{n+}(aq){+}MnO_{2-y}{+}(1{+}y/2)O_2 + 2H_3O^+ + 2e$ as a typical corrosion reaction for perovskites in acidic aqueous solution.

In the ETEM studies, we observe by EELS analysis that degradation via recrystallization and amorphization in Ca-rich samples is accompanied by a Ca depletion of the reacted zones. The diffraction patterns of the Ca-depleted recrystallized areas are compatible with a cubic Ca-Mn-O phase which is subsequently transformed into MnO rich amorphous areas. This resembles the formation of Mn oxide in the ex situ voltammetry experiments due to A-site cation dissolution in the electrolyte. The suppression of the corrosion reaction via a negative potential in the in situ ETEM experiment directly rules out that knock - on damage is the main driving force for corrosion and gives strong evidence for the presence of electrochemically driven corrosion.

Corrosive behavior is increased for Ca-rich manganites due to reduced phase stability.

Indeed, the formation enthalpy of A-site doped manganites decreases with increasing Mn valence. [161] Undoped $CaMnO_3$ has only a very narrow stability range in the pseudo-binary CaO-MnO phase diagram and can easily decompose into Ca-rich and Mn-rich phases. [162] The decomposition kinetics can be strongly influenced by the defect chemistry of the catalyst in its active state: Because oxygen vacancy formation may be less favorable in the single phase $CaMnO_3$ perovskite with a band gap, it can easily drive the phase decomposition and thus may play an important role in the catalyst corrosion.

3.4 Conclusions

Although manganites exhibit relatively large overpotentials for electro-catalytic O_2 evolution (e.g. in comparison to RuO_2), they represent interesting model systems for the study of the role of e g doping, covalency and defect chemistry on catalytic activity. In particular, we observe that near surface oxygen vacancies are formed in neutral conditions (pH = 7) which decrease the Mn valence and thus increase the e_g occupation. This may be essential for the observed reduced oxygen evolution activity compared to expectations of activity based on the equilibrium e_g doping level. First steps in understanding electron beam driven electrochemical processes in an ETEM are demonstrated, where we observe oxygen evolution activity as well as corrosive decomposition. The suppression of O_2 evolution as well as corrosive processes via a negative potential in the in situ ETEM electrochemical cell, directly rules out that knock-on damage is the main driving force for corrosion and supports our conclusions that catalysis as well as corrosion is driven by a positive electrical potential. We find that subtle band structure effects such as the splitting of the Mn $3d - e_g$ states and changes in the character of the hole states have an impact on charge transfer during water oxidation and may decide whether oxygen vacancy formation is assisting catalysis or corrosion. Our findings may stimulate more detailed and atomic level studies on the role of oxygen vacancies for catalytic activity in perovskites. We expect that strategies which can stabilize non-equilibrium concentrations of defects in the active state of the catalyst and can thereby improve the catalytic activity without corrosion are of high importance for the future optimization of catalyst materials.

3.5 Experimental Section

Sample Preparation:
Bulk $Pr_{1-x}Ca_xMnO_3$ samples (x =0.32, 0.8, 0.95, 1.0) were prepared via a grinding and sintering process starting from a stoichiometric mixture of dry Pr_6O_{11}, $CaCO_3$, and Mn_2O_3 powder. After repeated milling in a ball mill and calcination in air, cold-pressing and closing sintering at 1370 K for 48h, the polycrystalline samples reveal only the orthorhombic phase (space group: Pbnm) with a small amount of the charge-ordered $P2_1nm$ PCMO for $x = 0.32$ but no secondary phases. From the bulk sample electron-transparent specimens were prepared by a polishing and dimpling process and a final single-sided Ar ion etching at 3 kV at an angle of 12°. The sample used for electrochemical

TEM (Figure 3.6) was cut via focused-ion-beam (FIB) in a FEI Nova Nanolab 600 using Ga ions with energies ranging from 30keV and 7nA (initial cuts) to 5keV and 29pA (final Ga-milling). Finally, Ar ion etching at 3 kV at an angle of 12° is performed in order to minimize the amount of FIB-damages sample volume. Depending on the position, grains with diameter of several 100 nm can reveal well-crystalline edges as well as amorphous edges. This indicates that irradiation damage like oxygen vacancies cannot be completely excluded. The samples were glued either on a copper grid or on a tantalum ring and electrically grounded to minimize electric charging effects.

$Pr_{1-x}Ca_xMnO_3$ thin films ($x = 0 - 0.8$) for CV studies were deposited by ion-beam-sputtering at a deposition temperature of $T_{dep} = 795$°C and an oxygen partial pressure of $p_{O_2} = 10^{-4}$ mbar. 400 nm thick PCMO films with different Ca contents were deposited on almost single-crystalline Pt templates on [100] MgO, in order to obtain a conducting back-contact. The PCMO films are predominantly [001] orientated but typically twinned, leading to a [110]-orientated volume fraction. [111] misorientations in the Pt give rise to a volume fraction of [112] grains in the PCMO. Inspection of the PCMO films via optical and scanning electron microscopy shows complete coverage of the template without any holes or cracks. Undoped $CaMnO_3$ films ($x = 1$) have been excluded from this study because they have not been successfully prepared as single phase material.

In situ ETEM Experiments and Electron Loss Spectroscopy:
A C_s image-corrected FEI Titan 80 - 300 kV electron microscope with a point resolution of 0.08 nm including a differentially pumped environmental cell is used for electron diffraction, high-resolution imaging and electron energy loss spectroscopy (EELS). The base pressure without gas injection is 10^{-6} mbar. Water injection is performed by inlet of He gas bubbled through distilled water. The total pressure during exposure amounts to 1.3 mbar with an estimated H_2O partial pressure of 0.013 mbar. In order to study chemical reactions at catalyst-vapor interfaces, a gaseous sacrificial Si-containing compound is used. In preliminary experiments, we observed that SiH_4 is present as an impurity in the sample chamber. The correlation between silane oxidation to solid amorphous SiO_{2-x} by sufficient amounts of evolving oxygen at crystalline catalyst surfaces is used for systematic studies of the catalytic water splitting activity in a series of 8 PCMO samples with different doping levels (x =0, 0.32, 0.8, 0.95 and 1). High-resolution bright field imaging is performed on PCMO grains orientated to a low index zone axis.
A Gatan Tridiem energy filter for Electron Energy Loss Spectroscopy (EELS) and elemental mapping is installed. For high spatial resolution of $\sim$ 1.5 nm EELS measurements are performed in the scanning TEM mode with an energy resolution of 1.2 eV in high vacuum before and after the gas exposure. For details of the analysis of the Mn L edge, see supporting information. EDX line scans shown in the supporting information Figure 3.9 are performed in a Philips CM12 electron microscope at 120 keV in the scanning TEM mode with a spatial resolution of $\sim$ 10 nm and an energy resolution of 130 eV.

Electrochemical Cell within the ETEM:
An electrochemical cell is realized within the ETEM sample chamber using a sample holder which includes a piezo-controlled STM Pt/Ir tip (Nanofactory). It allows for application of a bias voltage to the electron-transparent sample and to use the Pt/Ir tip in contact with specific sample areas as the counter electrode. Bias voltages between - 1.5 V and + 1.5 V applied to the TEM sample are suitable to control electrochemical reactions of a catalyst. The tip acting as a counter electrode remains grounded.

In Situ XANES Measurements:
The X-ray absorption spectra (XANES) were recorded using tunable monochromatic radiation from the ISISS (Innovative Station for In Situ Spectroscopy) beamline at the synchrotron radiation facility BESSY II (Berliner Elektronenspeicherringgesellschaft für Synchrotronstrahlung). The monochromator slit was set to 60 μm, corresponding to an energy resolution of about 0.2 eV. The spot size at the sample was 150 by 200 μm. Epitaxial PCMO thin film samples ($x = 0.32$) on Pt/MgO were positioned about 2 mm away from a 1 mm aperture, which is the entrance to the differentially-pumped electrostatic lens system separating gas molecules from photoelectrons focused toward the hemispherical analyzer (PHOIBOS 150, SPECS GmbH). The experimental setup is described in more detail elsewhere. [162] Experiments were performed in ultra high vacuum (UHV) and in H_2O vapor (flow of 3 ml/min. at 0.1 mbar). Sample 1 was put in to the UHV chamber without additional surface treatment and the Mn L core near edge features were measured in UHV and in H_2O vapor with an applied bias of + 1.3 V. Sample 2 was treated ex situ in H_2O (dest.) for 2 h. It was then exposed to Ar^+ sputtering in $1.3 \cdot 10^{-4}$ mbar Ar for 12 min in the transfer chamber to remove surface carbon. After stabilization of H_2O pressure, an external bias of + 1.3 and + 1.8 V, respectively, was applied to the sample. The spectra presented here show the Auger electron yield (AEY). The intensities have been normalized with respect to the impinging photon flux.

Acknowledgments This research carried out in part at the Center for Functional Nanomaterials, Brookhaven National Laboratory, which is supported by the U.S. Department of Energy, Office of Basic Energy Sciences, under Contract No. DE-AC02-98CH10886. Research in Göttingen is supported by the DFG within the SFB 602. Financial support of the Research at TU Clausthal by the DFG through FOR 1346 is gratefully acknowledged. The XANES measurements performed at HZB/BESSY II (Helmholtz-Zentrum Berlin) were performed in collaboration with Rosita Arrigo and Axel Knop-Gericke from FHI (Fritz-Haber-Institute of the Max-Planck-Society Berlin). We gratefully acknowledge the Differential Mass Spectroscopy measurements and valuable discussion about electrochemistry with P. Bogdanoff and S. Fiechter, Institute of Solar Fuels, Helmholtz-Center for Materials and Energy, Berlin. Valuable discussions with M. Beleggia, Technical University of Denmark, Center for Electron Nanoscopy about electron-sample interactions are gratefully acknowledged.

3.6 Supporting Information

3.6.1 Electrochemical Characterization

Experimental

The electrochemical cell for cyclic voltammetry consists of a $Pr_{1-x}Ca_xMnO_3$ thin film electrode and a Pt counter-electrode in a 0.1 M Na_2SO_4 electrolyte (pH 7) at a fixed temperature of about 22°C. This electrolyte was chosen to study catalytic activity under neutral pH conditions although the ability for pH buffering is less pronounced as for e.g. choosing KOH as electrolyte. We assume, however, that this choice enables a more realistic comparison to in situ ETEM measurements in H_2O vapor, where equal values of the concentrations of H^+ and OH^- ions can be assumed.

An Ivium Compactstat potentiostat was employed to measure the potential versus an Ag/AgCl standard electrode. The $Pr_{1-x}Ca_xMnO_3$ films on MgO/Pt were embedded in a synthetic resin to exclude direct electrochemical contact between the current leads or back-contacts and the electrolyte. The $Pr_{1-x}Ca_xMnO_3$/Pt/MgO stack is electrically connected via a PVC coated Cu wire. The free $Pr_{1-x}Ca_xMnO_3$ surface which is in contact with the electrolyte has a size of 4 x 9 mm^2. For the calculation of current densities, the free surface was used as active electrode area. No roughness corrections have been performed, since SEM and TEM inspection before and after voltammetry measurements have shown that the films are flat and the roughness does change the electrode area only by about 20% which is within the error level of the measurement.

For the analysis of oxygen evolution, differential mass spectroscopy (DEMS) was applied at the Institute of Solar Fuels, Helmholtz-Center for Materials and Energy, Berlin. Here, 0.5 M K_2SO_4 was used as electrolyte at pH=6.8 and a temperature of 22°C. The epitaxial films are pressed against a membrane with a thin liquid electrolyte layer in between. Since the pH cannot be buffered in this configuration, measurements are performed only at relatively low current densities up to 0.2 mA/cm^2.

Cyclic Voltammetry

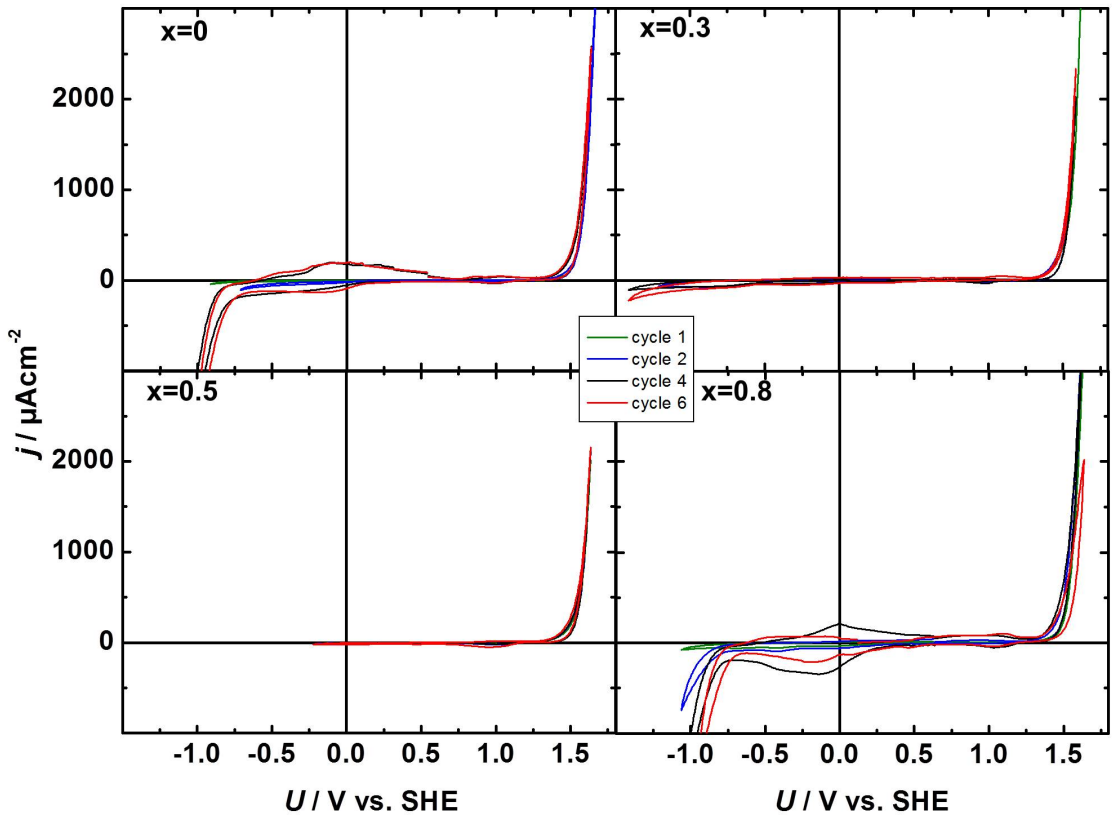

FIG. 3.8 Cyclovoltammetry measurements of $Pr_{1-x}Ca_xMnO_3$ films with doping level of $x = 0,\ 0.32,\ 0.5$ and 0.8, measured at 5 mV/s. For all doping levels, oxygen evolution at positive potential and hydrogen evolution at negative potential is observed. Hydrogen evolution is directly related to a rapid corrosive decomposition of the oxide electrodes at slightly negative potential for all doping levels. There are two additional peaks at about $U_0 = +0.1 - 0.3$ V and $U_0 = +1.05$ V. Since we study oxygen evolution, in the following we consider only positive potentials.

3.6.2 Chronoamperometry and Stability of the Electrodes

Electron diffraction of the film shown in Fig. 3.9b shows the presence of a Pbnm structure, however superstructures due to oxygen deficiency and vacancy ordering are observed at several places (not shown here). In contrast, chronoamperometry measurement at $U = 0.9$ V vers. SHE shows negative currents (not shown here) which indicate a rapid reductive decomposition of the electrode also confirmed by TEM analysis. In the TEM, we observe amorphization in large areas and formation of large pores (see Fig. 3.9d). EDX analysis of this film reveals pronounced A-site depletion in all amorphous regions. A-site cation dissolution is also confirmed by chemical analysis of the dried electrolyte

by EDX.

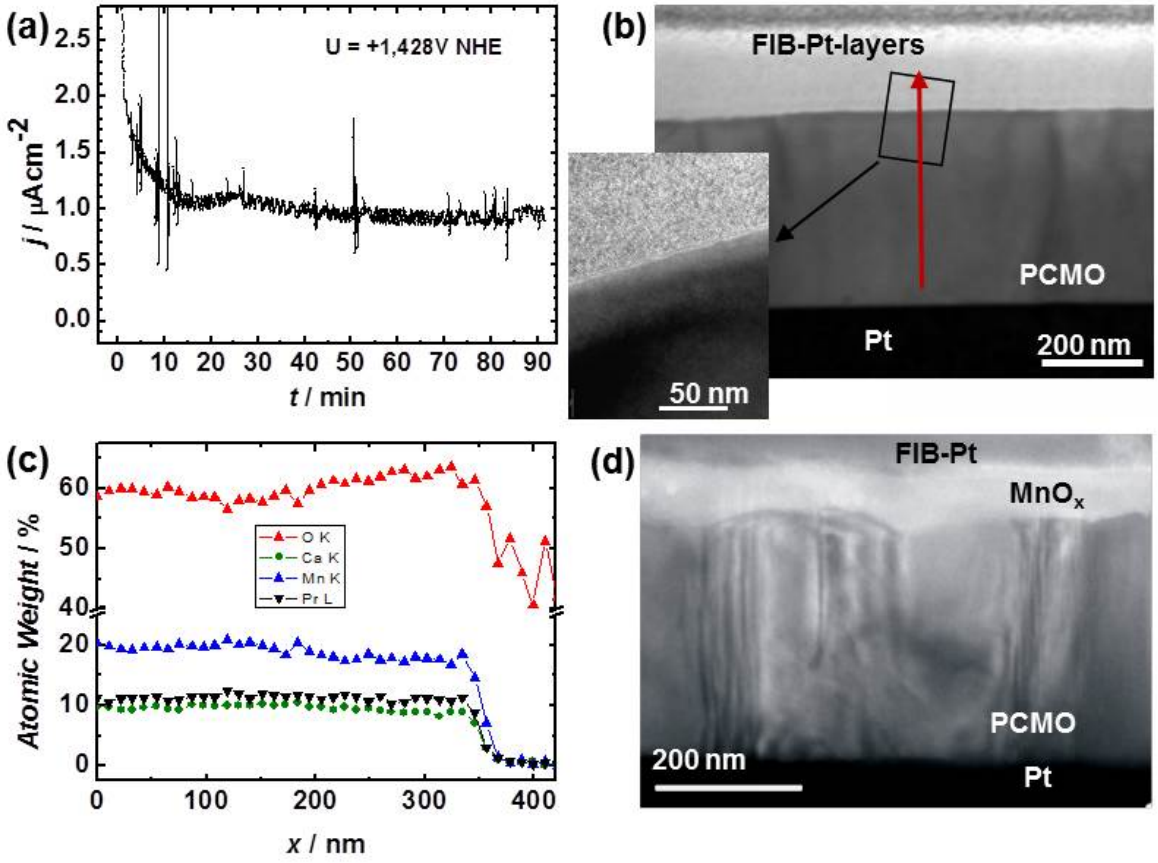

FIG. 3.9 (a) Chronoamperometry measurement during oxygen evolution of a $Pr_{0.5}Ca_{0.5}MnO_3$ electrode at $U = 1.428$ V vers. SHE. The current density decreases from $\sim 3\mu A/cm^2$ to $\sim 1\mu A/cm^2$ within the first 15 min and then does not show any further change within 90 min. (b) Bright field STEM image of the film, inset: TEM image of the near surface region of the film. The red arrow marks the position of the EDX line scan shown in (c). The atomic weight of the O-K, Ca-K, Mn-K reveals no change in cation stoichiometry near the surface. (d) TEM image of $Pr_{0.5}Ca_{0.5}MnO_3$ after Chronoamperometry measurements at $U = 0.89$ V vs. SHE shows an A-site depleted amorphous Mn-O-surface layer.

3.6.3 Determination of the Exchange Current Density for Oxygen Evolution

The exchange current density j_0 is determined at a set of $Pr_{1-x}Ca_xMnO_3$ film electrodes, where significant corrosion at negative potentials has been avoided. The values are determined by extrapolating the current density at $U > 1.5$ V vers. SHE to the thermodynamically required voltage for oxygen evolution at pH = 7 (0.82 V vers. SHE). For a film at $x = 0.5$, the change of the determined j_0 at different $j-V$ cycles and different sweep rates was studied. We see an increase with increasing sweep rate but no drastic dependence on

the cycle number. Extrapolation of j_0 to vanishing sweep rate gives $j_0 = (3.36 \pm 3.77)$ nA/cm^2 (Figure 3.10).

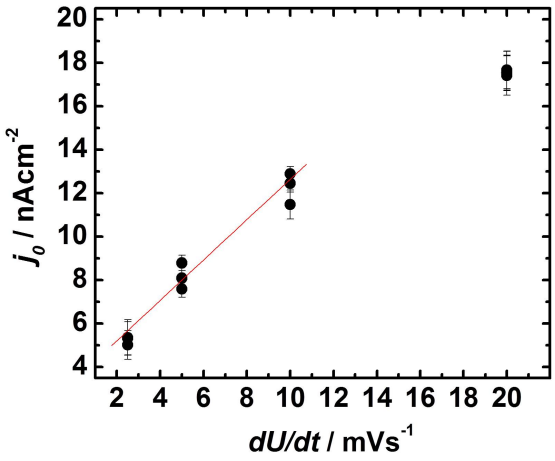

FIG. 3.10 Determination of exchange current density for $x = 0.5$ as a function of sweep rate dU/dt. Extrapolation to $dU/dt = 0$ enables us to separate capacitive contributions from true oxygen evolution. However, an influence of pH drift during the measurement cannot be excluded. The value at a sweep rate of 20 mV/s is not considered for the extrapolation since pronounced hysteric effects at this sweep rate due to pH changes adulterate the determination of j_0.

3.6.4 Control Experiment on the Absence of Catalytic Activity at Amorphous PCMO ($x = 0.32$) Edges

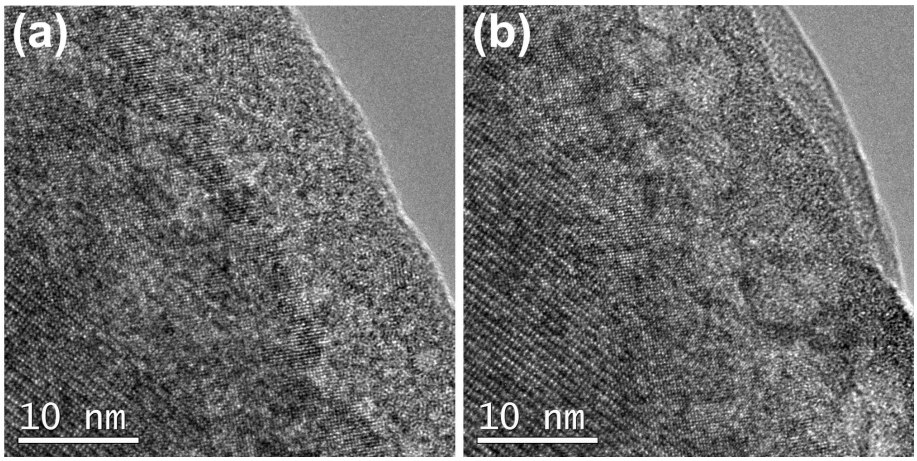

FIG. 3.11 Absence of SiO_{2-x} growth at an amorphous PCMO ($x = 0.32$) edge at the same sample and conditions, where SiO_{2-x} growth is observed at crystalline PCMO edges. (a) initial state in $He/H_2O/SiH_4$ vapor $\sim$ 2 s after shifting the electron beam to this area (b) same area in the gas mixture $\sim$ 100 s later. Inspection by EELS shows that the amorphous area in (b) is composed of Pr, Ca, Mn and O. SiO_{2-x} is absent.

3.6.5 Documentation of Dynamic Observations in the ETEM

Movies available on http://www.onlinelibrary.wiley.com/doi/10.1002/adfm.201103173/full show dynamic observation of characteristic processes at PCMO of different doping level in the ETEM. All movies represent a series of bright field TEM images and were recorded under the same conditions, i.e. in a He/H_2O gas mixture under electron beam dose of $5 \cdot 10^4 e/(Å^2 s)$. The total gas pressure is 1.3 mbar, and the H_2O partial pressure is estimated to be about 0.013 mbar. The SiH_4 compound in the vapor is present for all experiments. Images are acquired with a frame rate of 1/s and acquisition time of 0.2 s. All movies are shown in real time.

Movie M1. *Dynamic observation of SiO_{2-x} growth at a crystalline PCMO ($x = 0.32$) edge:*

The movie M1 shows the electron beam and water exposure induced growth of a SiO_{2-x} amorphous layer at the surface of a crystalline PCMO ($x = 0.32$) grain imaged at [001] zone axis. At 26 s the sample edge is moved towards the image center, in order to compensate for drift. The 2 x 2 superstructure modulation can be seen in the modulation of the lattice fringe contrast. It is already visible at some locations during the initial state and becomes more pronounced during the acquisition of the movie.

Movie M2. *Dynamic observation of competition between SiO_{2-x} growth and interface recession due to corrosion at PCMO ($x = 0.32$):*

The movie M2 shows a series of bright field ETEM images of a crystalline PCMO ($x = 0.32$) interface in the [201] orientation. The sample is moved $\sim$ 8-12 s after start of the experiment in order to readjust the interface to the center of the image. Detailed EELS analysis of the amorphous-crystalline interface after the ETEM experiment shows that the amorphous phase only contains Si and O, whereas the crystalline phase contains Pr, Ca, Mn and O. The higher spatial resolution of this series of images allows us for the identification of corrosion processes at the PCMO/SiO_{2-x} interface (see Fig. 3 in the main article). The average value of the growth rate of the SiO_{2-x} layer and the rate of interface recession were determined to be $\sim$ 10 nm/min and $\sim$ 1.8 nm/min, respectively.

Movie M3. *Dynamic observation of fast corrosion at PCMO ($x = 0.95$):*

The movie M3 shows a series of bright field ETEM images of a pristine crystalline PCMO edge ($x = 0.95$). The movie starts $\sim$ 15s after beginning of the electron beam exposure in water vapor and shows a thin amorphous SiO_{2-x} layer which disappears during the corrosion. It shows dynamic recrystallization under the electron flux followed by amorphization of the PCMO.

3.6.6 Electronic Structure of $Pr_{1-x}Ca_xMnO_3$

Details of the electronic structure calculations

We performed electronic structure calculations based on density functional theory (DFT) [113] using a local hybrid functional PBE0^r. The basis of this functional is the PBE functional. [119] Part (1/4) of the exchange term is replaced by the explicit Hartree-Fock exchange term as in the PBE0 hybrid functional. [163] In the PBE0^r

functional only onsite exchange terms are considered. The calculations have been performed with the projector augmented wave method [115] as implemented in the CP-PAW code. [164]

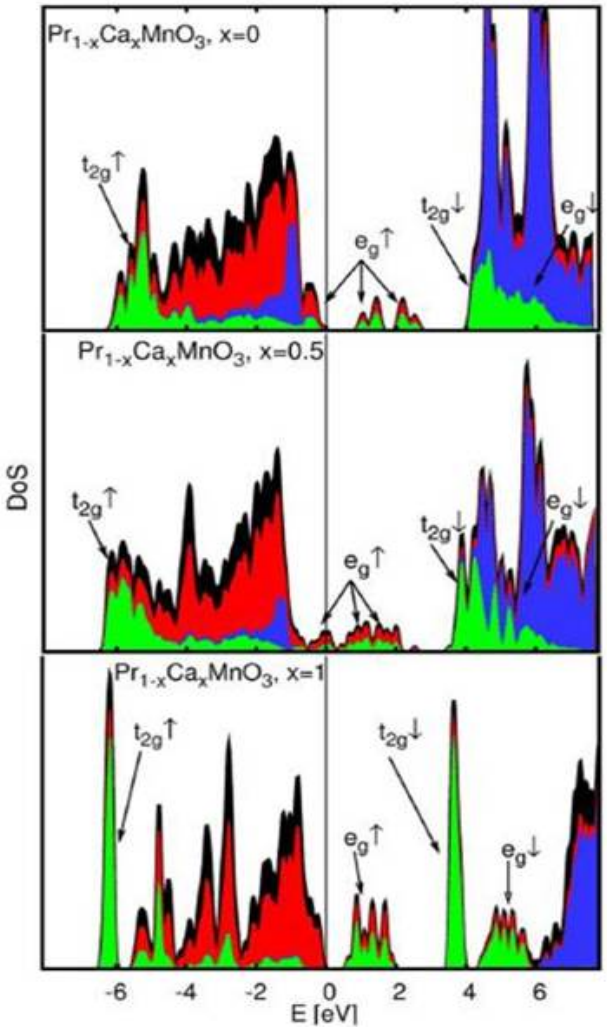

FIG. 3.12 Density of states for $PrMnO_3$ (top), $Pr_{0.5}Ca_{0.5}MnO_3$ (middle) and $CaMnO_3$ (bottom). The green area describes the contribution of Mn d states, the blue area corresponds to the Pr d and f states and the red area corresponds to the weight of O $2p$ states. Black are other contributions. The vertical at $E = 0$ eV indicates the top edge of the valence band or the Fermi level, respectively, which is relevant for the transport of hole carriers. For $CaMnO_3$ ($x = 1$), holes are of pure oxygen character, while for $x < 1$ the states near the Fermi level are Mn $3d - e_g$ O $2p$ anti-bonding states.

The plane wave cutoff has been set to 40 Ry for $x = 0$ and $x = 0.5$ and to 50 Ry for $x = 1$. A 3 x 4 x 3 k-point grid has been used for the orthorhombic cells ($x = 0,\ 0.5$) and a 8 x 8 x 8 grid for the smaller cell for $x = 1$. The $5s$ and $5p$ semi-core electrons of Pr and the $3s$ and $3p$ semi-core electrons of Ca have been treated explicitly as valence electrons. For Pr we used a $2s2p2d2f$ augmentation. This notation implies that $2s$-type, $2p$-type, $2d$-type and $2f$-type projector functions and

partial waves have been used per magnetic and spin quantum number. For Ca we used a $2s2p2d$ augmentation, for Mn a $2s2p2d$ augmentation and for O a $2s2p1d$ augmentation.

For $x = 0$ and $x = 0.5$, the orthorhombic structure with 4 formula units per unit cell and an AF-A type ordering of the magnetic moments has been used. For $x = 1$, the orthorhombic distortion is small and has been ignored. Here, we start with an AF-G FCC unit cell with 2 formula units in the unit cell. Lattice parameters and atomic positions were fully relaxed. A detailed comparison of the calculated DOS with experimental spectroscopic data is in preparation.

Band Structure of PCMO

The results of DFT band structure calculations at three doping levels $x = 0$, 0.5 and 1 are shown in Fig. 3.12. Due to the large on-site Coulomb interaction there is a large splitting between the t_{2g} and the e_g band, so that the t_{2g} band is located at the lower edge or even below the oxygen $2p$ valence band, while the partially empty e_g band is located above. Using conventional density functional calculations, the t_{2g} band is erroneously located at the top of the oxygen p-band. Only methods explicitly including the large Coulomb repulsion, such as LDA+U or hybrid density functionals, shift the occupied t_{2g} bands to low energies and thus lead to the proper description of the manganites as charge transfer insulators. We find the occupied Pr-f states in the upper part of the oxygen band. The empty Pr states lie far above the e_g band, in the region of the Mn d states with the minority spin direction.
We find for $CaMnO_3$ a calculated band gap of 0.8 eV which is a little smaller than the experimental gap of $E_g \approx 1.3 - 1.55$ eV. [102, 106] The observed differences may be also due to unknown exact oxygen stoichiometry. The other limiting case of doping is $PrMnO_3$ with $x = 0$, which is a semiconductor with a calculated band gap of $E_g = 1$ eV in agreement with the measured optical band gap of $E_g \sim 1$ eV. [126]

Work Function of PCMO

The work function of $Pr_{1-x}Ca_xMnO_3$ (x=0.3) was determined by Reagor et al. [165] to $\phi = 4.896$ eV. K. Ebata et al [166] measured the doping dependence of the chemical potential of charge carriers μ by photoemission spectroscopy. $Pr_{1-x}Ca_xMnO_3$ exhibits a sharp drop of μ for $0.2 \geq x \geq 0.3$ and then shows a nearly constant μ up to $x = 0.75$. This is in contrast to $La_{1-x}Sr_xMnO_3$, where a linear decrease of μ over the entire doping range is observed. The Fermi-level pinning in PCMO is a direct confirmation for the shift of spectral weight of the hole states at the top valence band edge from Mn $3d - e_g$ to O $2p$. Taking into account the available data at $x = 0.3$ and for $LaMnO_3$ ($\phi \approx 4.5$ eV), [166] we estimate a work function of undoped $PrMnO_3$ of $\phi \approx 4.5$ eV. The reported work function in nominally undoped $CaMnO_3$ is determined from the built-in potential of $CaMnO_3$/Nb:$SrTiO_3$ hetero-junctions. It varies between 4.8 eV [167] and 5.3 eV. [37] A theoretical value of $\phi = 5.65$ eV is given in Ref. [168] which seems to be too large. Fig. 3.13

compares the doping dependent work function with $E^0(H_2O \rightarrow O_2) = 5.32$ eV for oxygen evolution at pH=7. This suggests that the Fermi-level is always above $E^0(H_2O \rightarrow O_2)$.

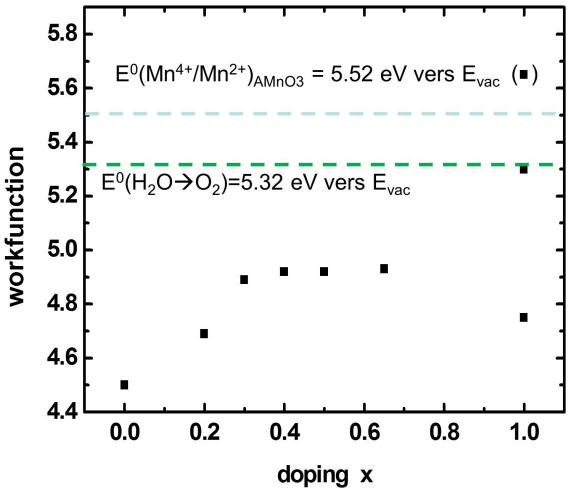

FIG. 3.13 Work functions for $Pr_{1-x}Ca_xMnO_3$ as a function of doping are compared with the equilibrium potential for oxygen evolution at pH=7 $E^0(H_2O \rightarrow O_2) = 5.32$ eV measured with respect to the vacuum level. For details and references see text.

3.6.7 Vulcano-Plot of Perovskite Oxides Including PCMO

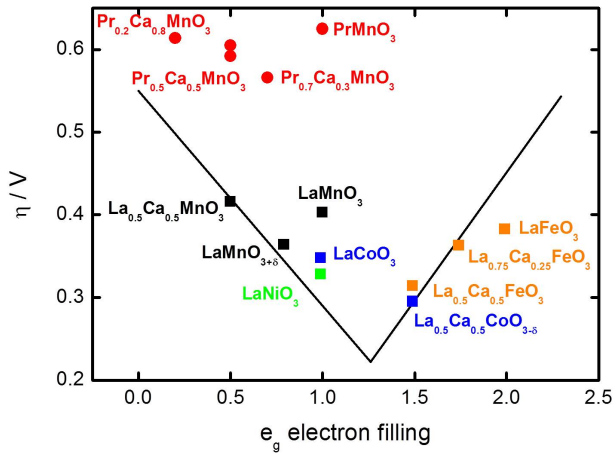

FIG. 3.14 Overpotential at $j = 50\mu A/cm^2$ vs. e_g-filling for A-site doped perovskites. Square symbols and the 'volcano plot line' at pH=13 were taken from Ref. [2]. Circles represent our data on $Pr_{1-x}Ca_xMnO_3$ at pH=7.

3.6.8 Making Water Splitting Visible by Silane Oxidation: The Supporting Observations by In Situ Mass Spectrometry

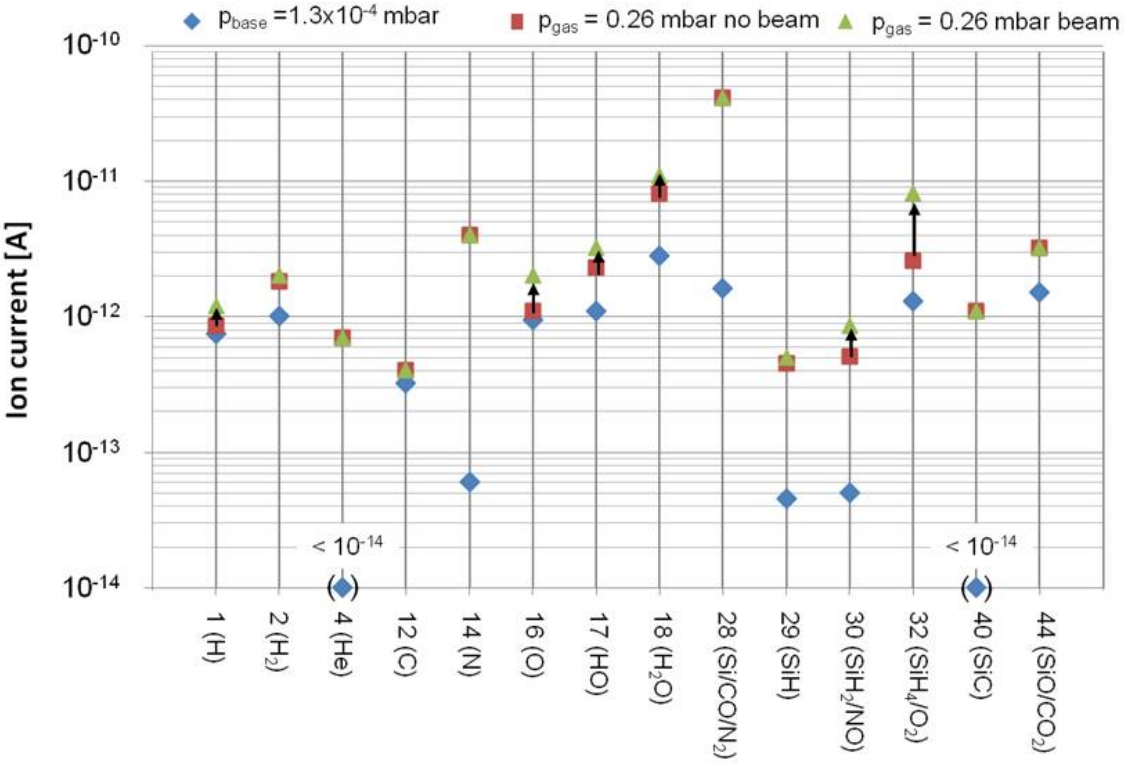

FIG. 3.15 Mass spectroscopy of the changes in gas composition induced by electron beam stimulation of the $Pr_{1-x}Ca_xMnO_3$ catalyst. Shown are the ion currents in three different states of the experiment: (i) after switching to ETEM mode at the base pressure of $p_{base} = 1.3 \cdot 10^{-4}$ mbar; (ii) at working pressure of the used $He/H_2O/SiH_x$ mixture with blanked electron beam at 0.26 mbar and during exposition of the catalyst with the electron beam (after waiting 5 min for diffusion of the reaction products during the differential pumping stage). Black arrows indicate the major concentration changes during sample stimulation.

In air, SiH_4 exhibits an exothermic reaction with O_2 ($\Delta H = -1518$ kJ/mol) or water ($\Delta H = -374$ kJ/mol) [169] to form SiO_2. However, the latter reaction does not spontaneously take place under ETEM conditions using a He/H_2O mixture at a total pressure of $p = 0.26$ mbar and a water partial pressure of roughly $p_{H_2O} = 0.026$ mbar. This can be concluded from our observations that SiO_{2-x} formation requires the presence of a catalytically active sample. SiO_{2-x} formation is never observed spontaneously.
Consequently, SiO_{2-x} must be formed via electrochemical oxidation at an active electrode. We consider the two alternative half reactions at the PCMO electrodes.

a) Catalysis of the direct reaction with H_2O:

$$SiH_4 + 2H_2O \rightarrow SiO_2 + 8H^+ + 8e^- \tag{3.1}$$

b) Oxygen evolution from water splitting and subsequent silane oxidation:

$$2H_2O \rightarrow O_2 + 4H^+ + 4e^- \tag{3.2}$$

$$SiH_4 + O_2 \rightarrow SiO_2 + 4H^+ + 4e^- \tag{3.3}$$

From the analysis of Fig. 3.15, we can make the following statements:

- Injection of the He gas mixture increases the background concentration of all measured impurities.
- Due to mass channel overlap, SiH_x compounds can be uniquely measured only at the channel 29 (SiH).
- Injection of the gas mixture does not change the level of channel 16 (O) but doubles channel 32 (O_2) from $1.3{\cdot}10^{-12}$ A to $2.6{\cdot}10^{-12}$ A. Since atomic oxygen is produced by the ionization process in the mass spectrometer, one expects that changes in channels 16 and 32 must be proportional. This indicates that the increase in channel 32 during gas injection (and beam shifted off the sample) is mainly due to the increase in the SiH_4 compound.
- Stimulation of the PCMO catalyst by the electron beam leads to a significant enhancement of channel 16 (O), channel 30 (SiH_2 or NO) and channel 32 (O_2 and SiH_4). From the simultaneous increase of channel 16 (O) and 32 (O_2), we conclude that the increase in channel 32 is dominated by the O_2. Also channel 1 with atomic H and channel 17 (HO) is slightly increased, whereas channels which are not involved in the relevant chemical reactions (He, N, Si/CO/N_2, SiC, SiO/CO_2) remain stable within 5%.
- There is an increase in H_2O partial pressure during catalysis which is due to recombination of H+ with oxygen in the sample chamber and/or mass spectrometer. The only possible explanation is that hydrogen which stems from SiH_4 oxidation can react with oxygen. This supports our overall reaction model, i.e. that oxygen evolution from water splitting according to reaction channel (3.2) is involved in electrocatalysis.

The observations clearly support our conclusions about the origin of the SiO_{2-x} growth on catalytically active surfaces. The increase in O and O_2 indicates significant oxygen evolution during electron beam stimulation of the sample according to reaction (3.2). However, we cannot completely rule out that some SiH_4 oxidation also takes place via reaction (3.1) or that other transition states of SiH_x (see e.g. [170]) may be involved.

3.6.9 EELS Analysis of Mn L_{23}-Edges

Different methods for extracting the L_{23} ratio are discussed in the literature. [171] For a reliable extraction of the Mn-L_3,L_2 intensity ratio (L_{23}-ratio) an accurate background subtraction is necessary. In accordance to the method explained by Varela et al. [172], a power law background have been fit to an energy loss interval of 50 eV before the Mn-L_3 onset. The continuum contribution has been subtracted by scaling a Hartree-Slater cross section function [173] available in Gatan Digital Micrograph to a spectrum interval of 10 eV placed right to the L_2-edge. Subsequently the L_{23}-ratio is determined from the integral intensities of L_3 and L_2-feature and the Mn oxidation state is obtained by comparison with the results gained by Varela et al. with Ca-doped $LaMnO_3$. Since the chemical activity is accompanied by the formation of SiO_{2-x}, the O K features of the manganite are not unambiguously accessible. Consequently, the EELS analysis is restricted to the intensity ratio of the Mn L_3,L_2-edges.

CHAPTER 4

Environmental TEM Study of Electron Beam Induced Electrochemistry of $Pr_{0.64}Ca_{0.36}MnO_3$ Catalysts for Oxygen Evolution

---

S. Mildner, M. Beleggia, D. Mierwaldt, T. W. Hansen, J. B. Wagner, S. Yazdi, T. Kasama, J. Ciston, Y. Zhu, and C. Jooss
Journal of Physical Chemistry C **119**, 5301-5310, February 9, 2015
DOI: 10.1021/jp511628c

ABSTRACT Environmental transmission electron microscopy (ETEM) studies offer great potential for gathering atomic scale information on the electronic state of electrodes in contact with reactants. It also poses big challenges due to the impact of the high energy electron beam. In this article, we present an ETEM study of a $Pr_{0.64}Ca_{0.36}MnO_3$ (PCMO) thin film electrocatalyst for water splitting and oxygen evolution in contact with water vapor. We show by means of off-axis electron holography and electrostatic modeling that the electron beam gives rise to a positive electric sample potential due to secondary electron emission. The value of the electric potential depends on the primary electron flux, the sample's electric conductivity and grounding, and gas properties. We present evidence that two observed electrochemical reactions are driven by a beam induced electrostatic potential of the order of a volt. The first reaction is an anodic oxidation of oxygen depleted amorphous PCMO which results in recrystallization of the oxide. The second reaction is oxygen evolution which can be detected by the oxidation of a silane additive and formation of SiO_{2-y} at catalytically active surfaces. The quantification of beam induced potentials is an important step for future controlled electrochemical experiments in an ETEM.

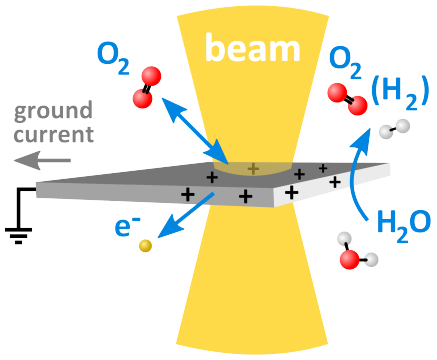

4.1 Introduction

Electrocatalysts are of high importance in speeding up electrochemical reactions via the control of reaction steps and lowering activation barriers. [174] Typically, electrocatalysts are used in the form of electrodes which enable the transfer of electric charges into adsorbed reactants. Ideally, catalysts are involved in the catalyzed electrochemical reaction without being consumed or corroded. Consequently, high catalytic performance requires materials with a sufficiently flexible atomic electronic surface structure in order to facilitate the reaction processes. [175,176] In their active state, catalysts often undergo significant changes in surface and defect structure. A recent example even shows that a water splitting electrocatalyst can be formed in operando. [27] Whether the catalyst forms desired highly active states, undergoes undesired changes reducing its activity, or even shows irreversible corrosion can strongly depend on the specific ambient conditions. In situ atomic scale studies of electrocatalysts under working conditions can contribute substantially in providing insights into the underlying reaction mechanism. [177–179]

Environmental transmission electron microscopy (ETEM) studies using aberration corrected microscopes offer the opportunity for real space atomic resolution studies of catalysts at local pressures of several millibars. [80, 148–150, 180] The high spatial resolution capabilities can be combined with a variety of analytical methods for chemical and band structure analysis, e.g., local X-ray and electron energy-loss spectroscopy (EELS). [81] The opportunity for real time observations of catalysts in operando by a high-energy electron probe poses a great challenge for well-defined studies of electrochemistry due to the need for understanding and controlling the effect of the electron beam on the catalyst state.

Generally, the electron beam affects the studied sample via inelastic collisions of high-energy electrons with atoms. The appearance of atomic displacements is controlled by the ratio between the energy transfer of back-scattered electrons to the atoms and their displacement energy and thus is a function of the atomic mass and the energy of the primary electrons. [91] Point defect generation sets in above a threshold value of the primary electron energy depending on the sample material. In addition to atomic displacements, inelastic scattering of high-energy electrons with specimen electrons can give rise to a variety of excitations such as plasmons, [181] secondary electron emission, [151] and even sample heating or point defect generation due to radiolysis [91] at high electron fluxes. Since electrocatalytic activity essentially depends on the electric potential of the catalyst, the effect of electrostatic charging due to the emission of secondary, core, and Auger electrons must be addressed carefully. A beam induced potential of the order of the redox potential of a catalyzed chemical reaction may have a tremendous effect on the sample state. Understanding such effects quantitatively may allow for developing strategies toward controlled electrochemistry in an ETEM.

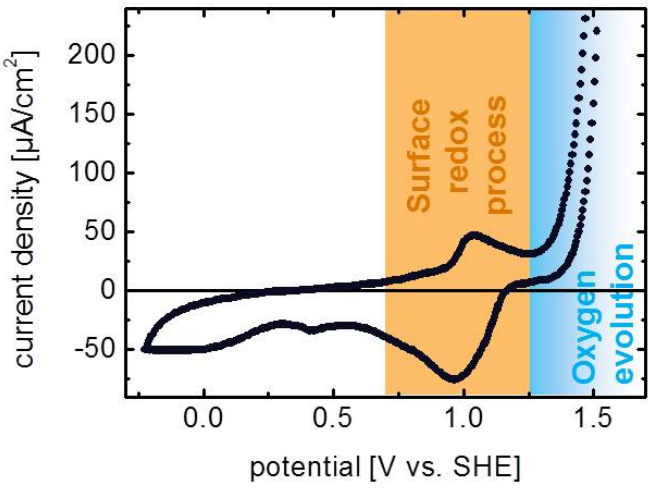

FIG. 4.1 Cyclovoltammetry measurement (in pH = 7) shows two electrochemical reactions: catalyst surface oxidation/reduction due to oxygen intercalation at $V \approx 1$ V and oxygen evolution at $V \approx 1.5$ V.

We here present a study of electron beam induced electrochemistry using a manganese-based perovskite oxide catalyst for oxygen evolution. Perovskite oxides for electrocatalytic oxygen evolution have attracted appreciable attention during the past decades [3] and particularly in recent literature. [2,146,182] Especially manganese-based oxides are in the focus of current research due to their affinity to the active manganese-calcium complex in the natural Photosystem II and the flexible oxidation state of manganese. [183] In this article, hole-doped perovskite $Pr_{1-x}Ca_xMnO_3$ ($x = 0.36$) has been selected as model catalyst for electrocatalytic oxygen evolution. Previous cyclovoltammetry measurements in liquid electrolyte in a standard three-electrode configuration reveal two well-characterized redox reactions (Figure 4.1): (i) stable O_2 evolution at positive potential of $V > 1.4$ V versus standard hydrogen electrode (SHE) at neutral pH in liquid electrolytes [3, 184] and (ii) a reversible surface redox process at a potential of $V \approx 1$ V versus SHE due to generation and annihilation of oxygen vacancies. [185] Topotactic intercalation of oxygen at anodic currents just below the O_2 evolution potential is typical for many transition metal oxides. [186]

In a previous study, we have shown that sacrificial SiH_4 in the ETEM visualizes O_2 evolution activity by the growth of amorphous SiO_{2-y} at active PCMO. [185] Under the chosen experimental conditions, SiO_{2-y} growth requires O_2 evolution and thus evolves via $SiH_4 + 2O_2 \rightarrow SiO_2 + 2H_2O$. In that study, a beam-induced electrochemical corrosion process in a Ca-rich PCMO sample was halted by applying a negative potential of $V \approx -1$ V to the sample, which was in good electric contact with a biasing sample holder. We thus concluded that beam induced potentials of the order of 1 V have driven the observed reactions and that the underlying mechanisms are of electrochemical nature.

The main goal of the study presented here is to shed light on the electron beam induced electrostatic potential and its impact on the selected electrochemical model reactions. The beam induced electric potential is measured by electron holography combined with electrostatic modeling. In contrast to the electron-transparent lamellae of our previous study, where polycrystalline PCMO was glued onto metallic sample carriers, we use here cross-section lamellae cut by focused ion beam (FIB) from high quality epitaxial PCMO thin films grown on MgO substrates. The electric back-contact of the PCMO electrode via insulating MgO suggests high beam induced potentials even at low electron fluxes as applied in holography. However, this assumption was disproved by direct resistivity measurements of MgO TEM lamellae cut by FIB. Our article is organized as follows: In section 4.3.1, we present ETEM oxidation studies of surface oxygen depleted PCMO in pure water vapor. This is followed by an ETEM oxygen evolution study of nominally fully oxygenized PCMO in a $He/H_2O/SiH_4$ gas mixture in section 4.3.2. Off-axis electron holography measurements of beam induced electrostatic sample charging are shown in section 4.3.3. In section 4.4.1, the recorded phase shift in vacuum near the sample edges at variable electron flux is analyzed by electrostatic modeling. This allows for an estimation of the amount of injected charge at steady-state conditions as well as the resulting beam induced electric potential. Section 4.4.2 presents the discussion of structural and chemical modifications of PCMO observed in the ETEM in the presence of gas in the framework of beam induced electrochemistry. Finally, a summary and conclusion is given in section 4.5.

4.2 Materials and Methods

The in situ ETEM study is carried out on electron transparent samples which are cut from an epitaxial [001] oriented 480 nm thick $Pr_{0.64}Ca_{0.36}MnO_3$ (PCMO) thin film with some [110] twin domains (orientations are given normal to the substrate surface). Twin domains are unavoidably present due to the orthorhombic structure of the PCMO. The film was prepared using reactive ion beam sputtering (IBS) on MgO [001] substrate at a deposition temperature of 1050 K in oxygen atmosphere with a partial pressure of $p_{O_2} = 1.4 \cdot 10^{-4}$ mbar during deposition. A subsequent annealing procedure at $T = 1200$ K in air for 20 h was performed in order to improve crystal quality and oxygen content. Protection layers consisting of Al_2O_3 (900 nm) and Au (900 nm) were deposited via IBS at room temperature on the PCMO film in order to avoid beam damage during TEM sample preparation.

By means of focused ion beam (FIB; FEI Nova Nanolab 600), electron transparent samples in cross-section geometry were cut out of the film and mounted on a copper sample support. The lamellae is further divided into several elements by cutting notches using low-energy (5 keV) ions. A final milling process using a precision ion polishing system (PIPS) with low-energy argon ions provides highly crystalline sample edges (see Figure 4.8 in the Supporting Information).
ETEM and EELS experiments in vacuum and water containing gas with partial pressures of $p_{H_2O} = 1 - 150$ μbar are performed in an aberration corrected FEI Titan electron mi-

croscope with an environmental cell using 300 keV electrons with different flux densities. EEL spectra of the manganese L-edge were used to determine the Mn oxidation state before and after water exposure.

Energy dispersive X-ray (EDX) spectra after gas exposure were acquired in a Philips CM12 electron microscope with scanning (STEM) capability operated at 120 keV. Characteristic X-rays were detected with a Si drift detector from Oxford with an energy resolution of 136 eV. Details on the experimental methods and basic TEM characterization of the sample are provided in the Supporting Information.

4.3 Results

All presented ETEM studies were performed using a 300 keV electron beam due to optimum high-resolution imaging conditions in H_2O vapor environments. Fully oxidized PCMO shows high stability under 300 keV electron irradiation at high-vacuum conditions (typically better than 10^{-6} mbar). Even in high-resolution STEM and EELS with electron fluxes as high as 10^{10} $e/(Å^2s)$, we have not found any indication of beam damage.

4.3.1 PCMO Oxidation in Pure Water Vapor.

A crystalline, approximately 50 nm thick sample was selected for this study. Initially, parts of the sample are covered by a 3 nm thick oxygen depleted surface layer of ion beam damaged amorphous PCMO (Figure 4.2a).
The thickness of this layer was measured under high-vacuum conditions, where no changes were observed on time scales of 30 min during irradiation with 300 keV electrons. During the exposure to pure water vapor at a pressure of $p_{H_2O} = 1$ μbar and electron flux of 9000 $e/(Å^2s)$, the amorphous edges start to recrystallize (Figure 4.2b). Recrystallization of thin amorphous areas also affects the surfaces normal to the electron beam as indicated by the inhomogeneous image contrast, while keeping a crystalline Pbnm structure (Figure 4.2b). The corresponding Fourier transform (inset) shows that the initially sharp spots which belong to the Pbnm structure become diffuse. An increase of the pressure to $p_{H_2O} = 5$ μbar during exposure to 5000 $e/(Å^2s)$ results in minor changes of the morphology of the recrystallized areas. Figure 4.2c shows the state after a total of 20 min exposure to H_2O and the electron beam (10 min in $p_{H_2O} = 1$ μbar and 10 min in $p_{H_2O} = 5$ μbar, respectively). The HRTEM image reveals the existence of misoriented, recrystallized domains with a size < 5 nm. The corresponding Fourier transform exhibits a further circle-shaped spreading of the Pbnm spots as well as the appearance of some additional spots. These observations clearly indicate the formation of nanometer-sized crystalline domains with misorientation angles $< 30°$ (see the inset of Figure 4.2c) by crystallization of the former amorphous areas of the sample surface.

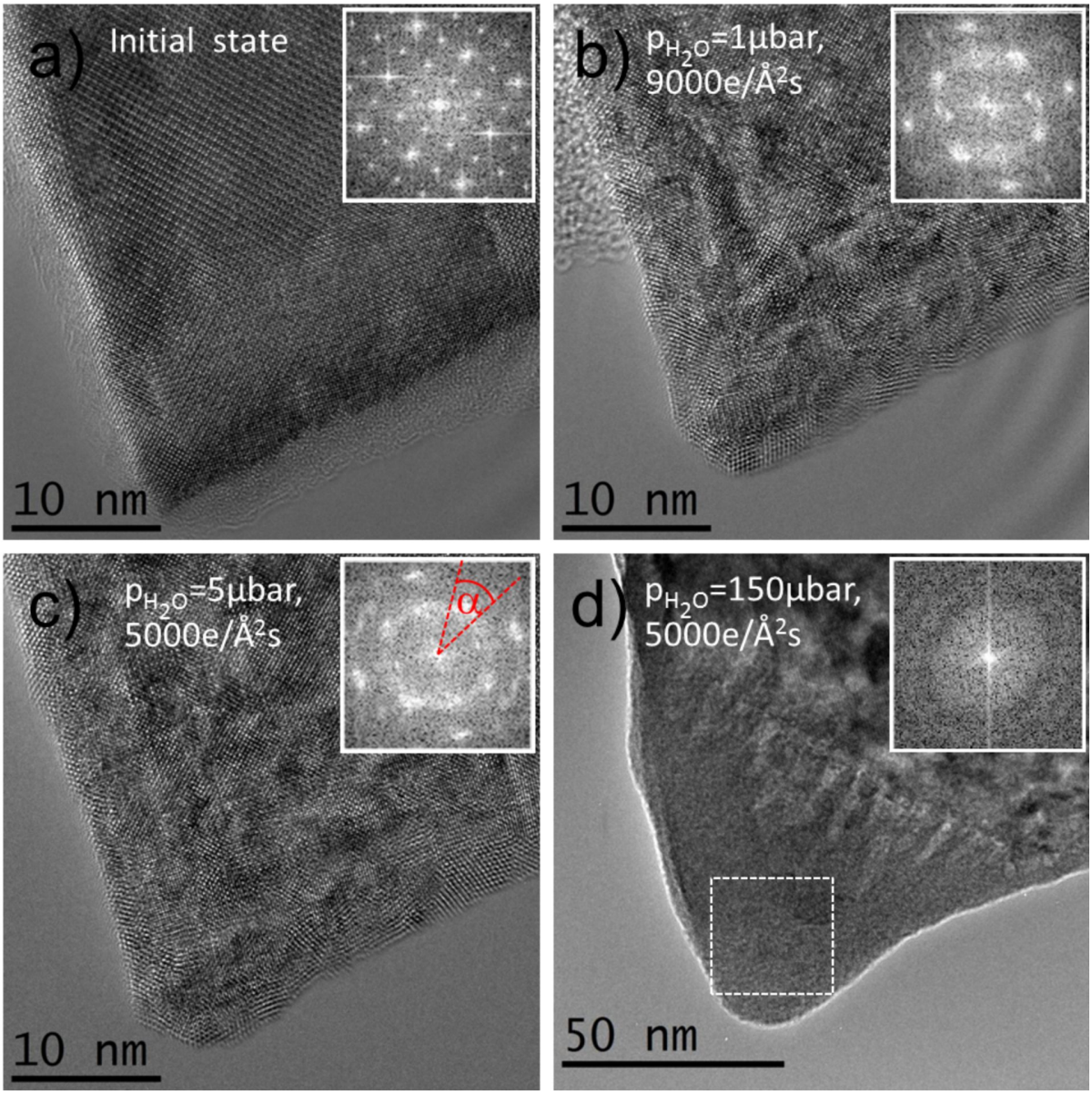

FIG. 4.2 HRTEM images of a crystalline edge of the PCMO film in different water pressure environments and electron fluxes. (a) Initial state in high vacuum. (b) State after 10 min in $p_{\mathrm{H_2O}} = 1$ μbar with electron flux of 9000 $e/(\text{Å}^2\text{s})$. (c) Same area 10 min after increasing the pressure to 5 μbar in a flux of 5000 $e/(\text{Å}^2\text{s})$. (d) Phase transition to amorphous state after enhancement of the pressure to 150 μbar at 5000 $e/(\text{Å}^2\text{s})$. The insets show the corresponding Fourier transformed images. In the FFT in (c) the initially sharp spots are blurred within an angle of $\alpha = 30°$. The dashed square in (d) marks the region used for the FFT.

The stability of the catalyst against beam-induced corrosion is only maintained for low water pressure. An increase of the pressure to $p_{\mathrm{H_2O}} = 150$ μbar at 5000 $e/(\text{Å}^2\text{s})$ results in a phase transition to an amorphous structure in electron-irradiated regions after a few minutes.

Figure 4.2d was recorded after high vacuum conditions were re-established. The observed processes cease as water vapor is evacuated from the microscope chamber. Thus, a recrystallization of initially amorphous edges via growth of misoriented nanocrystals requires a water pressure of $\sim 1 - 10$ μbar whereas a pressure increase to > 100 μbar results in amorphization of the former crystalline lattice. The interface between crystalline and amorphous material in Figure 4.2d roughly corresponds to the boundary of the electron beam profile. Post-characterization of the entire specimen confirms that such structural modifications only occur in regions exposed to the electron beam.

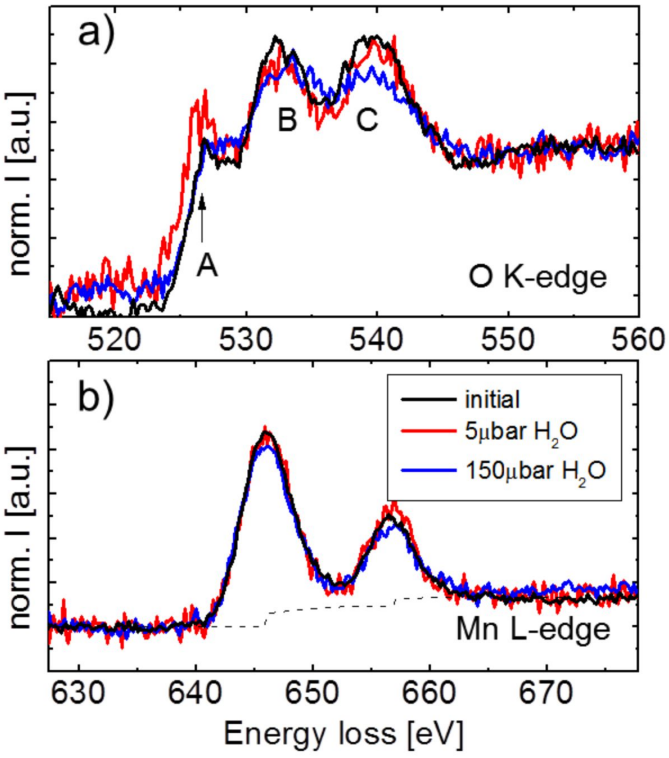

FIG. 4.3 Postmortem ELNES studies of the changes of characteristic loss edges after contact with water vapor. (a) O K-edge and (b) Mn L-edge. Initial state (black), after 5 μbar water exposure (red), and the amorphous state after 150 μbar water exposure (blue).

Electron energy-loss near edge structure (ELNES) of the oxygen K-edge and the manganese L-edge were measured in the initial state, after exposure to 5 μbar water vapor and after amorphization in 150 μbar water vapor (Figure 4.3).
The O K-edge (Figure 4.3a) exhibits three sub-features labeled A, B, and C, which are well-known for manganites. The pre-peak (feature A) arises from a hybridization of the O $2p$ with the e_g majority spin states and is sensitive to carrier doping and bonding characteristics. Feature B can be attributed to hybridization with anti-bonding minority spin Mn-$3d$ as well as Pr states. Feature C is related to hybridization with Pr, Ca,

and Mn states of higher energy. The O K-edge of the FIB/PIPS virgin sample shows a relatively small pre-peak feature (A) compared to other results on conventionally prepared manganite TEM lamellae at $x \approx 0.3$ measured with TEM which are obtained in the literature. [172, 187] We attribute this to surface oxygen depletion to FIB TEM sample preparation. Oxygen vacancies are known as electron donors filling the majority e_g states in manganites. The exposure to low-pressure water vapor ($\leq$ 5 μbar) results in an intensity increase of the O K-pre-peak (A). This implies a depletion of majority e_g states, i.e., an increase of hole doping due to oxygen vacancy healing. In contrast, subsequent exposure to 150 μbar water vapor results in a decrease of pre-peak intensity to roughly the initial value, thus indicating oxygen depletion during amorphization.

Figure 4.3b shows the Mn L_3- and L_2-edges (white lines) at 646 and 656 eV. We use the Gaussian fitting method for the determination of the $I(L_3)/I(L_2)$ intensity ratio which is a measure for the Mn valence state [171] (for details see 4.6.2 in the Supporting Information). We find an initial $I(L_3)/I(L_2)$ ratio of 2.2. The resulting Mn valence state of +3.4 agrees with the nominal valence state expected from doping (+3.36). While O K-pre-edge (feature A) shows a clear increase after 5 μbar water exposure, only marginal changes of the Mn L-edge, i.e., a slight increase of the $I(L_3)/I(L_2)$ intensity ratio, are visible. In contrast, the corrosive amorphization of PCMO during exposure to 150 μbar water vapor results in stronger changes of both in the Mn L- and in the O K-edges. The Mn $I(L_3)/I(L_2)$ intensity ratio increases to 2.5, indicating a decrease of the Mn valence to +2.8. Simultaneously, the intensity of the O K-pre-edge decreases, and there is a significant reduction of the (C) peak which is due to hybridization of O and A-site cations. This change may indicate an incipient decomposition of the PCMO perovskite into other metal oxide compounds accompanied by a change in the Mn valence state and the A-site cation configuration (see 4.6.2 in the Supporting Information).

4.3.2 Using SiO_{2-y} Growth for Monitoring Oxygen Evolution at PCMO.

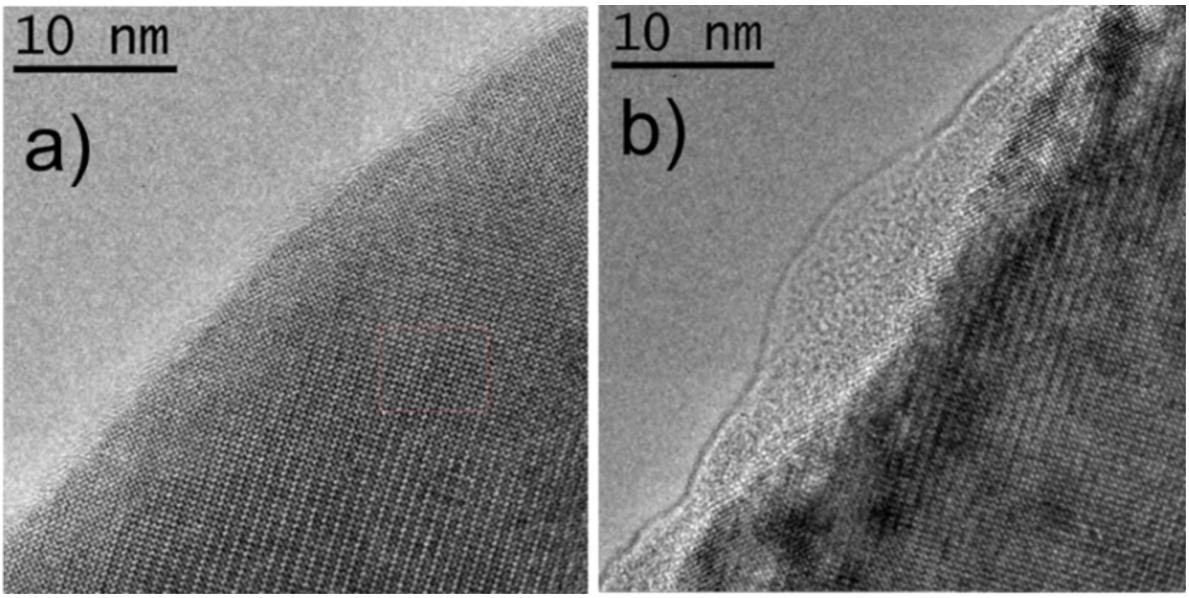

FIG. 4.4 Crystalline edge of the PCMO film (a) in vacuum and (b)after $t \sim 120$ s in $H_2O/He/SiH_4$ gas ($p = 0.3$ mbar) in an electron flux of 11 000 $e/(Å^2s)$. The amorphous outgrowth in (b) represents SiO_{2-y}.

Figure 4.4 demonstrates the development of a virgin sample region during exposure to 11 000 $e/(Å^2s)$ in 0.3 mbar of a $He/H_2O/SiH_4$ gas mixture containing 1% H_2O vapor ($p_{H_2O} \approx 3\ \mu$bar).
Figure 4.4a depicts the initial state of a crystalline edge. After a few seconds of electron illumination in gas the growth of amorphous material at the crystalline edges is observed. The state after 120 s in the gas is shown in Figure 4.4b. Using EELS and EDX spectroscopy, the amorphous outgrowth is identified as SiO_{2-y}. The growth of SiO_{2-y} is only observed under the following specific conditions:

(i) It requires the presence of crystalline PCMO edges. If the same experiment is performed at amorphous PCMO edges or at catalytically nonactive materials such as the copper sample support, no growth of SiO_{2-y} is observed.

(ii) Exposing crystalline PCMO to the $He/H_2O/SiH_4$ mixture but without electron irradiation, the growth of SiO_{2-y} is absent. It is also absent if we move the electron beam away from the sample, where the high-energy electrons interact only with the gas in the sample chamber. Consequently, the stimulation of the catalyst by the high-energy electron beam is essential for the catalytic reaction at PCMO in the TEM.

(iii) SiO_{2-y} growth on PCMO requires water vapor, since neither structural modification in PCMO nor SiO_{2-y}growth is observed during the pre-characterization with

electrons in high vacuum despite the presence of the SiH_4 impurity. Mass spectroscopy data (not shown here) reveal the presence of SiH_4 gas even in high-vacuum mode. [185] Thus, we can exclude a direct electron beam driven reaction between PCMO species and SiH_4.

These three observations are fully consistent with previously reported results for PCMO TEM lamellae cut from bulk material and show that SiO_{2-y} growth under these conditions can be considered as an indicator for oxygen evolution. [185]

Local ELNES spectra of the O K-edge and the Mn L-edge before and after the reaction in $He/H_2O/SiH_4$ gas (Figure 4.9) in the Supporting Information) reveal a pronounced increase of the Mn $I(L_3)/I(L_2)$ ratio after the reaction. The disappearance of the O K-pre-peak and the decrease of the Mn oxidation state from initially 3.3 to 2.4[1] after the reaction are in accordance with the observation of the formation of oxygen vacancies during the active state of PCMO bulk material as seen in previous ETEM experiments [185] and confirmed by in situ XANES. [28] See also 4.6.9 in the Supporting Information.

Figure 4.5 shows the SiO_{2-y} coverage of PCMO after exposure to 0.3 mbar of the gas mixture in and nearby electron-exposed areas at two different electron fluxes. The yellow circle marks the diameter of the electron beam during gas exposure. Figure 4.5a shows a bright-field STEM image of the studied sample region 15 min after irradiation with 11 000 $e/(Å^2s)$. The corresponding EDX-mapping of the Si-$K_{\alpha 1}$ line in Figure 4.5b reveals a significant Si concentration present in and nearby the beam area at maximum $\approx$ 200 nm from the beam center. In all areas, where Si is found by EDX mapping, it exists in the form of SiO_{2-y} which covers the PCMO sample as confirmed by EELS (not shown here). Figure 4.5c,d shows another sample area which has been exposed to the same gas mixture and pressure as before at a reduced electron flux of 2000 $e/(Å^2s)$ for $t \approx 7$ min. Here, we also observe the growth of SiO_{2-y}. In contrary to the experiment with 11 000 $e/(Å^2s)$, EDX mapping in Figure 4.5d shows a Si signal only in the area exposed to the electron beam.

[1] Notably, one should avoid to overrate the significance of the absolute value of the Mn oxidation state determined from ELNES of the Mn L-edge because it suffers systematic errors originating from the determination via comparison of our experimental $I(L_3)/I(L_2)$ ratio with literature results of finite accuracy. However, the observed trends of the $I(L_3)/I(L_2)$ ratio measured under similar experimental conditions are definitely reliable and clearly prove a reduction of PCMO after $He/H_2O/SiH_4$ exposure even though the absolute oxidation state value may be underestimated.

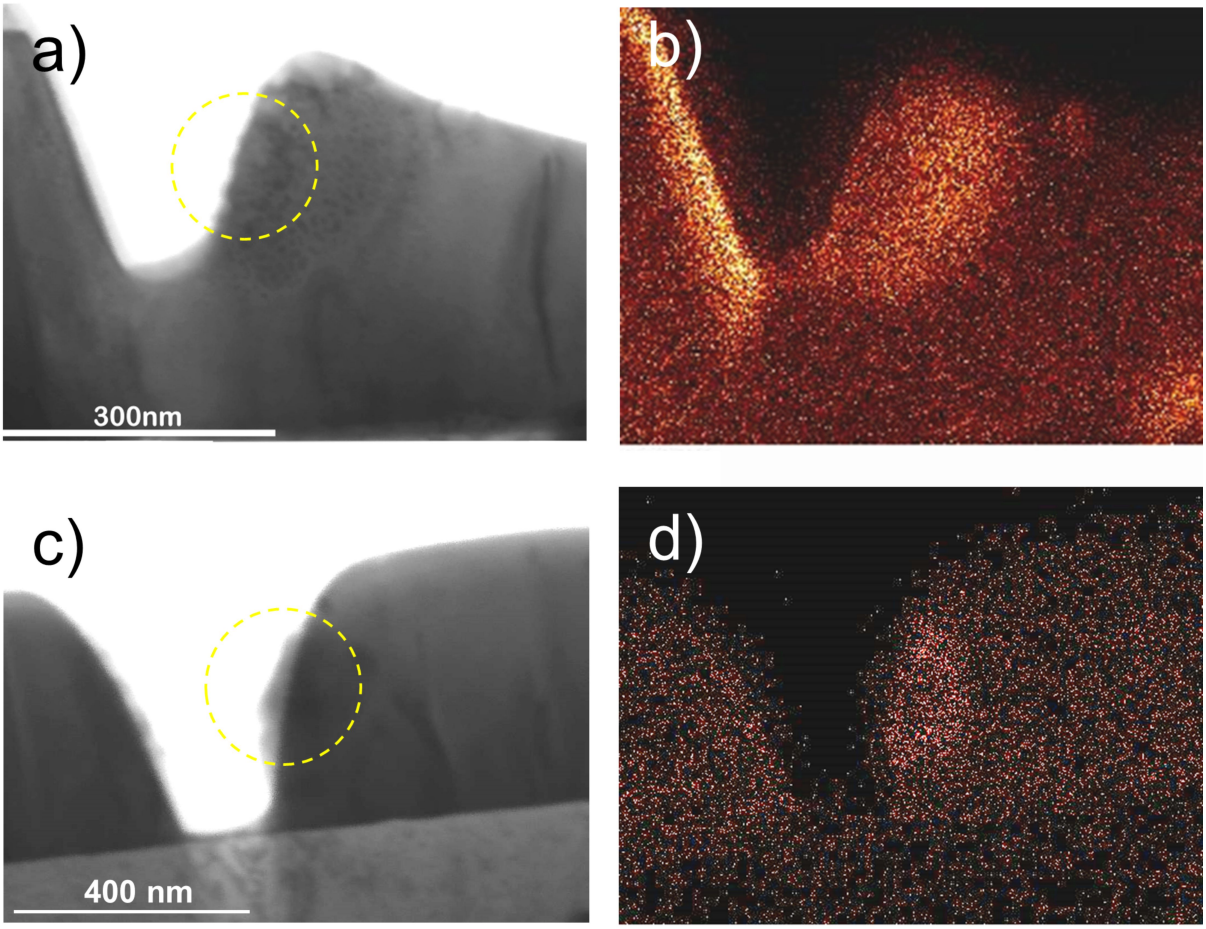

FIG. 4.5 Analysis of the effect of different electron fluxes on the oxygen evolution activity. (a) A bright-field STEM image of a reacted PCMO region after electron irradiation with 11 000 $e/(\text{Å}^2\text{s})$ in the $He/H_2O/SiH_4$ gas. The yellow circle marks the electron beam position and size during gas exposure. (b) The corresponding EDX count map of the Si-$K_{\alpha 1}$ emission shows maximum Si signal in regions adjacent to beam position. (c) Bright-field STEM image of another region of the same specimen which was treated under same conditions as the sample region depicted in (a) but with decreased electron intensity of 2000 $e/(\text{Å}^2\text{s})$. (d) The corresponding EDX count map reveals a Si signal only in the primarily electron irradiated region.

4.3.3 Off-Axis Electron Holography for Investigation of Electron Beam Induced Electrostatic Potentials

Off-axis electron holography experiments in combination with an approximate model of the potential distribution were carried out to measure the beam-induced potential values at the PCMO surface. Off-axis electron holography is based on the determination of the phase shifts of electron waves traversing a region interspersed by an electrostatic or magnetic field. A more detailed description of this method and the experimental setup can be found in the Supporting Information part 4.6.3.
A general relation between the electrostatic potential $V(x, y, z)$ and the phase modulation

of the electron wavefront $\varphi(x, y)$ can be obtained by solving the Schrödinger equation describing an initially plane electron wave propagating along the optical axis z through an electrostatic field $-\text{grad}[V(x, y, z)]$. Taking into account relativistic effects and neglecting dynamic diffraction as well as inelastic scattering, the phase shift of the electron beam after passing through the sample is

$$\varphi(x, y) = C_E \int_{-\infty}^{+\infty} V(x, y, z) \mathrm{d}z \tag{4.1}$$

The constant C_E depends on the accelerating voltage of the microscope used: at 300 kV it has a value of $C_E = 6.53$ rad/(Vμm). Within the sample interior, the phase shift originates from two contributions to the total electrostatic potential: the partially screened Coulomb potential of the atomic nuclei (crystal potential) and the electrostatic potential generated by external charges induced by the beam. We aim at measuring only the second contribution. Consequently, we restrict the analysis of the phase shift to the vacuum next to the sample edge, where the electric potential is only given by the stray field contribution of the charged sample.

Figure 4.6 summarizes the results gained with electron holography at 80 $e/(\text{Å}^2\text{s})$ primary electron flux and introduces the fundamentals of the model used for determination of the electron beam induced potential. The modeling of the phase gradient is subject in section 4.4.1.

Figure 4.6c shows the measured phase shift $\varphi(x, y)$ which is obtained via reconstructing a hologram acquired at a flux of 80 $e/(\text{Å}^2\text{s})$ from the sample area depicted in Figure 4.6a. The red and the green line profiles shown in Figure 6e reveal a positive phase shift near the PCMO surface. Since the effect of the magnetic potential on the electron wave can be disregarded, the spatial dependence of the phase shift in the vacuum area near the sample reflects the electric potential distribution due to the beam induced surface charges of the TEM sample. The phase shift near the surface as a function of primary electron flux exhibits a nonlinear behavior indicating a saturation of charge (Figure 4.6f). According to Eq. 4.1, a positive phase shift proves a positive electron beam induced surface potential. This is in contrast to the situation in scanning electron microscopy (SEM), where the absorption of primary electrons within insulating materials typically results in a negative sample charge. [188]

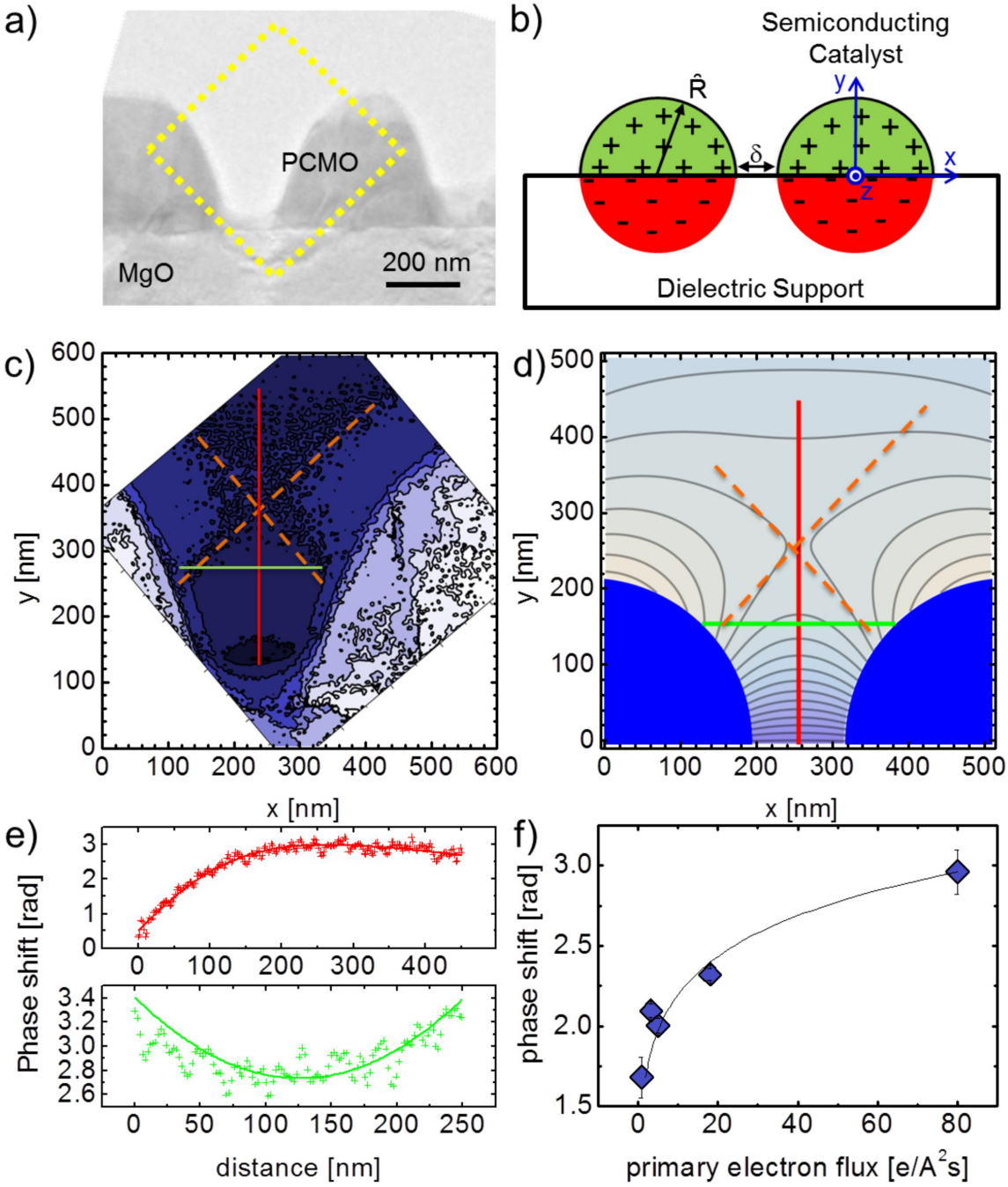

FIG. 4.6 Determination of the beam induced electric potential at the PCMO catalyst protrusions by off-axis holography and electrostatic modeling. (a) TEM image of the sample area used for electron holography. (b) Simple model of the charge distribution within the catalyst/support structure, where the beam-induced positive charges in the catalyst semicylinders with radius $\hat{R}$ and relative displacement ξ are inducing negative counter charges within the dielectric support structure. (c) Experimental contour map of the phase of the electron wave at an electron flux of $\sim 80\ e/(\text{Å}^2\text{s})$ at the sample area marked in(a). (d) Contour map of the calculated phase shift around uniformly charged semicylinders. Note the cross-shaped pattern (saddle point in the potential) indicated by the dashed orange lines in (c) and (d). (e) Fit of the measured phase shifts along the green and red lines depicted in (c) and (d), resulting in $\hat{R} = 215$ nm, $Q = 210$ electrons, and an averaged (over the rim) surface potential of $V = 1.6$ V. (f) The phase shift in vacuum at the PCMO/vacuum interface as a function of the primary electron flux; the black line is a guide to the eye pointing the nonlinear increase of the phase shift with flux.

4.4 Discussion

Our observations of the flux dependent local changes of the PCMO electrocatalyst and the active regions for the SiO_{2-y} formation as an indicator for oxygen evolution activity clearly show a major impact of the electron beam on the catalyst state. In the following, we give a quantitative estimate of the electron beam induced electrostatic potential on the basis of off-axis holography results via electrostatic modeling. We here discuss the extrapolation of holographically measured potentials at low electron flux to potentials occurring under ETEM conditions. Furthermore, we analyze the observed changes of the electrode in more detail and discuss the observations reported above in the framework of electrocatalytic behavior.

4.4.1 Electron Beam Induced Electrostatic Potential

Modeling of the Phase Shift.
In order to understand the observed phase shift $\varphi(x, y)$ and to obtain an estimate of the induced surface potential, we need to model the phase shift in the sample exterior. We note first of all that any charge within the PCMO region, or on its surface, will polarize the (insulating) MgO support, resulting in an induced charge density that also contributes to the phase shift. For simplicity, we assume that the dielectric constant of the support is large enough to result in metal-like behavior; i.e., the induced charges are located at the PCMO-MgO interface, and their electrostatic field is generated by an image (negative) charge positioned mirror-symmetrically with respect to the external (positive) charge (see Figure 4.6b).
Because of the rather high conductivity of highly doped semiconducting PCMO, we expect the PCMO surface to be equipotential; i.e., we expect that all induced charges reside on the outer surfaces S, with a charge density distribution $\rho(r)$ which maintains S equipotential. The self-consistent solution of Poisson's equation

$$\nabla^2 V(r) = -\frac{\rho(r)}{\varepsilon_0 \varepsilon} \tag{4.2}$$

with the appropriate boundary conditions for a surface S of a roughly semicylindrical object of radius $\hat{R}$ and height d requires numerical treatment and cannot be used conveniently for fitting the data.
Therefore, we introduce a further approximation: we assume that the charge is uniformly distributed within S and is mirrored by an image-charge distribution within the MgO support as sketched in Figure 64.6b. With this particular choice of $\rho(r)$, the phase shift comes directly from integrating the equation linking charge density and potential according to Eq. 4.1 along the optical axis z and carrying out the remaining integrations along r and θ.

By superimposing the fields generated by two equal PCMO regions laterally displaced by a gap of $\xi = 110$ nm (as measured from the calibrated experimental data), and by assigning the values $\hat{R} = 215$ nm and a total charge of $Q = 210$ electrons, we obtain

the simulated phase image shown in Figure 4.6d. The parameters $\hat{R}$ and Q were fitted from the phase profiles taken along the red and green lines in Figure 4.6c,d and explained in more detail in paragraph 4.6.7 of the Supporting Information. The final step in the analysis is to extract the potential from the measured charge distribution. Note first that a detrimental side effect of the uniform-charge-density approximation is that the potential of the PCMO regions is not a constant any longer: it varies with the angle along the curved outer surface (rim) as well as with angle and radius over the top and bottom planar surfaces of the PCMO regions. To reconnect with the "sample potential" V, we take an average of the surface potential around the rim, which turns out to be

$$\langle V \rangle = V_S \sum_{m=0}^{+\infty} \frac{C_m}{(2m+1)^2} \tag{4.3}$$

where $V_S = Ne/(4\pi\varepsilon_0\hat{R})$ is the potential which would be established if all the measured charge was distributed over a spherical surface of radius $\hat{R}$, and the coefficients C_m of the capacitance series are given as a sum of Chebyshev polynomials. With the values for $\hat{R}$, $Q = Ne$ as determined above, Eq. 4.3 yields the value $V = \langle V \rangle = 1.6$ V. For details see Supporting Information 4.6.8.

Estimation of the Electrostatic Potential from the Secondary Electron Yield.

In order to establish the connection between electron holography results at low electron fluxes $< 80\ e/(\text{Å}^2\text{s})$ and the ETEM experiments shown in Figures 4.2 and 4.4 at several $10^3\ e/(\text{Å}^2\text{s})$, we propose here a rate equation describing the sample potential as arising from the balance of the electron flux induced emission current of secondary electrons and neutralization currents.

Positive beam induced potentials in TEM samples arise from the emission of secondary (SE), Auger (AE), and core electrons (CE). Altogether they produce a net flow of negative charges directed out of the sample which is partly compensated by neutralization currents via groundings and environment. All currents (emission and neutralization) affecting the specimen charge are summarized in Figure 4.7.

The emission current is proportional to the primary beam current $I_e = I_p Y$, where the proportionality constant Y is the electron emission yield per incident electron. Y depends on the sample potential due to its effect on the escape probability. For simplicity, we only consider the SE contribution to Y, since the cross sections for generating AEs and CEs are much smaller than for SE generation. We estimate Y for SEs emitted from PCMO with energy E according to the equation of the yield spectrum $\mathrm{d}Y/\mathrm{d}E$ given by Chung and Everhart for metals, [189] modified in order to take into account the finite thickness d of the PCMO regions. The yield spectrum is calculated combining the probability (per unit primary path length) of generating a SE in the energy range (E, $E + dE$) multiplied by

the probability for such SE to reach the surface and escape into a vacuum. The resulting spectral yield is given by

$$\frac{\mathrm{d}Y}{\mathrm{d}E}(E,\phi) = 2\frac{S(E)\lambda(E)}{4}\left(1-\exp\left[-\frac{d}{\lambda(E)}\right]\right)\left(1-\frac{E_F+\phi}{E}\right) \tag{4.4}$$

where ϕ is the work function of PCMO and E the energy of the SE relative to the bottom of the conduction band. The probability of beam induced electronic excitations in the specimen is described by $S(E) = C_Y/(E-E_F)^2$, where C_Y is a constant which depends on the energy of the primary electrons and material specific parameters. The factor 2 takes into account the existence of two surfaces, top and bottom surface of the PCMO lamella from which SE are emitted. Integration over all SE energies from vacuum level to infinity gives the total initial yield $Y_0 = 0.0034$ per primary electron of 300 keV for a 50 nm thick PCMO lamella (see Supporting Information part 4.6.4).

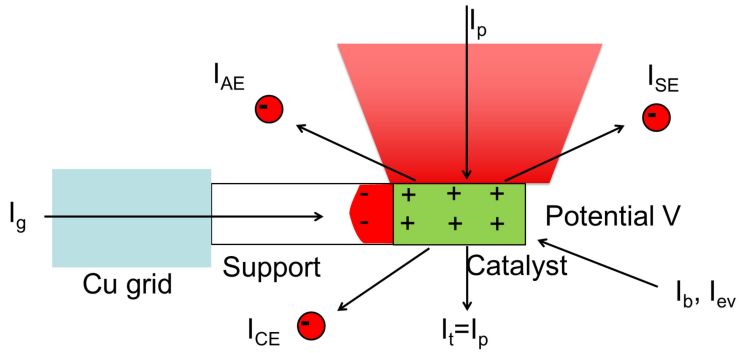

FIG. 4.7 Schematic representation of the generation of beam induced sample potential in a TEM lamella composed of a semiconducting catalyst and an insulating dielectric support. Sample-beam configuration, where the high-energy electron beam with intensity I_p is transmitting the semiconducting catalyst and is creating a positive charge by emission currents I_e of secondary electrons (SE), Auger electrons (AE), and core electrons (CE) due to inelastic scattering processes. In a stationary state, these emission currents are compensated by backflow currents I_b, I_{ev} from gas and other environmental components, and ground currents I_g across the support. Note: the arrows describe the direction of the electron currents and not the conventional current direction.

As charges accumulate inside the sample and build up a potential V, it becomes increasingly difficult to extract further SEs since the escape barrier increases from ϕ to $\phi + eV$ and the yield decreases. The $Y(V)$ curve is obtained by

$$Y(V) = \int_{E_F+\phi+eV}^{+\infty} \mathrm{d}E \frac{\mathrm{d}Y}{\mathrm{d}E}(E,\phi+eV) \tag{4.5}$$

Numerical evaluation of Eq. 4.5 followed by least-squares fitting of the $Y(V)$ curve to the model function $Y_0/(1+v)^\beta$, with $v = V/\phi$, results in $\beta \approx 2.2$ in the experimentally relevant interval $0 < v < 2$. The decrease of Y with V is the origin of a self-limiting process. In absence of the self-limitation, the sample potential in an insulator would

increase linearly with irradiation time.

In general, the energy distribution $\mathrm{d}Y/\mathrm{d}E(E,\phi)$ for insulators and semiconductors is narrower than for metals. [190,191] Thus, with the Chung-Everhart formalism we presumably overestimate the high-energy tail of $\mathrm{d}Y/\mathrm{d}E(E,\phi)$ as well as the value $Y(V)$. Accordingly, we might underestimate the exponent β. A higher value of β implies a stronger decay of $Y(V)$, i.e., an increased impact of the self-limiting effect.
However, the self-limiting process does not fully saturate by itself. Because of the power-law dependence of Y on V, it only changes the time dependence of the potential from linear to logarithmic. Therefore, the establishment of a steady state with a "saturation" potential V requires a neutralization current I_n. The accumulation of a charge q within the sample is governed by the continuity equation

$$\frac{\mathrm{d}q}{\mathrm{d}t} = Y(V)I_p - I_n(V) \tag{4.6}$$

In the stationary state $\mathrm{d}q/\mathrm{d}t = 0$, an equilibrium potential is established, which is given by the intersection of the yield function $Y_0/(1+v)^\beta$ with the current ratio curve $I_n(v)/I_p$.

Comparison of ETEM and Holography Experimental Conditions

For the comparison of beam induced surface potentials determined by holography under HV conditions with beam induced surface potentials under ETEM conditions, the continuity equation (Eq. 4.6) gives a very straightforward approach: assuming that the neutralization current $I_n = V/R(v)$ is controlled by a nonlinear resistance $R(v)$, the balance-of-currents equation reads

$$v(1+v)^\beta = Y_0 I_p R(v)/\phi \tag{4.7}$$

Equation 4.7 gives a nonlinear dependence of the potential V on the primary current as experimentally indicated by the electron flux dependent phase shift in Figure 4.6f. Using $Y_0 = 0.0034$ and $\phi = 4.9$ eV, a positive potential of 1 V at an electron flux of 11 000 $e/(\text{Å}^2\text{s})$ requires a neutralization current of about 100 pA or a sample resistance of the order of $R \approx 10^{10}\ \Omega$. For a smaller sample resistance, for example if the sample is well connected to ground, the potential saturates at smaller values. The opposite limiting case is represented by a floating sample with $1/R = 0$ (regardless of whether the material is metallic or insulating itself). In this limit, the saturation potential would logarithmically depend on the total irradiation time: no steady state would be reached, leading possibly to either arc discharges or dielectric breakdown. In all intermediate cases, a saturation potential of the order of the work function may be expected.

The most difficult quantity in Eq. 4.7 is to estimate a realistic value of the neutralization current and thus the behavior of the resistivity $R(v)$ as a function of potential, gas pressure, and beam conditions. In an ETEM, the neutralization current and thus $R(v)$ can be composed of three contributions $I_n = I_g + I_b + I_{ev}$ (see Figure 4.7):
The current I_g from the ground through the sample holder into the TEM sample depends

on sample and contact resistances. In our experiment, the ground current is controlled by the MgO resistance. In situ TEM measurements by using a biasing sample holder with a piezo-controlled nanotip yield $R \approx 5 \cdot 10^9\ \Omega$ (see 4.6.7 in the Supporting Information) and consequently allows for I_g of the order of 100 pA at samples bias of 1 V. Defect states and surface contaminations reduce the initial resistivity of single crystalline bulk MgO from $\rho \approx 10^{15}\ \Omega$cm to $\rho \approx 2 \cdot 10^3\ \Omega$cm in defect-rich MgO-lamella cut by FIB. [192]

I_b denotes the backflow current from the gas environment either via capture of secondary electrons emitted from gas species or by negative gas ions which are formed by capture of electrons. An estimate shows that I_b is limited to sub-fA levels due to the small ionization cross sections of gas atoms and the small range of the electric field outside the TEM lamella (see Supporting Information 4.6.6). Cross sections for the formation of negative gas ions by SE capture are also very small. [193]
Backflow currents from the other environment I_{ev} involve secondary electrons originating from inelastic collisions of primary electrons with the MgO substrate[2], with TEM components and/or from back-scattered electrons from TEM elements. Such currents cannot easily be quantified, and their detailed discussion is beyond the scope of this paper. We assume their magnitude is small compared to I_g and comparable in the ETEM and in the holography experiment and disregard their influence in a comparative study of both experiments.

An extrapolation of the measured potential of $\langle V \rangle = 1.6$ V at 80 $e/(\text{Å}^2\text{s})$ to high fluxes via Eq. 4.7 would result in $V \approx 16$ V at 11 000 $e/(\text{Å}^2\text{s})$ based on an ohmic resistance. However, due to the strong potential dependence of $R(V)$ (Frenkel-Poole like behavior; see 4.6.7 in the Supporting Information), such an extrapolation overestimates the beam induced potential. Furthermore, the Chung-Everhart formalism most likely overestimates the high energy tail of $\mathrm{d}Y/\mathrm{d}E(E, \phi)$ and thus the SE emission currents. Taking these effects into account, the beam induced potential predicted from 4.7 for a primary flux of $10^3 - 10^4\ e/(\text{Å}^2\text{s})$ in the used gas environment is expected of the order of a few volts.

4.4.2 Behavior of the PCMO Electrocatalyst under ETEM Conditions

On the basis of our estimate of a beam induced positive potential of the order of a few volts, we assume that the conditions for anodic behavior of the electrocatalyst are present in our ETEM experiments. Dependent on the magnitude of the potential V, the water pressure, and the damage state of the catalyst, two different oxidation processes can be induced at the catalyst-water interface: (i) oxidation of defect-rich, oxygen-depleted areas of the PCMO electrocatalyst and (ii) oxidation of H_2O and oxygen evolution. Both processes may also coexist.

[2]Part of the MgO substrate might be illuminated because of a spread of the beam diameter in gas due to scattering of primary electrons with gas molecules.

Oxidation and Recrystallization of Damaged Amorphous PCMO Areas
The observation of an electron beam induced recrystallization process of initially amorphous PCMO in pure water vapor at electron flux $< 9000\ e/(\text{Å}^2\text{s})$ (Fig. 4.2b,c) is in the following interpreted as an electrochemical oxidation of oxygen-depleted amorphous specimen regions driven by a beam induced positive electrical potential. EELS of the O K-edge shows the reestablishment of the pre-edge feature (A) which was suppressed in the as-prepared state of the TEM sample (Fig. 4.3a). This is consistent with the presence of oxygen deficiency in the as-prepared state, where surface oxygen vacancy donor defects have been generated by the preparation process of the TEM lamella. Healing of such donor defects increases the hole concentration in the O $2p$ - Mn $3d$ valence band which is indicated by the increase of the O K-pre-edge feature (A) (see Fig. 4.3a). The tiny increase of the Mn $I(\text{L}_3)/I(\text{L}_2)$ intensity ratio is also consistent with the healing of electron donor defects such as oxygen vacancies (see Fig. 4.2c). However, the Mn L-edge seems to be less sensitive to changes in the oxygen content and in the Mn valence state crystalline PCMO in comparison to the O K-pre-edge. This is in agreement with investigations by Riedl et al. and Varela et al., who show that features representing the Mn valence state of manganites which involve the O K-edge (e.g., $|E(O\ K_A) - E(O\ K_B)|$ or the pre-peak (A) intensity) have a higher sensitivity to changes of the Mn valence state. [172, 194]

The absence of the recrystallization of amorphous PCMO as well as the related changes in the O K-edge and Mn L-edge in high-vacuum experiments indicates that the presence of H_2O or H_2O-derived intermediates is required for the healing of the damaged regions. Electrochemical oxidation/reduction by oxygen intercalation/deintercalation is observed in cyclic voltammetry for many transition metal oxides. The redox process can take place at room temperature at electrical potentials of the order of $V \approx 1$ V, [157, 158] where the oxidation of electrodes by oxygen intercalation requires an anodic polarization. The oxygen intercalation is topotactic in nature, if the reaction does not involve diffusive rearrangement of the host atoms. In perovskite-derived structures of transition metal oxides $ABO_{3-\delta}$, a reversible topotactic transformation between fully oxygenized and O-deficient structures is typically observed at electrochemical potentials V slightly below the potential $V(H_2O \rightarrow 1/2O_2 + H_2)$ for oxygen evolution. [186] There, the high mobility of the oxygen was attributed to the surface formation of O^- ions from H_2O or OH^- species. The penetration of O^- from the electrode surface into the bulk requires metal cations with variable valence state and where the charge transfer reaction $B^{(n+1)}+O^{2-} \leftrightarrow B^{n+}+O^-$ only requires a small charge transfer energy. In addition to the electrochemical transformation between crystalline structures of different oxygen stoichiometry, topotactic transformations may also involve amorphous phases. [195]

Our observation that the electron beam driven oxidation is limited to a H_2O pressure range of some μbar and changes into a beam induced amorphization/corrosion at higher H_2O pressure (Figure 4.1d) may be explained by an increased thickness of the H_2O adsorption layer which suppresses the SE emission. We have no proof for this assumption. However, it is consistent with reduced electrostatic charging at increasing pressures in environmental

electron microscopy. [196] A drop of the potential below the equilibrium potential for the oxygen intercalation would give rise to a reduction reaction of the electrode.

Electrocatalytic Oxygen Evolution Indicated by the SiO_2 Reaction

The growth of SiO_{2-y} at catalytically active surfaces in a $He/H_2O/SiH_4$ gas mixture at a partial pressure of $p_{H_2O} \sim 3$ μbar is also consistent with the presence of a positive potential above 1.5 V. According to previous results, [185] SiO_{2-y} growth under such conditions indicates electrocatalytic oxygen evolution and cannot take place by a direct reaction of SiH_4 with H_2O. This statement is derived from the observation that the beam induced SiO_{2-y} growth requires the presence of a catalyst for oxygen evolution and does not take place at nonactive materials or at amorphous PCMO edges. The formed oxygen can react with the SiH_4 molecules according to $SiH_4 + O_2 \rightarrow SiO_2 + H_2O/H_2$, with SiO_2 growing as a solid amorphous material on the catalyst surface.

The analysis of the Mn $I(L_3)/I(L_2)$ intensity ratio of EEL spectra yields a decrease of the Mn oxidation state in PCMO in SiO_{2-y} covered surfaces from 3.3 to 2.4. The Mn^{2+} formation at surfaces under oxygen evolution conditions is also observed by in situ XANES experiments. [28] This valence decrease is consistent with the generation of oxygen vacancies and related electron doping while the crystalline perovskite structure is largely maintained.

Apparently, the oxygen vacancy formation under oxygen evolution conditions is contrary to the observation of oxidation of amorphous areas in experiments with pure H_2O vapor. Indeed, oxygen intercalation is often observed by cyclic voltammetry as an oxidation reaction preceding the oxygen evolution reaction. We assume that surface and subsurface oxygen vacancies participate in the O_2 evolution process. Consequently, the full oxidation of the catalyst may be not achievable after the oxygen evolution has set in. Recently, it has been shown that the formation of oxygen vacancies in the active state of the PCMO catalyst is fully reversible and can be entirely healed out in the presence of gaseous oxygen at slightly elevated temperatures at zero bias. [28] However, in the ETEM in $He/H_2O/SiH_4$ gas mixture the oxygen evolving from water oxidation is captured in the reaction $SiH_4 + O_2 \rightarrow SiO_2 + H_2O/H_2$. This may lead to a deceleration of oxygen intercalation and a suppression of oxygen vacancy healing which results in a reduction of the PCMO surface and subsurface. The formation of oxygen vacancies in the active area of the studied PCMO lamella is supported in postmortem analysis, where the evolution of a 2 x 2 superstructure most likely due to oxygen vacancy ordering is observed (see 4.6.9 in the Supporting Information). The spatial extent of areas exhibiting SiO_{2-y} coverage and areas with 2 x 2 superstructure in postmortem studies nicely agrees (Fig. 4.13). The catalytic turnover number, i.e., the number of oxygen atoms in the SiO_{2-y} layer per oxygen vacancy in the PCMO crystal, is estimated to about 3.8 (see section 4.6.9 in the Supporting Information). A turnover number > 1 proves that catalytic oxygen evolution via water oxidation takes place and that the SiO_{2-y} layer is not exclusively formed by oxygen released during catalyst reduction.

The increasing area exhibiting SiO_{2-y} coverage at different electron flux between 2000 and 11 000 $e/(Å^2s)$ (Figure 4.5b,d) at constant beam diameter may give insight into the spatial extent and distribution of beam induced potentials. The spatial distribution of potentials where oxygen evolution takes place can exceed the beam diameter by a factor of 1-3 depending on the electron flux. Remarkably, the area of highest electron flux in the center of the electron irradiated area (Figure 4.5a,b) shows a significant reduction of the SiO_{2-y} growth compared to surrounding areas. The reduced SiO_{2-y} formation in the central beam area with the highest electron flux may either indicate that the local potential was too large or that beam damage may have reduced the reaction rate. We exclude that the spread of the SiO_{2-y} around illuminated areas is induced by beam spreading in the gas because the fraction of scattering events between primary electrons and gas atoms/molecules generally provoking a skirt-like beam spread [197] is very weak in the TEM due to the small scattering cross section for 300 keV electrons.

4.5 Conclusions

ETEM studies of a $Pr_{0.64}Ca_{0.36}MnO_3$ (PCMO) electrocatalyst in contact with water vapor reveal that two chemical reactions can be induced by the high-energy electron beam: (i) The oxidation of oxygen-depleted amorphous surface regions of the electrode which are formed during TEM sample preparation with FIB. The oxidation is visible by the increase of the O K-pre-edge feature and the formation of the Pbnm perovskite structure via recrystallization of the amorphous material. (ii) Oxygen evolution is detected via observation of the growth of SiO_{2-y} at catalytically active PCMO surfaces in a $He/H_2O/SiH_4$ gas mixture. We are aware that using SiO_{2-y} formation as an indicator for oxygen evolution is indirect. However, we base our conclusion on systematic ETEM studies which exclude a direct SiH_4 oxidation by water and show that an oxygen evolution catalyst is required. In accordance with a recent in situ XANES study, [28] which shows that reversible oxygen vacancy formation evolves at positive potentials under oxygen evolution conditions, we provide direct imaging of the oxygen vacancy enriched areas by 2 x 2 superstructure formation combined with EELS of the oxygen K-edge. Although some of the SiO_{2-y} may be formed with oxygen from the electrode material, we can exclude that SiO_{2-y} growth is the origin of the oxygen vacancy formation.

Furthermore, we conclude that whether PCMO surface and subsurface regions are oxidized or reduced in contact with water vapor may not only depend on the applied potential. It rather seems to be an intrinsic property of the catalyst with respect to the oxygen evolution activity. Formation of Mn^{2+} and filling of the anti-bonding Mn-e_g bands with more than one electron per unit formula would result in a reduced oxygen evolution activity as pointed out in Ref. [2].

On the basis of the quantification of electron beam induced sample potentials by electron flux dependent measurement of phase shifts in off-axis holography, we present strong evidence that the observed chemical reactions are of electrochemical nature; i.e., they are

driven by a beam induced positive electrode potential of the order of 1-2 V. Electrostatic modeling provides insights into the balance of currents and thus into the conditions which are required for the buildup of potentials. The results show that potentials of the order of 1 V can be easily built up in samples that are electrically insulated from the ground and in gas environments, where the ion and electron densities are orders of magnitude below the generated charge density within the TEM sample. We are confident that the provided insights into the beam induced electric potential effects in ETEM will stimulate further experimental and theoretical work on measurement and control of electrode potentials and open up a pathway for controlled electrochemical experiments under electron beam illumination.

Acknowledgments We thank the DFG for financial support within the SFB 1073, project C02.

4.6 Supporting Information

4.6.1 Experimental Methods and Basic Sample Characterization

Figure 4.8a illustrates the structured cross-section TEM lamella showing a MgO-PCMO-Al_2O_3 stacking sequence. The finally deposited gold film is completely removed during the FIB procedure. A post-milling procedure using a Gatan precision ion polishing system (PIPS) with Ar ion energies 0.5.1.5 keV under incident angles $< 10°$ removes most of the re-deposited or beam-damaged material. This preparation method of TEM samples produces thin crystalline edges, where the damaged amorphous PCMO at edges along the focused ion beam direction is only 1-2 unit cells wide (see Fig. 4.8b). Electron diffraction imaging of the TEM sample (Fig. 4.8c) confirms epitaxial growth and the existence of [110]/[001] twin domains. The orthorhombic unit cell of PCMO (room temperature space group Pbnm) exhibits a doubling of the pseudocubic c-axis resulting in a half periodicity in the reciprocal lattice in comparison to the cubic $Pm\bar{3}m$ perovskite structure. The half periodicity is visible by the appearance of the [101] spots, since the [001] peak is extinct due to extinction rules.

TEM experiments including electron diffraction, imaging and electron energy loss spectroscopy (EELS) were performed with 300 keV electrons in an aberration corrected FEI Titan electron microscope with an environmental cell (ETEM). With an information limit of about 0.08 nm in high-vacuum this microscope allows for high-quality lattice imaging and study of atomic scale processes. The Scanning TEM (STEM) capability combined with EELS gives access to the local chemical composition and the electronic structure with a spatial resolution of $\sim$ 0.2 nm and an energy resolution of $\sim$ 1.3 eV.

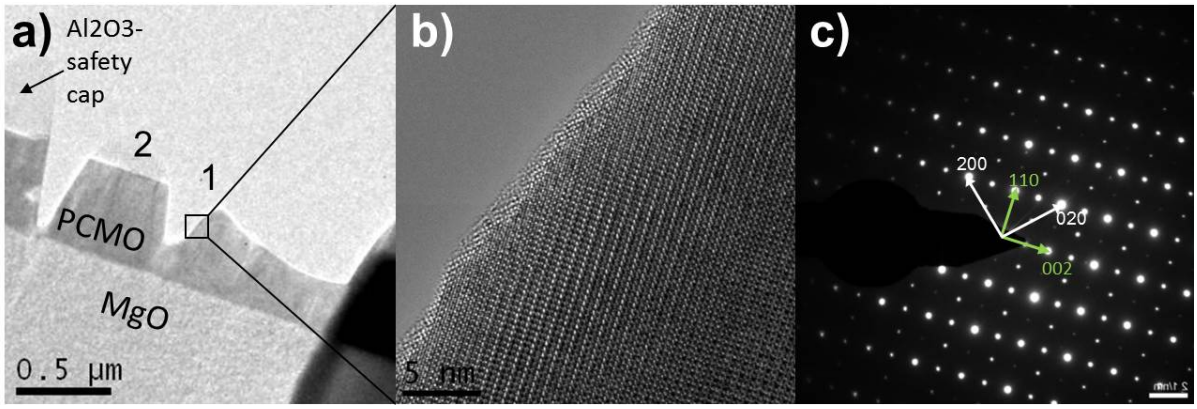

FIG. 4.8 PCMO/MgO TEM lamella which was used for electro-catalytic studies of oxygen evolution. a) Overview bright field image showing sample geometry of the PCMO film on MgO [001] substrate covered with an amorphous Al_2O_3 protection layer. The notches carefully cut by FIB allow for the formation of vertical crystalline edges. (b) High resolution TEM image of a selected vertical edge showing crystalline structure with minimum ion beam damage on a scale of 2 nm. (c) Diffraction pattern of the PCMO film. The diffraction spots can be indexed with [110] /[002] (green arrows) and [200]/[020] (white arrows), i.e. the diffraction pattern shows [-110] (green) as well [001] (white) zone axis due to presence of twin domains with the Pbnm c-axis either parallel to the beam direction (white) or perpendicular rotated by 90° around the crystalline [110] direction (green).

For studying the behavior of the PCMO crystal in contact with water vapor, we carried out two types of experiments: i) PCMO in pure water vapor, where evaporating distilled water was injected into the sample chamber of the ETEM yielding pressure ranges from $1-150$ μbar, and ii) PCMO exposed to gas mixtures containing H_2O, He and monosilane SiH_4 with the total gas pressure $p = 0.3$ mbar and the H_2O partial pressure $p_{H_2O} = 3$ μbar. As was shown in Ref. [185] SiH_4 can be used as an indicator agent for visualization of active catalyst areas for oxygen evolution. After gas inlet the sample was equilibrated for about 20-30 min in gas before electron exposure started. The processes of the specimen in contact with water vapor were studied via TEM imaging in gas with electron fluxes of $2000-11000$ $(e/\text{Å}^2\text{s})$.

4.6.2 Chemical Analysis of the Initial and Reacted State by means of EELS - Determination of Mn Oxidation States

EELS analysis of the initial state of the specimen and after gas exposure were performed in high vacuum and in water vapor. All different states were compared in order to analyze the chemical and electronic modifications of the specimen in gas atmosphere. The analyzed regions have a ratio of lamella thicknesses d to the electron inelastic mean free path λ at 300 keV of $d/\lambda < 0.7$. Due to spectrometer drift, a calibration of the energy axis of the spectrometer to the Mn L_3 energy at 646 eV is performed. The Ca L-spectra are normalized to the L_2-peak intensity. The spectra of the O K-edge and the Mn L-edge are normalized to the intensity of the respective continuum excitation in a 5 eV window above the characteristic features. The Mn L_3-feature originates from electronic excitations from $2p_{\frac{3}{2}}$ to $3d_{\frac{5}{2}}$ and $3d_{\frac{3}{2}}$ spin-orbit split states while the L_2

feature is a result of transitions between $3p_{\frac{1}{2}}$ and $3d_{\frac{3}{2}}$ states. For instance, a decrease of the Mn valence state implies an increasing occupation of $3d_{\frac{3}{2}}$ states and the intensity of excitation channels with $3d_{\frac{3}{2}}$ final state decreases. This results in an increased $I(\mathrm{L_3})/I(\mathrm{L_2})$-intensity ratio which is commonly used as a measure for the Mn valence state.

The determination of the Mn oxidation state is carried out in order to analyze the change in oxygen and cation stoichiometry, defect concentration and resulting carrier density in the conduction band. For the determination of the Mn valence by EELS we use here the method of analyzing the intensity ratio of the Mn $\mathrm{L_3}$ and the $\mathrm{L_2}$ lines ($\mathrm{L_{23}}$ ratio). [171–173, 194, 198, 199] A qualitative analysis of the O K-pre-peak intensity is used to verify the results obtained with the Mn $I(\mathrm{L_3})/I(\mathrm{L_2})$-ratio analysis. [172, 200]. For a reliable extraction of the Mn $I(\mathrm{L_3})/I(\mathrm{L_2})$-ratio, careful background subtraction using a Hartree-Slater continuum background was carried out and the line intensities were determined via integrating characteristic ranges of the dataset. A comparison of our results of the Mn L-edge analysis with results on Ca-doped $\mathrm{LaMnO_3}$ obtained in [172, 194] allows the determination of the Mn oxidation state.

The energy loss near edge structure (ELNES) of the Ca L-edge of the initial state and the reacted state after exposure to 5 μbar and 150 μbar water vapor is illustrated in Fig. 4.9a. Typically, it is split into the $\mathrm{L_3}$ and $\mathrm{L_2}$-edge at 346 eV and 350 eV due to spin-orbit coupling of the Ca $2p$ states (Fig. 4.9a). Low pressure water vapor exposure (5 μbar) does not induce any appreciable changes to the Ca L-edge. However, at 150 μbar water vapor, the $\mathrm{L_3}$ intensity decreases drastically which indicates a change in the bond coordination. [201,202] Changes in the ligand field can have a strong effect on the position and intensities of the $\mathrm{L_3}$ and $\mathrm{L_2}$ lines. [203] The observed strong changes in the Ca L-edge during beam induced amorphization thus reflect the decomposition of the perovskite structure into a disordered material. However, the broad peak centered near 340 eV which evolves in high water pressure may originate from carbonate formation. [204]

4.6.3 Oxidation State of Manganese during Electron Exposure in $\mathrm{He/H_2O/SiH_4}$

Figures 4.9b and 4.9c show the ELNES of the O K-edge and the Mn L-edge before and after exposure to the gas mixture $\mathrm{He/H_2O/SiH_4}$. It reveals a drastic decrease of the Mn oxidation state from initially 3.4 to 2.4 after 3 minutes under electron irradiation in gas. The post-gas disappearance of the O K-pre-edge is a further strong indicator for a significant filling of the majority e_g-states. The entire disappearance even suggests that the majority e_g-states are completely filled which corresponds to a Mn oxidation state of 2. However, the superposition of oxygen signals originating from PCMO as well as $\mathrm{SiO_{2-}}_y$ makes a quantitative analysis of the O K-edge impossible.

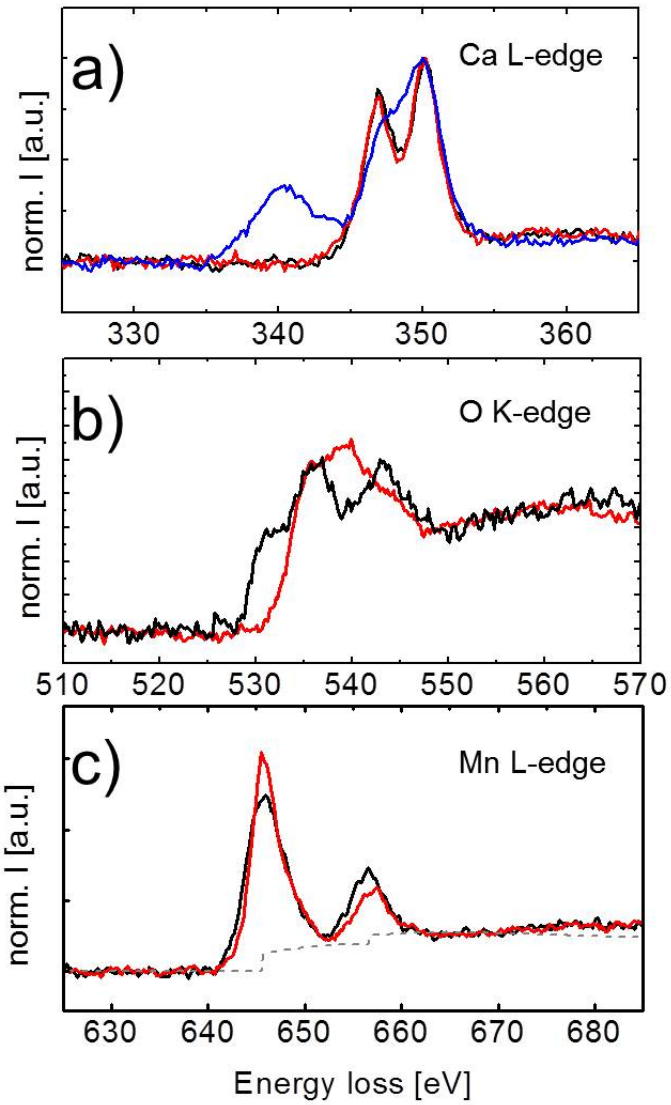

FIG. 4.9 ELNES of the a) Ca L-edge before (black line) and after exposure to pure water vapor with a pressure $p_{H_2O} = 5$ μbar (red line) and $p_{H_2O} = 150$ μbar (blue line). b) and c) ELNES of the O K-edge and the Mn L-edge before (black line) and after exposure to $He/H_2O/SiH_4$ gas mixture at $p = 0.3$ mbar (red line) . The gray dashed line in c) corresponds to the Hartree-Slater background which is subtracted from the Mn white lines before quantification of the $I(L_3)/I(L_2)$-intensity ratio.

4.6.4 Off-Axis Electron Holography (Experimental Parameters)

The phase shifts of the electron wave traversing the sample or near sample areas are measured by acquiring an interference pattern with a reference wave propagating far enough from the sample area in the vacuum. The position and contrast of the fringes in the gained interference pattern, the hologram, depend on the phase and the amplitude of the electron wave interacting with the specimen potential. The interference pattern is

generated by placing a biased conductive wire (the biprism) at an appropriate location along the beam path, which acts as a beam splitter: half of the electron beam undergoes a phase shift due to interaction with the electric or magnetic fields of the specimen and the other half, ideally unperturbed, is the reference. In order to avoid phase shifts induced by a magnetic potential at the specimen area, the objective lens is switched off. Instead, a Lorentz lens is used which almost eliminates magnetic fields in the specimen region. Since our sample is paramagnetic, a possible magnetic potential from sample magnetization is absent too. Numerical image processing including Fourier transformations and filtering procedures of the hologram yields the phase as well as the amplitude image (see [205] for details).

We use a C_S-corrected FEI Titan Analytical 80-300ST equipped with a field emission gun (FEG), rotatable biprism and Lorentz lens operated at 300 kV. The FEG generates highly coherent electron waves, which are necessary to achieve high-quality holograms. The holograms with 2.8 nm fringe spacing are recorded with a Gatan model 894 2k UltraScan 1000 camera and the reconstruction of the phase and amplitude is obtained using standard FFT-algorithm. [205] Measurements are performed in high vacuum at varying electron flux ranging from 0.8 to 80 $e/\text{Å}^2 s$.

4.6.5 Estimate of Secondary Electron (SE) Yields in PCMO

High energy electrons traversing a target material undergo diverse elastic and inelastic scattering events. The probability of a certain scattering event basically depends on the thickness and density of the target material as well as its electronic and atomic structure. Generally the scattering rate $\mathrm{d}n_s/\mathrm{d}t$, i.e. the number of scattering events per unit time and unit target volume of electrons of energy E_i traversing a target is described by

$$\frac{\mathrm{d}n_S}{\mathrm{d}t} = n_T \cdot \sigma_{T\leftrightarrow e}(E_i) \cdot F_i \tag{4.8}$$

F_i is the primary electron flux, $F_i = \frac{1}{A} \cdot \frac{\mathrm{d}N_i}{\mathrm{d}t}$, the number of primary electrons N_i per unit time and electron irradiated target area A. n_T is the particle density of the target material and $\sigma_{T\leftrightarrow e}(E_i)$ is the target material specific scattering cross section of the considered scattering event for electrons of energy E_i .

In the following calculations, we treat F_i as constant in the whole irradiated target volume which is an adequate assumption if the yield, i.e. the number of scattered electrons per primary electron and unit time is small.
In order to determine the charge induced into the PCMO specimen by secondary electron emission, we need to know about the charge generation and charge compensation rates, or rather the SE emission and neutralization currents. Here, we estimate the SE yield Y, i.e. the number of SE current per incident electron current, by modifying Eq. 4.8. The flux can be expressed as a particle current per unit volume $A \cdot \mathrm{d}x$, $\frac{\mathrm{d}n_i}{\mathrm{d}t}$, multiplied with

the thickness of a target element $\mathrm{d}x$, $F_i = \frac{1}{A} \cdot \frac{\mathrm{d}N_i}{\mathrm{d}t} = \frac{\mathrm{d}n_i}{\mathrm{d}t} \cdot \mathrm{d}x$.

$$\frac{\mathrm{d}n_{SE}}{\mathrm{d}t} = n_{PCMO} \cdot \sigma_{ion}(E_i) \cdot F_i = n_{PCMO} \cdot \sigma_{ion}(E_i) \cdot \frac{\mathrm{d}n_i}{\mathrm{d}t} \cdot \mathrm{d}x \tag{4.9}$$

$\mathrm{d}x$ can be translated into a characteristic depth where generated SE depending on their energy can escape the sample, i.e. the escape probability of generated SE with energy E. Most of the generated SE have kinetic energies $E_{SE} < 5$ eV (for most materials) [191] and thus a rather short mean free path in the PCMO specimen. We can describe the inelastic mean free path λ of the SE in PCMO with the semi-empirical formula

$$\frac{\lambda(E)}{a} = 2170\,(E - E_F)^{-2} + 0.72\,(a\,(E - E_F))^{\frac{1}{2}} \tag{4.10}$$

given by Seah and Dench [206] for inorganic compounds where a is the monolayer thickness ($a = 0.385$ nm), E_F is the Fermi energy ($E_F = 1.84$ eV) and E is the energy of SE relative to the bottom of the conduction band. The SE-yield, i.e the number of generated SE per incident electron current and unit time, can be calculated according to an equation given by Chung and Everhart. [189] Considering a thin TEM specimen of thickness d we get

$$\frac{\mathrm{d}Y}{\mathrm{d}E(E,\phi)} = \frac{2 \cdot S(E)\lambda(E)}{4} \cdot F(E,\phi) \cdot \left[1 - \exp\left(-\frac{d}{\lambda(E)}\right)\right] \tag{4.11}$$

$S(E)$ describes the number of electrons per incident electron and unit energy excited into an energy interval between E and $E + \mathrm{d}E$. $F(E,\phi)$ depends on the work function ϕ and considers the propagation of SE excited to energies above vacuum level, i.e. $E > E_F + \phi$, to the surface. The term $\lambda(E) \cdot F(E,\phi) \cdot \left[1 - \exp\left(-\frac{d}{\lambda(E)}\right)\right]$ considers the limitation of the emission of SE electrons due to the finite thickness of the TEM specimen, i.e. when their mean free path $\lambda(E) < d$. In this limit, the presence of two surfaces is taken into account by a factor of 2 in Eq. 4.11. It results from the emission of SE from the top as well as from the bottom surface of the thin TEM foil assuming that the incident flux at the top and the bottom surface is the same.

$$S(E) = \frac{C_Y(E_i)}{(E - E_F)^2} \qquad \text{and} \qquad F(E,\phi) = 1 - \frac{E_F + \phi}{E} \tag{4.12}$$

The normalization constant $C_Y(E_i)$ depends on material properties and the incident electron energy E_i. It can be determined by comparing the total number of electrons excited to energies $E > E_F + \phi$, i.e. ionizing scattering events per incident electron with the ionization cross section of PCMO:

$$n_{PCMO} \cdot \sigma_{ion}(E_i) = \int_{E_F+\phi}^{\infty} S(E)\mathrm{d}E = \frac{C_Y(E_i)}{\phi} \tag{4.13}$$

The ionization cross section basically depends on the incident energy. We estimate the cross section $\sigma_{ion}(E_i)$ from atomic ionization cross sections for $\mathrm{Mn}^{3+} + e \rightarrow \mathrm{Mn}^{4+} + 2e$

($\sigma_{\mathrm{Mn3}\to\mathrm{Mn4}}(E_i) \approx 2\cdot10^{-19}$ cm^2) and $\mathrm{Ca}^{2+} + e \to \mathrm{Ca}^{3+} + 2e$ ($\sigma_{\mathrm{Ca2}\to\mathrm{Ca3}}(E_i) \approx 2\cdot10^{-19}$ cm^2) for 300 keV incident electrons. We get these cross sections from the database http://dbshino.nifs.ac.jp/. The cross section for $\mathrm{O} + e \to \mathrm{O}^{1+} + 2e$ is of the same order of magnitude. Unfortunately, there is no data available for Pr. We assume that cross sections describing $\mathrm{Pr}^{3+} + e \to \mathrm{Pr}^{4+} + 2e$ are in the same order of magnitude. Thus we get an average ionization cross section of $\sigma_{ion}(E_i) \approx 2\cdot10^{-19}$ cm^2 from the stoichiometric sum $\sum_i \frac{n_i}{n}\cdot\sigma^i_{ion}$. The particle density in PCMO is $n_{PCMO} = 8.76\cdot10^{22}$ cm^{-3}.

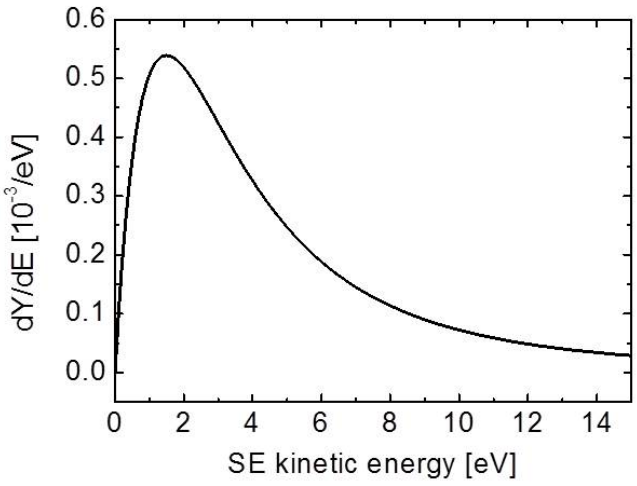

FIG. 4.10 Energy distribution of the SE-yield according to Eq. 4.11.

Integrating $\frac{\mathrm{d}Y}{\mathrm{d}E}$ over all SE energies $E > E_F + \phi$, with $E_F = 1.84$ eV and $\phi = 4.9$ eV [165] gives the total yield

$$Y_0 = \int_{E_F+\phi}^{\infty} \frac{\mathrm{d}Y}{\mathrm{d}E}\mathrm{d}E = 0.0034 \tag{4.14}$$

The energy distribution $\frac{\mathrm{d}Y}{\mathrm{d}E}$ of the emitted SE from PCMO is presented in Fig. 4.10. It exhibits a maximum at $E_{SE} = 1.49$ eV. Note, E_{SE} is the kinetic energy of escaping SE with respect to vacuum level, i.e. $E_{SE} = E - E_F - \phi$.

4.6.6 Estimation of the Neutralization Current from the Gas Environment

In presence of gas (here 99% helium and 1% water) incident electrons undergo inelastic scattering events with gas atoms or molecules resulting in a fractional ionization of the gas particles. Such ionization processes are accompanied by the emission of SE from gas atoms/molecules, so-called environmental secondary electrons (ESE). All ESE generated near the PCMO surface are attracted by the beam induced electric potential in PCMO and thus contribute to charge compensation. Furthermore, SE emitted from PCMO

might be captured by water molecules due to dissociative electron attachment. This results in the generation of negatively charged OH^-, O^- or H^- ions which represent an additional contribution to charge neutralization. [207] The possible charge neutralization channels from gas, i.e. ESE capture and charge transfer from negative ions, are schematically shown in Fig. 4.11. Due to the decay of the electric field outside the PCMO specimen the neutralization currents of ESE and negative ions are generated within a finite interaction volume with radius s_i. It depends on the sample geometry, sample potential, kinetic energies and mean free paths of the respective particles. Kinetic energies of ESE and negative ions are small (<5eV). In the following we assume that ESE and negative ions generated at $s > s_i$ do not contribute to charge compensation whereas all ESE and $\{H_2O\}^-$ ions generated at $s < s_i$ are captured by PCMO.

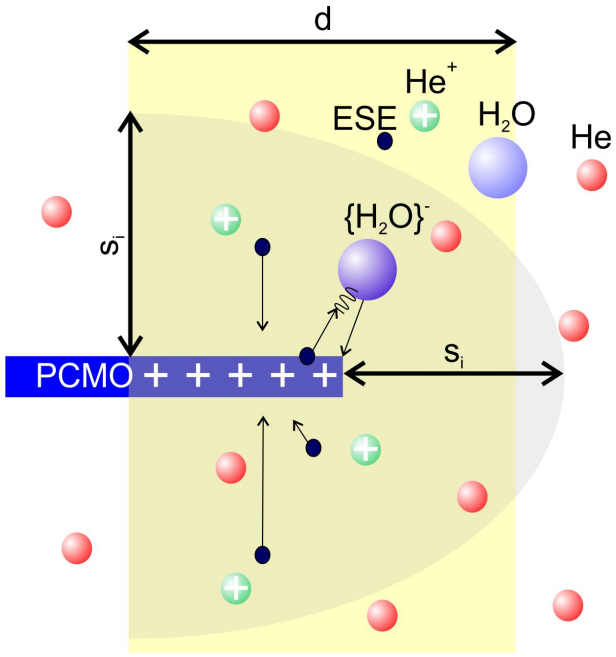

FIG. 4.11 Scheme of the contribution of gas environment to neutralization currents. Inelastic collision of beam electron with gas molecules leads to ESE emission and generation of positive gas ions (here helium). ESE as well as negative gas ions due to dissociative electron attachment to water can diffuse to the sample for distances $s < s_i$ (gray shaded area), where s_i denotes the range of the electric field in the vacuum. The yellow area represents the beam diameter d.

We get a rough estimate of the ESE-yield for He gas pressure $p = 0.3$ mbar and a typical ionization cross section $\sigma_{ion}(E_i) \sim 10^{-19}$ cm^2 via

$$Y_{He}^{ESE} = n_{gas} \cdot \sigma_{ion}(E_i) \cdot 2s_i \approx 5 \cdot 10^{-8} - 10^{-6} \tag{4.15}$$

for s_i in a range of 500 nm - 10 μm. Y_{He}^{ESE} is only $10^{-3} - 5 \cdot 10^{-5}$ of the SE-yield Y_0 of PCMO. For a beam current of $I_p = 11$ nA the resulting backflow current in the order of $I_b = 10$ fA. Even for much larger s_i, I_b is much below the SE emission currents. Thus, the backflow from gas limited by the number of ESE is much too small to be taken into

account for neutralization.

Cross sections for dissociative electron attachment are even smaller than for ionization. Considering for example H_2O, $\sigma_{diss} < 10^{-21}$ cm^2 for ESE energies < 5 eV is more than 2 orders of magnitude smaller than $\sigma_{ion}(E_i) \approx 10^{-19}$ cm^2 . Moreover, the water partial pressure is a factor 10^2 smaller than the He partial pressure. Thus, we can easily disregard all charge neutralization channels involving H_2O and He. [193]

The negligible impact of the gas environment on neutralization of sample charging in the ETEM seems to be in contradiction to environmental SEM (ESEM), where gas is used for charge neutralization of insulating samples. In contrast to ETEM, an external potential between the sample (which is negatively charged due to the absorption of beam electrons) and the electron detector is applied in ESEM. The applied potential gives rise to an acceleration of ESE and, thus, a drastic interaction volume between ESE, gas ions and sample. Furthermore, in environmental SEM the emitted SE's are accelerated to the detector which is at positive bias. Thus, they gain kinetic energy leading to multiple inelastic scattering events of one single SE with gas species and resulting cascade generation of positively charged gas ions. This cascade effect is absent in TEM. [208]

4.6.7 Neutralization Current from the MgO Back Contact

In order to estimate the contribution to the neutralization current coming from the nominally insulating MgO section of the TEM lamella clued to the Cu grid by an electron beam deposited Pt/C mixture, we have measured current-voltage characteristics using a Nanofactory TEM holder equipped with a piezo-driven Pt/Ir tip for biasing. The dimensions of the MgO lamella and the PCMO/MgO lamella shown in Fig. 4.8 are comparable, i.e. both have a thickness of 50 nm and a height of about 3 μm. The height is defined as the distance from the Cu grid back contact to the surface which can be contacted by the Pt/Ir tip. In the experiment shown in Fig. 4.12, we obtain a total resistance of $R = 10^9\ \Omega$ for $\|U\| \leq 1$ V. Using the STM holder for resistance measurements at metallic TEM samples, the contribution of interface and feed line resistances can be estimated to be in the range of $15 - 20\ \Omega$. Even contact resistance between the Pt/Ir tip and highly conducting oxides such as Nb:STO is below 100 Ω. Consequently, we estimate a resistivity of about $\rho \approx 2 \cdot 10^3\ \Omega$cm for the MgO TEM lamella which is 12 orders of magnitude smaller than ideal single crystal values of $\rho \approx 10^{15}\ \Omega$cm. [192] Due to the non-linear current-voltage characteristics, the resistivity further decreases with increasing voltage.
It is well known that FIB preparation of TEM lamellae induces defects in the MgO, such as Ga implantation and oxygen vacancies due to atomic displacements. Oxygen vacancies can act as donors and generate electronic states within the band gap. [209] The same may apply for implanted Ga. In addition, surface contamination by C can enhance the electric conductivity.

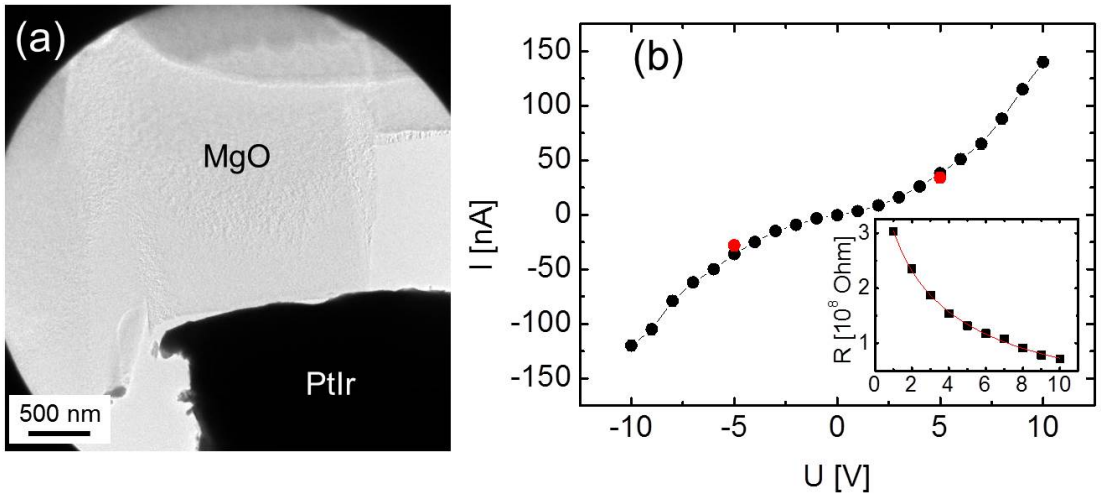

FIG. 4.12 Measurement of the electric characteristics of a MgO TEM lamella prepared by FIB. (a) Measurement configuration showing the electron transparent MgO, the Pt/Ir tip in contact with the lamella and the TEM aperture used for defining the illumination area. (b) Current-voltage curve with blanked beam (black circles), and under illumination (red circles) with a total beam current of $I = 10$ nA. Inset: Frenkel-Poole fit to the potential dependence of the resistance.

Considering a semi-circular PCMO region of radius $\hat{R} = 200$ nm illuminated by a beam current of $I_p = 11$ nA, and assuming a beam induced potential of 2 V where the potential dependent yield is $Y(V) = 0.0015$, the balance-of-currents equation 4.7 in the main manuscript indicates that a neutralization current of $I_n(V) = 17$ pA is sufficient to reach a stationary state. Using the measured resistivity for MgO would allow for neutralization currents of the order of $I_n(2V) \approx 100$ pA in this geometry, which is more than enough to insure a steady state.

4.6.8 Phase Shift Calculation

The electrostatic potential resulting from a fixed and known charge distribution $\rho(r)$ is

$$V(r) = \frac{1}{4\pi\varepsilon_0} \int \frac{\rho(r')}{|r - r'|} \mathrm{d}r' \tag{4.16}$$

According to Eq. 4.1 in the main text, the corresponding phase shift is

$$\varphi(x, y) = \frac{C_E}{4\pi\varepsilon_0} \int_{-\infty}^{+\infty} \mathrm{d}z \int \frac{\rho(r')}{|r - r'|} \mathrm{d}r' \tag{4.17}$$

As sketched in Fig. 4.6b, we choose $\rho(r') = \rho_0 \,\mathrm{Sign}(y)$, $r' < \hat{R}$, $|z| < d/2$, where $\hat{R}$ is the semi cylinder radius, d its thickness, $\rho_0 = 2Q/(\pi\hat{R}^2 t)$, Q is the total amount of charge present within the PCMO region (also equal to the total amount of image charge present throughout the MgO support). By considering the expansion of $1/|r - r'|$ in cylindrical

harmonics, [210] we have after integrating along z and z':

$$\varphi(x,y) = \frac{\rho_0 \cdot C_E \cdot d}{2\pi\varepsilon_0} \sum_{m=-\infty}^{+\infty} \int_0^{\hat{R}} r' \mathrm{d}r' \int_0^{+\infty} \frac{\mathrm{d}k}{k} J_m(kr') J_m(kr) \left[\int_0^{\pi} \mathrm{d}\theta' - \int_{\pi}^{2\pi} \mathrm{d}\theta' \right] \mathrm{e}^{\mathrm{i}m(\theta-\theta')} \tag{4.18}$$

where $J_m(x)$ is a Bessel function of the first kind. The angular integration along θ' removes even m's for symmetry, so that

$$\varphi(x,y) = \frac{4\rho_0 \cdot C_E \cdot d}{\pi\varepsilon_0} \sum_{m=0}^{+\infty} \frac{\sin\left[(2m+1)\theta\right]}{(2m+1)} \int_0^{\hat{R}} r' \mathrm{d}r' \int_0^{+\infty} \frac{\mathrm{d}k}{k} J_{2m+1}(kr') J_{2m+1}(kr) \tag{4.19}$$

In the exterior region $r > \hat{R} > r'$ the integral over the pair of Bessel functions yields a term proportional to $(r'/r)^{2m+1}$, which can be integrated along r' to give the end result

$$\varphi(x,y) = N\varphi_0 \frac{y}{r} \frac{16}{\pi} \sum_{m=0}^{+\infty} \frac{U_{2m}\left(\frac{x}{r}\right)}{(2m+1)^2(2m+3)} \left(\frac{\hat{R}}{r}\right)^{2m+1} \tag{4.20}$$

where we have introduced the Chebyshev polynomial of the second kind $U_{2m}(\cos\theta) = \sin\left[(2m+1)\,\theta\right] / \sin\theta$ to maintain a compact notation back in Cartesian coordinates, defined $\varphi_0 = eC_E/(4\pi\varepsilon_0)$ the single electron phase shift constant, equal to about 9.4 mrad at 300 kV, and measured the total charge in number of electrons: $Q = Ne$.

To fit the experimental data, we place a second PCMO region centered at $x = 2\hat{R} + \xi$, (see Fig. 4.6b) measuring the gap ξ directly from the experimental data, and evaluate the external phase profile along the curves parametrized by $\left(\hat{R} + \frac{\xi}{2}, y\right)$, red-fit, and (x, y_0), green-fit, where $y_0 = 155$ nm is the distance from the MgO substrate at which the experimental green profile was measured. The two free parameters N and $\hat{R}$ are then best-fitted as shown in Fig. 4.6e-f, yielding $N = 195$ and $\hat{R} = 214$ nm. Estimating the measurement uncertainty is very difficult. First of all, the procedure is extremely geometry- and model-dependent, while in reality the PCMO regions do not resemble closely semi cylinders, and we are using a rigid volume charge distribution. Therefore, the pure statistical uncertainty on the measurements (which, thanks to the high SNR in the data is rather small: $<2\%$) may not be very significant. Furthermore, we have disregarded two potentially relevant effects: additional PCMO regions outside the field of view, which, if charged, would add a stray field correction to the measured charge density, and the perturbation of the reference wave. While these two effects tend to compensate (stray fields from nearby charged regions would result in a larger measured charge density, while the perturbation of the reference wave would effectively decrease it), overall our degree of confidence in the measured value is probably in the 20% range.

The best-fit values are then employed to estimate the resulting beam-induced potential of the PCMO region. To this purpose, we calculate the potential according to Eq. 4.8,

and then average it over the hemicylindrical volume. The necessary computational steps are very similar to those carried out for the phase shift, so we just report the final result:

$$\langle V \rangle = V_S \sum_{m=0}^{+\infty} \frac{C_m}{(2m+1)}^2 \tag{4.21}$$

where $V_S = Ne/(4\pi\varepsilon_0\hat{R})$ is the potential that would be established if all the measured charge were distributed over a spherical surface of radius $\hat{R}$, and the coefficients of the capacitance series are given by

$$C_m = \frac{64}{\pi^2} \int_0^1 x \, \mathrm{d}x \int_0^1 x' \, \mathrm{d}x' \int_0^{+\infty} J_{2m+1}(qx) J_{2m+1}(qx') \, \mathrm{d}q \tag{4.22}$$

The capacitance series evaluates numerically without major difficulties to about 1.23, so that $\langle V \rangle = 1.23 V_S = 1.6$ V when $N = 195$ electrons and $\hat{R} = 214$ nm.
Note that, as it generally happens when estimating effective capacitances associated to rigid charge distributions that are not relaxed in such a way to produce equipotential surfaces, our result for $\langle V \rangle$ is most likely an overestimate of the real surface potential. For example, the self-capacitance of a spherical conductor is $4\pi\varepsilon_0\hat{R}$, so that $V_S = Q/(4\pi\varepsilon_0\hat{R})$, while the effective capacitance of a uniform charge distribution over a spherical region of radius $\hat{R}$, estimated by averaging the resulting electrostatic potential throughout the spherical volume, is $5/6(4\pi\varepsilon_0\hat{R})$, so that $\langle V \rangle = 6/5 V_S$. Therefore, the same amount of charge Q that results in V_S when distributed properly (i.e. uniformly over a spherical surface, in case of a spherical conductor), results in $1.2 V_S$ volume-averaged, if distributed uniformly over the volume. Furthermore, in calculating the averaged potential we have assumed that the thickness of the PCMO was much smaller than its radius, corresponding to neglecting the influence of the lateral surface, lowering further the effective capacitance.

4.6.9 Oxygen Vacancy Formation and Distribution

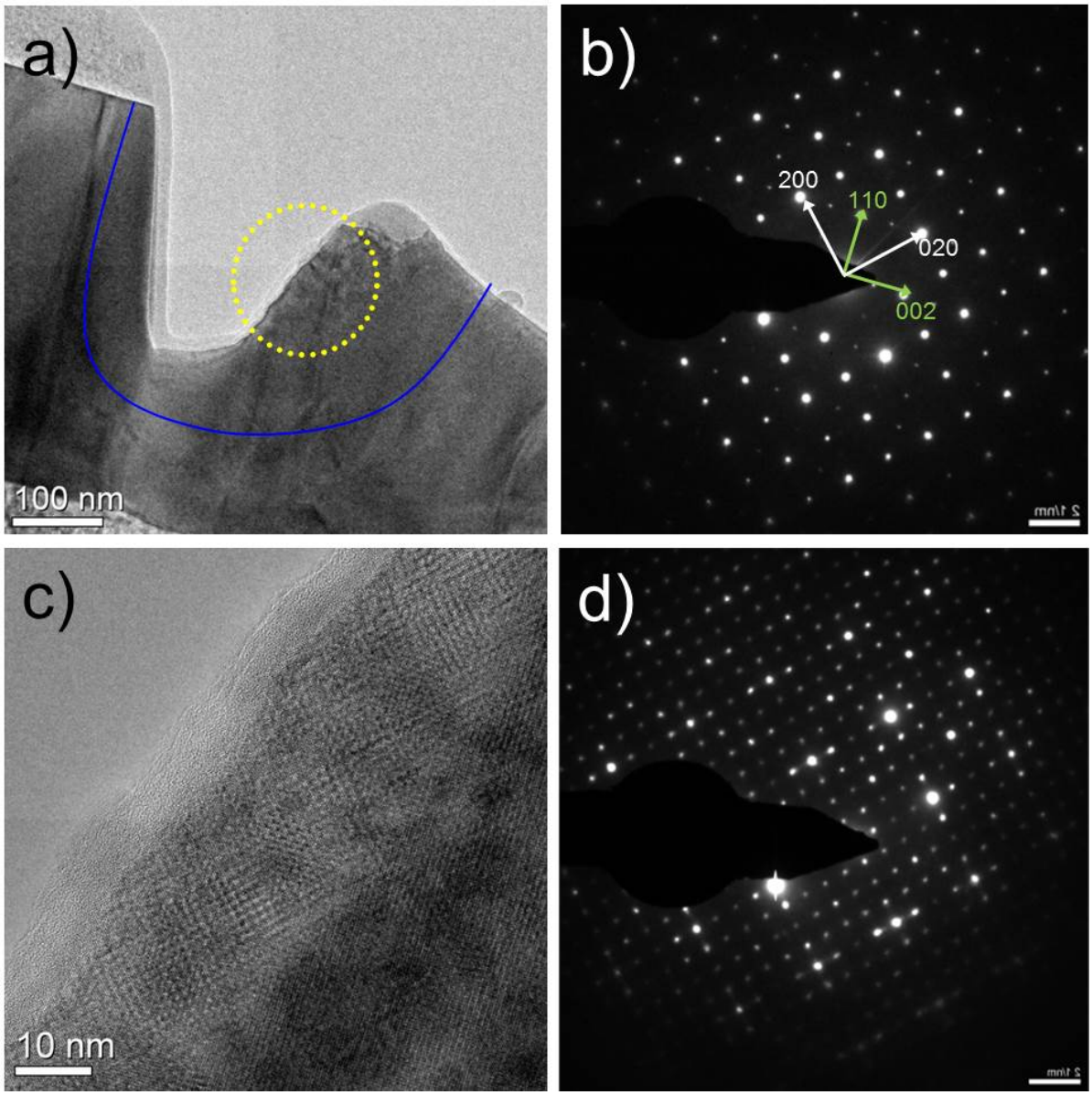

FIG. 4.13 Post mortem analysis of the induced changes in the PCMO film after the ETEM experiment in the 0.3 mbar $H_2O/He/SiH_4$ gas mixture. (a) TEM bright field overview image. The yellow circle marks the position of the electron beam with a flux of 11000 $e/Å^2 s$.The diffraction pattern in (b) is recorded immediately after return to HV mode and shows the initial Pbnm structure with characteristic twinning , i.e [001] (white arrows) as well as [-110] (green arrows) zone axis (c.f. Fig. 4.8 and associated figure caption) with a slightly increased fraction of twins with [001] zone axis. (c-d) During the post mortem study, a 2x2 superstructure starts to develop under the stimulation of the electron beam on a time scale of several minutes. (c) HRTEM image of the evolved superstructure. (d) The corresponding diffraction pattern of the area shown in c) reveals a real space doubling of the Pbnm *a*- and the *b*-axis. The blue line in a) marks the region with developed superstructure.

Figure 4.13 summarizes the formation of a 2x2 superstructure in a PCMO lamella after exposure to H_2O/He/SiH_4 and the electron beam. All images were obtained in high vacuum mode after turning off the gas supply. In Fig. 4.13 the yellow circle marks the position and size of the electron beam during the presence of H_2O/He/SiH_4 gas. While the PCMO crystal structure remains intact at edge regions parallel to ion beam used in FIB preparation, amorphization is observed at edges perpendicular to the ion beam (brighter top region above the yellow circle in Fig. 4.13a). Such edges suffer under strongly enhanced radiation damage during FIB preparation which may result in an increased instability against electrochemical corrosion during gas and electron exposure. Those edges are not further considered in the analysis.

Diffraction patterns obtained from the electron and gas exposed region (Fig. 4.13b) do not reveal any significant changes compared to the initial state, if studied immediately after re-establishing high vacuum conditions (Fig. 4.13b). The formation of a 2x2 superstructure is only observed a few minutes after starting the post ETEM characterization at a flux of $5000 - 25000\ e/\text{Å}^2 s$ (see Fig. 4.13 and d). The superstructure domains grow under the impact of the high energy electron beam. This phenomenon occurs only within regions that have been close to the electron beam irradiated area during the ETEM gas experiment. The blue line in Fig. 4.13a depicts the borderline of the evolving superstructure domain determined by HRTEM imaging. The image illustrates the final state after the growth of the superstructure domain has saturated under further continuous electron beam irradiation. For verification purposes, a crystalline region of PCMO far away from the reacted regions was exposed to the electron beam for 10 min with the same electron flux. It did not reveal any superstructure formation and showed the same stability like virgin PCMO which has been proven to be stable against beam damage in HV even in STEM/EELS under elevated dose rates as observed in numerous TEM studies (see e.g. [60, 64]).

Since the superstructures associated with charge order are only formed in the crystallographic *b*-direction and are mainly observed at low temperatures, [64] we can attribute the 2x2 superstructure at room temperatures in regions with reduced Mn valence and reduced O K pre-edge intensity to oxygen vacancy ordering. Furthermore, the time scale of superstructure formation under electron bombardment is of several minutes, indicating that vacancy redistribution is required to form the superstructure.

Water Oxidation vs. Oxygen Vacancy Formation - Catalytic Turnover

The spatial coincidence of areas with increased oxygen vacancy concentrations (exhibiting 2x2 superstructure) and areas exhibiting SiO_{2-y} coverage raises the question, whether SiO_{2-y} was partially formed by the reduction of the electrode. In the following we give an estimate of the turnover number $R_O = N_O/N_{V_O}$, i.e. the number of oxygen atoms N_O in the SiO_{2-y} layer per generated oxygen vacancies N_{V_O} in the PCMO crystal. From the TEM images (Fig. 4.5a), EELS spectroscopy as well as the EDX measurements (Fig. 4.5) we estimate the ratio of the SiO_{2-y} layer thickness covering the PCMO crystal and

the PCMO thickness to $\frac{d_{Si}}{d_{PCMO}} \sim 0.65$. The decrease of the Mn oxidation state to 2.4 as proved by EELS yields an oxygen deficiency according to $Pr_{0.64}Ca_{0.36}MnO_{3-\delta}$ of $\delta = 0.48$. We can now estimate the number of oxygen vacancies in an arbitrary PCMO volume of exemplarily cylindrical shape $V_{PCMO} = \pi \cdot r^2 \cdot d_{PCMO}$ to $N_{V_O} = \delta \cdot \frac{V_{PCMO}}{a^3}$, where $a \sim 3.8$ Åis the pseudocubic lattice parameter of PCMO. We can further derive the number of oxygen atoms N_O in the SiO_{2-y}volume $V_{Si} = \pi \cdot r^2 \cdot d_{Si}$ covering the PCMO cylinder at both surfaces, $N_O = (2 - y) \cdot \frac{V_{Si}}{b^3}$ with SiO_{2-y} lattice parameter b 3.4 Å. Calculating the ratio assuming $y = 0$ yields $R_O = \frac{N_O}{N_{V_O}} = \frac{2 \cdot d_{Si} \cdot a^3}{\delta \cdot d_{PCMO} \cdot b^3} = 2 \cdot \frac{0.65}{0.48} \cdot \left(\frac{3.8}{3.4}\right)^3 \sim 3.8$, i.e. almost two generated SiO_2 units per oxygen vacancy in PCMO suggests that water oxidation is likely to proceed and provide oxygen for SiH_4 oxidation. Of course, oxygen deficiency in the SiO_{2-y} layer ($y > 0$) reduces R_O.

For conventionally prepared polycrystalline PCMO TEM lamellae, catalytic turnover numbers of about 10 for oxygen evolution have been found. [185] The turnover number for the PCMO thin film samples is reduced. We attribute this difference to sample damage such as preformed oxygen vacancies induced by FIB sample preparation. An increase of the oxygen vacancy concentration drastically increases the oxygen ion mobility in manganites. [211]

CHAPTER 5

General Discussion and Summary

In the present thesis $Pr_{1-x}Ca_xMnO_3$ as a representative of a strongly correlated perovskite manganite has been investigated as electrode material for OER with respect to the optical properties and the microscopic processes in the active state. These investigations cover doping and temperature dependent optical absorption spectroscopy, doping dependent cyclovoltammetry as well as in situ ETEM studies at different water vapor pressures and electron fluxes where the electron beam has been found to drive OER by inducing a positive electric potential in the electron irradiated specimen.

In chapter 2 it is shown that the strong electron-lattice coupling in PCMO gives rise to a broad double-peak structured optical absorption feature in the NIR/VIS range which originates from excitation between JT split states and photon-assisted polaron hopping allowing for an extensive absorption in the spectral range of solar light. The peak shape of the NIR absorption centered at $\hbar\omega \sim 1-2$ eV proves that the charge carriers in PCMO are small polarons in a wide doping ($0 \leq x \leq 0.8$) and temperature range ($80\ \mathrm{K} \leq T \leq 300\ \mathrm{K}$).

The evaluation of both peaks in the NIR-VIS absorption band on the basis of adiabatic small polaron theory [40, 109, 110] reveals that JT as well as Zener polaron dynamics are involved in the optical NIR-VIS absorption (Sec. 2.5). The presence of Zener polaron dynamics suggests a significant contribution of O $2p$ states to the UVBE in PCMO. This is confirmed by the non-linear doping trend of the spectral weight and the decreasing peak energy of the JT transition with increasing doping level (Sec. 2.5.2). For a reliable interpretation of these trends a doping dependent O $2p$ contribution to the UVBE has to be taken into account. Accordingly, the presented results prove that the electronic structure of PCMO and the polaron character (whether oxygen or manganese dominated) can be tuned by the doping level.

Referring to the temperature dependence of the optical absorption spectra, cooperative ordering effects like charge, orbital or magnetic ordering (see Fig.1.2b) in PCMO appear to have weak impact on the hopping energy as well as on the optical gap. In order to elucidate the role of cooperative ordering on the lifetime of excited polaron states,

temperature and time-dependent photoresistance measurements has been performed (see Appendix, chapter 6). A PCMO thin film sample ($x = 0.36$) was excited by a laser pulse with a photon energy of ~ 1.5 eV, which corresponds to the excitation between JT split states (cf. Fig. 2.3). The excitation causes a decrease of the PCMO sample resistance of the order of $\frac{dR}{R} < 3$ %, which relaxes on time scales of $1 - 100$ μs, depending on the temperature. These results indicate that polaron excitation from ordered states gives rise to long lifetimes of photo-excited polaron states. However, the impact of sample heating and experimental setup on the resistance relaxation could not be conclusively clarified. For details see Ref. [212].

From the viewpoint of catalysis the optical excitation between JT split states represents an interband transition with a presumably long-living excited polaronic state which, in contact with an aqueous electrolyte, may be transferred across the interface. The enhanced transport mobility under illumination due to photon assisted polaron hopping might further promote the transport to the interface. However, the photoactivity of PCMO electrodes for light-driven OER still needs to be carefully investigated. Evidence that PCMO also works as a photoanode for OER with light as the only driving force has not been provided in the framework of this thesis.

However, the electrochemical investigations presented in the chapters 3 and 4 clearly reveal that PCMO electrodes work as electrocatalysts for OER, albeit their OER activity is poor compared to well-established oxygen evolving electrocatalysts. [2, 213, 214] Conventional cyclovoltammetry experiments (Sec. 3.2.1 and 3.6.1) demonstrate OER in aqueous electrolyte at pH=7 at an overpotential of $\eta \approx 0.3 - 0.4$ V (for $j = 1$ μA/cm^2) with exchange current densities of $j_0 \sim 3 - 11$ nA (Fig. 3.2)[1].
The OER activity of PCMO has been also confirmed by in situ ETEM experiments in a gaseous $He/H_2O/SiH_4$ electrolyte. The secondary reaction of sacrificial SiH_4 with the evolved oxygen to SiO_2, which deposits as an amorphous layer on at catalytically active PCMO surfaces, uncovered the proceeding OER.

In the ETEM, the electron beam turned out to drive the OER reaction: Inelastic interactions of the electron beam with the specimen involve the emission of secondary electrons. Accordingly, hole charges accumulate within the specimen depending on the resistance connecting the electrode surface to ground potential. The experiments with the electrical TEM sample holder (Sec. 3.2.4), the electron holography experiments combined with electrostatic modeling of the electron beam induced potential as well as the theoretical considerations based on the secondary electron yield in chapter 4 prove the emergence of a positive electron beam induced electric potential in PCMO of the order of 1-2 V.

The stability of the investigated PCMO electrodes in the active state significantly

[1]Notably, RuO_2, $Ba_{0.5}Sr_{0.5}Co_{0.8}Fe_{0.2}O_{3-\delta}$ or various MnO-compounds representing high-performance electrodes reveal OER at much lower overpotential of $\eta \sim 0.25$ V with current densities up to mA/cm^2. [2, 213, 214]

depends on the Ca doping level x (Sec. 3.3.4). This is attributed to a correlation between the electrode stability and the O $2p$ contribution to the UVBE. Ca-rich (electron-doped) PCMO samples with enhanced O $2p$ contribution have reduced thermodynamic stability and tend to easily incorporate oxygen vacancies, [215–217] which seems facilitate degradation processes in terms of A-site dissolution and amorphization. OER activity rapidly decreases if degradation predominates. Hole-doped systems with higher Mn e_g contribution to the UVBE (due to the higher e_g-occupation) turned out to be more stable.

The OER activity with respect to the exchange current density and the overpotential (at $j \sim 1\mu\mathrm{A/cm^2}$) is highest for intermediate doping levels (Sec. 3.3.1-3.3.3). This result is to some extent in contradiction to the volcano-relation presented by Suntivich et al., [2] which predicts the highest OER activity at an e_g-occupation with one electron corresponding to the electronic configuration of $PrMnO_3$. In the considered branch of their volcano relation the desorption of an intermediate {O,H}-product from the electrode surface is assumed to be the rate-determining step in OER cycle. Thus, due to the higher occupation of anti-bonding e_g states, the weaker Mn-O bonding strength in e_g^1 compounds ($PrMnO_3$) compared to e_g^0 compounds ($CaMnO_3$) should give rise to a higher OER activity. However, the present work as well as other published results [215] show that $CaMnO_3$ or Ca-rich PCMO has the higher tendency to form oxygen vacancies (compared to weakly Ca-doped PCMO), which suggests a weaker Mn-O bond and higher OER activity in Ca-rich PCMO. This trend may be overlaid by the enhanced tendency of degradation with subsequent OER-deactivation of Ca-rich compounds leading to the observed activity maximum at intermediate Ca-doping and the decrease of OER activity for $x \widetilde{>} 0.5$.
Notably, our result of the highest activity for intermediate doping levels is in accordance with recently published results by Zaharieva et al. [14] The authors observed that Ca,Mn,O-based compounds with partly disordered MnO_6 units and mixed Mn^{3+}/Mn^{4+} valence reveal higher OER activity than the related single-valent Mn^{3+} and Mn^{4+} compounds. Moreover, the Mn oxidation state of the Mn ions in the Mn-Ca-based OER complex in the Photosystem II is presumed to alternate between 3+ and 4+ during the OER reaction cycle. [218–220] This supports our result of maximum OER activity for an average Mn oxidation between 3+ and 4+.

In analogy to the observations in artificial and natural photosynthesis, the EELS and XANES results presented in this work (Secs. 3.2.2, 4.3.1, 4.6.3) reveal that the Mn oxidation state at active PCMO surfaces changes during OER activity. Accordingly, PCMO provides sufficient flexibility to drive the OER. We attribute the varying Mn oxidation state in PCMO to the interplay of the generation and annihilation of oxygen vacancies during OER activity. Oxygen vacancies act as electron donors leading to a decrease of the Mn oxidation state. However, in contrast to the natural OER mechanism we observe a change to an Mn oxidation state below 3+ (Secs. 3.2.2 and 4.3.2). This suggests that Mn^{2+} ions are involved in catalytically active state of PCMO under the applied conditions due to an extensive formation of oxygen vacancies. This might be explained by an imbalance of vacancy generation and annihilation in active PCMO

regions. In presence of sacrificial SiH_4 the retarded vacancy annihilation is probably caused by the reaction of a portion of the lattice oxygen with SiH_4. A comparison of the oxygen content incorporated in the SiO_2 layer with the number of oxygen vacancies formed in PCMO clearly proves that the SiO_2 cover layer is not solely formed by lattice oxygen and that OER takes place in the ETEM (Secs. 3.2.3 and 4.6.9). Notably, ETEM experiments at water pressures < 5 μbar[2] in absence of sacrificial species, that captures the evolved oxygen, reveal a healing of TEM sample preparation induced oxygen vacancies. [221] This also points to the presence of an OER at active PCMO surfaces.
Our observations suggest that OER at PCMO electrode surfaces involves the formation of oxygen vacancies while the degree of reversibility, i.e. the rate of vacancy annihilation within the OER cycle, depends on the experimental conditions in the TEM, in particular the partial pressure of the evolved oxygen in the gas nearby the PCMO surface. The participation of lattice oxygen in the OER cycle implies a significant O $2p$ contribution to the UVBE in PCMO, which is consistent with the optical absorption results. Furthermore, it indicates that oxygen anions are the active surface sites of PCMO electrodes, which is in confirmation with recent results on Lanthanum and Iron-based perovskite oxide electrodes by Mueller et al. [29]

Giving a short outlook, Mother Nature teaches us that manganese based electrodes involving an Mn oxidation state between 3+and 4+ during OER have best performance. PCMO turns out to undergo excessive reduction under OER conditions to an Mn oxidation state $< 3+$ leading to a restraint of OER activity. Thus, conditions maintaining an oxidation state between 3+ and 4+ during activity or materials providing higher reversibility of oxygen vacancy formation have to be developed and established. Moreover, careful investigations of the energy dependent photoactivity of PCMO with respect to OER should tie in with the present work.

[2]This pure water vapor pressure roughly corresponds to the water partial pressure applied in the ETEM experiments in $He/H_2O/SiH_4$ gas mixture.

CHAPTER 6

Appendix

6.1 Time-Dependent Photoresistance Measurements

Time-dependent resistance measurements after a 5 ns laser pulse has been performed in collaboration with Nils Folchert at a PCMO (x=0.36) thin film epitaxially grown on MgO [001] substrate using a wavelength tunable OPO laser (Opolette 355 II) in order to investigate the lifetime of excited polaron states.

The applied experimental setup is illustrated in Fig. 6.1a (see also explanations in the

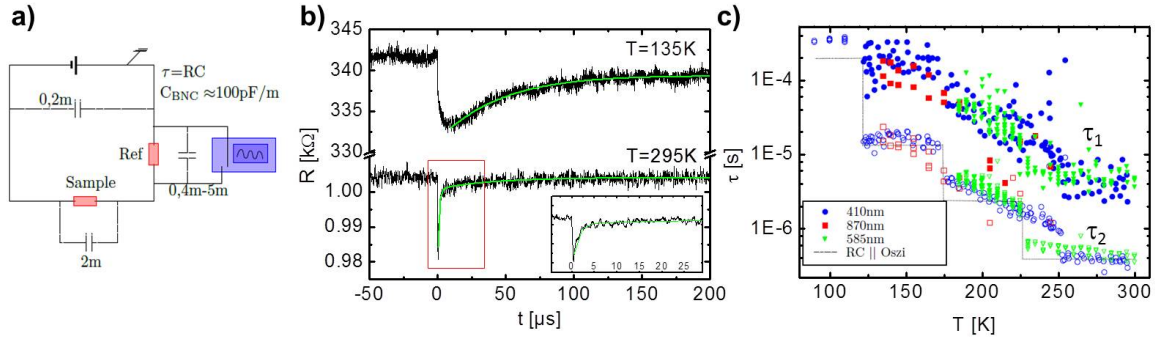

FIG. 6.1 a) Scheme of the experimental setup for the time-dependent photoresistance measurements. The distance information designates the length of the applied coaxial wires which contribute to the electrical circuit with a capacitance of $C_{coax} = 100$ pF/m. The photo-induced change of the sample resistance is detected via voltage measurement at an adjustable reference resistor using an oscilloscope and a source voltage of 1 V. b) $R(t)$-curves after a 5 ns pump pulse with $\lambda = 870$ nm at $T = 135$ K and room temperature and simulation according to Eq. 6.1. The inset shows the room temperature characteristics on a shorter time scale. c) The relaxation times gained from fitting $R(t)$ with Eq. 6.1 at wave lengths of 410 nm (blue symbols), 585 nm (green symbols) and 870 nm (red symbols) as a function of temperature. The image is taken from Ref. [212] Obviously, the short term relaxation strongly correlates with the experimental setup: The dashed line indicates the readjustment to another reference resistance.

figure caption). Fig. 6.1b shows two $R(t)$-measurements obtained at $T = 135$ K and room temperature after a pump pulse with $\lambda = 870$ nm. For both temperatures the resistance

relaxes exponentially with two characteristic time scales.

$$R(t > t_{min}) = R_0 - A_1 \cdot \exp\left(-\frac{t}{\tau_1}\right) - A_2 \cdot \exp\left(-\frac{t}{\tau_2}\right) \tag{6.1}$$

The relaxation times for different pump wavelengths is presented in Fig. 6.1c. Notably, the relaxation time strongly depends on the temperature. However, the short term relaxation with τ_2 correlates with the reference resistance and is, thus, considered as a measurement artifact originating from a parasitic capacitance in the RC circuit. The longer relaxation time τ_1 does not reveal an obvious correlation with the experimental setup and is accordingly regarded as an intrinsic relaxation process of the sample. The strong increase of τ_1 with decreasing temperature for $T < T_{CO} \sim 250$ K may be attributed to a retardation of the excited polaron relaxation with emerging charge ordering. Apparently, the measured relaxation times in the range of $1 - 100$ μs promise very long-living excited polaron states. However, sample heating and a resistance relaxation due to heat dissipation cannot be certainly excluded.
If heat dissipation is not the predominant resistance relaxation path, the relaxation time is expected to significantly depend on the excitation wavelength because time scales of dipole allowed and partly dipole forbidden recombination processes should be different. However, this is not observed: the relaxation for different excitation channels, i.e. on-site JT excitation at $\lambda \sim 800 - 900$ nm and O $2p \rightarrow$ minority t_{2g}/e_g charge transfer transitions at $\lambda \sim 400$ nm, occurs on similar time scales.

Bibliography

[1] H. M. Chen, C. K. Chen, R.-S. Liu, L. Zhang, J. Zhang, and D. P. Wilkinson. Nano-Architecture and Material Designs for Water Splitting Photoelectrodes. *Chemical Society Reviews*, 41(17):5654–5671, 2012.

[2] J. Suntivich, K. J. May, H. A. Gasteiger, J. B. Goodenough, and Y. Shao-Horn. A Perovskite Oxide Optimized for Oxygen Evolution Catalysis from Molecular Orbital Principles. *Science*, 334(6061):1383–1385, 2011.

[3] J. O. Bockris and T. Otagawa. The Electrocatalysis of Oxygen Evolution on Perovskites. *J. Electrochem. Soc.*, 131(2):290–302, 1984.

[4] Y. Surendranath, M. W. Kanan, and D. G. Nocera. Mechanistic studies of the oxygen evolution reaction by a cobalt-phosphate catalyst at neutral pH. *Journal of the American Chemical Society*, 132(46):16501–16509, 2010.

[5] M. Risch, J. Suntivich, and Y. Shao-Horn. Oxygen Evolution Reaction. In *Encyclopedia of Applied Electrochemistry*, pages 1475–1480. Springer, 2014.

[6] S. K. Tiwari, P. Chartier, and R. N. Singh. Preparation of Perovskite-Type Oxides of Cobalt by the Malic Acid Aided Process and Their Electrocatalytic Surface Properties in Relation to Oxygen Evolution. *Journal of The Electrochemical Society*, 142(1):148–153, 1995.

[7] A. Wattiaux, J. C. Grenier, M. Pouchard, and P. Hagenmuller. Electrolytic Oxygen Evolution in Alkaline Medium on $La_{1-x}Sr_xFeO_{3-y}$ Perovskite-Related Ferrites I. Electrochemical Study. *Journal of The Electrochemical Society*, 134(7):1714–1718, 1987.

[8] A. Grimaud, K. J. May, C. E. Carlton, Y.-L. Lee, M. Risch, W. T. Hong, J. Zhou, and Y. Shao-Horn. Double perovskites as a family of highly active catalysts for oxygen evolution in alkaline solution. *Nature communications*, 4, 2013.

[9] M. A. Peña and J. L. G. Fierro. Chemical Structures and Performance of Perovskite Oxides. *Chem. Rev.*, 101(7):1981–2018, 2001. PMID: 11710238.

[10] M. M. Najafpour, F. Rahimi, E.-M. Aro, C.-H. Lee, and S. I. Allakhverdiev. Nanosized Manganese Oxides as Biomimetic Catalysts for Water Oxidation in Artificial Photosynthesis: a Review. *Journal of The Royal Society Interface*, page rsif20120412, 2012.

[11] R. Lomoth, A. Magnuson, M. Sjödin, P. Huang, S. Styring, and L. Hammarström. Mimicking the Electron Donor Side of Photosystem II in Artificial Photosynthesis. *Photosynthesis research*, 87(1):25–40, 2006.

[12] F. A. Armstrong. Why did Nature Choose Manganese to Make Oxygen? *Phil. Trans. R. Soc. B*, 363(1494):1263–1270, 2008.

[13] I. McConnell, G. Li, and G. W. Brudvig. Energy Conversion in Natural and Artificial Photosynthesis. *Chemistry & biology*, 17(5):434–447, 2010.

[14] I. Zaharieva, M. M. Najafpour, M. Wiechen, M. Haumann, P. Kurz, and H. Dau. Synthetic Manganese-Calcium Oxides Mimic the Water-Oxidizing Complex of Photosynthesis Functionally and Structurally. *Energy & Environmental Science*, 4(7):2400–2408, 2011.

[15] J. P. McEvoy and G. W. Brudvig. Water-Splitting Chemistry of Photosystem II. *Chem. Rev.*, 106(11):4455–4483, 2006.

[16] L. M. Peter, K. G. U. Wijayantha, and A. A. Tahir. Kinetics of Light-Driven Oxygen Evolution at α-Fe_2O_3 Electrodes. *Faraday discussions*, 155:309–322, 2012.

[17] K. Sivula, F. Le Formal, and M. Grätzel. Solar Water Splitting: Progress using Hematite (α-Fe_2O_3) Photoelectrodes. *ChemSusChem*, 4(4):432–449, 2011.

[18] P. E. M. Siegbahn. Mechanisms for Proton Release during Water Oxidation in the S2 to S3 and S3 to S4 Transitions in Photosystem II. *Physical Chemistry Chemical Physics*, 14(14):4849–4856, 2012.

[19] A. Grundmeier and H. Dau. Structural Models of the Manganese Complex of Photosystem II and Mechanistic Implications. *Biochimica et Biophysica Acta (BBA)-Bioenergetics*, 1817(1):88–105, 2012.

[20] Y. Okimoto, Y. Tomioka, Y. Onose, Y. Otsuka, and Y. Tokura. Optical Study of $Pr_{1-x}Ca_xMnO_3 (x = 0.4)$ in a Magnetic Field: Variation of Electronic Structure with Charge Ordering and Disordering Phase Transitions. *Phys. Rev. B*, 59:7401–7408, Mar 1999.

[21] Y. S. Lee, T. Arima, S. Onoda, Y. Okimoto, Y. Tokunaga, R. Mathieu, X. Z. Yu, J. P. He, Y. Kaneko, Y. Matsui, N. Nagaosa, and Y. Tokura. Correlation of Electronic Structure and Ordered Charge and Orbital Patterns for Single-Layered Manganites in a Wide Hole-Doping Range ($0 \leq x \leq 1$). *Phys. Rev. B*, 75:144407, Apr 2007.

[22] J. H. Jung, K. H. Kim, T. W. Noh, E. J. Choi, and J. Yu. Midgap States of $La_{1-x}Ca_xMn_3$: Doping-Dependent Optical-Cconductivity Studies. *Phys. Rev. B*, 57:R11043–R11046, May 1998.

[23] S. Satpathy, Z. S. Popović, and F. R. Vukajlović. Electronic Structure of the Perovskite Oxides: $La_{1-x}Ca_xMnO_3$. *Physical review letters*, 76(6):960, 1996.

[24] J. Rossmeisl, Z.-W. Qu, H. Zhu, G.-J. Kroes, and J. K. Nørskov. Electrolysis of Water on Oxide Surfaces. *J. Electroanalytical Chemistry*, 607(1):83 – 89, 2007. Theoretical and Computational Electrochemistry.

[25] I. C. Man, H.-Y. Su, F. Calle-Vallejo, H. A. Hansen, J. I. Martinez, N. G. Inoglu, J. Kitchin, T. F. Jaramillo, J. K. Nørskov, and J. Rossmeisl. Universality in Oxygen Evolution Electrocatalysis on Oxide Surfaces. *Chem. Cat. Chem.*, 3(7):1159–1165, 2011.

[26] K. J. May, C. E. Carlton, K. A. Stoerzinger, M. Risch, J. Suntivich, Y.-L. Lee, A. Grimaud, and Y. Shao-Horn. Influence of Oxygen Evolution during Water Oxidation on the Surface of Perovskite Oxide Catalysts. *The Journal of Physical Chemistry Letters*, 3(22):3264–3270, 2012.

[27] M. W. Kanan and D. G. Nocera. In Situ Formation of an Oxygen-Evolving Catalyst in Neutral Water Containing Phosphate and Co^{2+}. *Science*, 321(5892):1072–1075, 2008.

[28] D. Mierwaldt, S. Mildner, R. Arrigo, A. Knop-Gericke, E. Franke, A. Blumenstein, J. Hoffmann, and Ch. Jooss. In Situ XANES/XPS Investigation of Doped Manganese Perovskite Catalysts. *Catalysts*, 4(2):129–145, 2014.

[29] D. N. Mueller, M. L. Machala, H. Bluhm, and W. C. Chueh. Redox Activity of Surface Oxygen Anions in Oxygen-Deficient Perovskite Oxides during Electrochemical Reactions. *Nature communications*, 6, 2015.

[30] Z. Jirák, S. Krupicka, Z. Šimša, M. Dlouhá, and S. Vratislav. Neutron Diffraction Study of $Pr_{1-x}Ca_xMnO_3$ Perovskites. *J. Magn. Magn. Mater.*, 53(1):153 – 166, 1985.

[31] P. G. Radaelli, M. Marezio, H. Y. Hwang, S. W. Cheong, and B. Batlogg. Charge Localization by Sstatic and Dynamic Distortions of the MnO_6 Octahedra in Perovskite Manganites. *Physical Review B*, 54(13):8992, 1996.

[32] D. I. Khomskii and G. A. Sawatzky. Interplay Between Spin, Charge and Orbital Degrees of Freedom in Magnetic Oxides. *Solid state communications*, 102(2):87–99, 1997.

[33] B. Halperin and R. Englman. Cooperative Dynamic Jahn-Teller Effect. II. Crystal Distortion in Perovskites. *Physical Review B*, 3(5):1698, 1971.

[34] R. Englman. *The Jahn-Teller effect in molecules and crystals.* Wiley-Interscience New York, 1972.

[35] M. D. Kaplan and B. G. Vekhter. *Cooperative Phenomena in Jahn-Teller Crystals.* Springer Science & Business Media, 2012.

[36] H. A. Jahn and E. Teller. Stability of Polyatomic Molecules in Degenerate Electronic States. I. Orbital Degeneracy. *Proceedings of the Royal Society of London. Series A, Mathematical and Physical Sciences*, pages 220–235, 1937.

[37] S. Asanuma, H. Akoh, H. Yamada, and A. Sawa. Relationship Between Rresistive Switching Characteristics and Band Diagrams of Ti/$Pr_{1-x}Ca_xMnO_3$ Junctions. *Phys. Rev. B*, 80(23):235113, 2009.

[38] R. Sopracase, G. Gruener, C. Autret-Lambert, V. T. Phuoc, V. Brizé, and J. C. Soret. Optical Rresponse to Magnetic Ordering in PrMnO_3: the Relevance of the Double Exchange Interaction. *arXiv preprint cond-mat/0609451*, 2006.

[39] L. D. Landau. Über die Bewegung der Elektronen im Kristall-Gitter. *Sow. Phys.*, 33:664–665, 1933.

[40] T. Holstein. Studies of Polaron Motion: Part I. The Molecular-Crystal Model. *Annals of Physics*, 8(3):325 – 342, 1959.

[41] H. Fehske and S. A. Trugman. Numerical Solution of the Holstein Polaron Problem. In *Polarons in Advanced Materials*, pages 393–461. Springer, 2007.

[42] D. Emin. Optical Properties of Large and Small Polarons and Bipolarons. *Phys. Rev. B*, 48:13691–13702, Nov 1993.

[43] J. T. Devreese and A. S. Alexandrov. Fröhlich Polaron and Bipolaron: Recent Developments. *Rep. Prog. Phys.*, 72(6):066501, 2009.

[44] Yu A. Firsov. Small Polarons: Transport Phenomena. *Semiconductors*, 29:515–537, 1995.

[45] C. C. Wang and L. W. Zhang. Polaron Relaxation Related to Localized Charge Carriers in $Pr_{1-x}Ca_xMnO_3$. *New Journal of Physics*, 9(7):210, 2007.

[46] J. Kanamori. Superexchange Interaction and Symmetry Properties of Electron Orbitals. *Journal of Physics and Chemistry of Solids*, 10(2):87–98, 1959.

[47] J. B. Goodenough. Theory of the Role of Covalence in the Perovskite-Type Manganites [La, M (II)] MnO_3. *Physical Review*, 100(2):564, 1955.

[48] J. B. Goodenough. *Magnetism and Chemical Bond*, volume 1. Interscience Publ., 1963.

[49] K. Kubo and N. Ohata. A Quantum Theory of Double Exchange. I. *Journal of the Physical society of Japan*, 33(1):21–32, 1972.

[50] C. Zener. Interaction Between the d Shells in the Transition Metals. *Physical Review*, 81(3):440, 1951.

[51] P. W. Anderson and H. Hasegawa. Considerations on Double Exchange. *Physical Review*, 100(2):675, 1955.

[52] Y. Tokura. *Colossal Magnetoresistive Oxides (Advances in Condensed Matter Science)*, volume 2. Gordon and Breach, Amsterdam, 2000.

[53] C. Martin, A. Maignan, M. Hervieu, and B. Raveau. Magnetic Phase Diagrams of $L_{1-x}A_xMnO_3$ Manganites (L=Pr,Sm; A=Ca, Sr). *Physical Review B*, 60(17):12191, 1999.

[54] P. V. Riboud and A. Muan. Melting Relations of CaO-Manganese Oxide and MgO-Manganese Oxide Mixtures in Air. *Journal of the American Ceramic Society*, 46(1):33–36, 1963.

[55] J. Hoffmann, P. Moschkau, S. Mildner, J. Norpoth, Ch. Jooss, L. Wu, and Y. Zhu. Effects of Interaction and Disorder on Polarons in Colossal Resistance Manganite $Pr_{0.68}Ca_{0.32}MnO_3$ Thin Films. *Materials Research Express*, 1(4):046403, 2014.

[56] M Fiebig, K Miyano, Y Tomioka, and Y Tokura. Ultrafast photoinduced insulator–metal transition in $Pr_{0.7}Ca_{0.3}MnO_3$. *Journal of luminescence*, 87:82–85, 2000.

[57] K. H. Höck, H. Nickisch, and H. Thomas. Jahn-Teller Effect in Itinerant Electron Systems: The Jahn-Teller Polaron. *Helvetica Physica Acta*, 56:237, 1983.

[58] A. Shengelaya, G.-M. Zhao, H. Keller, and K. A. Müller. EPR Evidence of Jahn-Teller Polaron Formation in $La_{1-x}Ca_xMnO_{3+y}$. *Physical review letters*, 77(26):5296, 1996.

[59] M. Quijada, J. Černe, J. R. Simpson, H. D. Drew, K. H. Ahn, A. J. Millis, R. Shreekala, R. Ramesh, M. Rajeswari, and T. Venkatesan. Optical Conductivity of Manganites: Crossover from Jahn-Teller Small Polaron to Coherent Transport in the Ferromagnetic State. *Phys. Rev. B*, 58:16093–16102, Dec 1998.

[60] Ch. Jooss, L. Wu, T. Beetz, R. F. Klie, M. Beleggia, M. A. Schofield, S. Schramm, J. Hoffmann, and Y. Zhu. Polaron Melting and Ordering as Key Mechanisms for Colossal Resistance Effects in Manganites. *Proc. Natl. Acad. Sci. U.S.A.*, 104(34):13597–13602, 2007.

[61] C. H. Patterson. Competing Crystal Structures in $La_{0.5}Sr_{0.5}MnO_3$: Conventional Charge Order Versus Zener Polarons. *Phys. Rev. B*, 72:085125, Aug 2005.

[62] A. Daoud-Aladine, J. Rodriguez-Carvajal, L. Pinsard-Gaudart, M. T. Fernandez-Diaz, and A. Revcolevschi. Zener Polaron Ordering in Half-Doped Manganites. *Physical review letters*, 89(9):097205, 2002.

[63] P. Barone, S. Picozzi, and J. van den Brink. Buckling-Induced Zener Polaron Instability in Half-Doped Manganites. *Phys. Rev. B*, 83:233103, Jun 2011.

[64] L. Wu, R. F. Klie, Y. Zhu, and Ch. Jooss. Experimental Confirmation of Zener-polaron-type Charge and Orbital Ordering in $Pr_{1-x}Ca_xMnO_3$. *Phys. Rev. B*, 76(17):174210, 2007.

[65] Y. A. Firsov and E. K. Kudinov. The Polaron State of a Crystal. *Phys. Solid State*, 43(3):447–457, 2001.

[66] O. Laporte and W. F. Meggers. Some Rules of Spectral Structure. *J. Opt. Soc. Am.*, 11(5):459–460, Nov 1925.

[67] P. Atkins and J. De Paula. *Elements of Physical Chemistry.* Oxford University Press, 2013. p. 477-529.

[68] F. Schwabl. *Quantenmechanik (QMI).* Springer-Verlag, 2013. p. 298 ff.

[69] A. S. Moskvin, A. A. Makhnev, L. V. Nomerovannaya, N. N. Loshkareva, and A. M. Balbashov. Interplay of *p-d* and *d-d* Charge Transfer Transitions in Rare-Earth Perovskite Manganites. *Phys. Rev. B*, 82:035106, Jul 2010.

[70] J. E. Huheey, E. A. Keiter, and R. L. Keiter. Anorganische Chemie, Vol. 2, 1995. p. 508 ff.

[71] J. Sun, D. K. Zhong, and D. R. Gamelin. Composite Photoanodes for Photoelectrochemical Solar Water Splitting. *Energy & Environmental Science*, 3(9):1252–1261, 2010.

[72] A. Kudo and Y. Miseki. Heterogeneous Photocatalyst Materials for Water Splitting. *Chem. Soc. Rev.*, 38:253–278, 2009.

[73] CH Hamann and W Vielstich. *Elektrochemie, 4., vollst. überarb. und aktualisierte Aufl.* Wiley-VCH, Weinheim, 2005.

[74] J. Zach and M. Haider. Correction of Spherical and Chromatic Aberrations in a LVSEM. *Proc. 13th Int. Congr. Electron Microscopy, Paris, France*, 1:199–200, 1994.

[75] M. Haider, H. Rose, S. Uhlemann, E. Schwan, B. Kabius, and K. Urban. A Spherical-Aberration-Corrected 200kV Transmission Electron Microscope. *Ultramicroscopy*, 75(1):53–60, 1998.

[76] M. Haider, H. Rose, S. Uhlemann, B. Kabius, and K. Urban. Towards 0.1 nm Resolution with the First Spherically Corrected Ttransmission Electron Microscope. *Journal of electron microscopy*, 47(5):395–405, 1998.

[77] O. L. Krivanek, G. J. Corbin, N. Dellby, B. F. Elston, R. J. Keyse, M. F. Murfitt, C. S. Own, Z. S. Szilagyi, and J. W. Woodruff. An Electron Microscope for the Aberration-Corrected Era. *Ultramicroscopy*, 108(3):179–195, 2008.

[78] N. Tanaka, J. Yamasaki, K. Usuda, and N. Ikarashi. First Observation of SiO_2/Si (100) Interfaces by Spherical Aberration-Corrected High-Resolution Transmission Electron Microscopy. *Journal of electron microscopy*, 52(1):69–73, 2003.

[79] B. Freitag, S. Kujawa, P. M. Mul, J. Ringnalda, and P. C. Tiemeijer. Breaking the Spherical and Chromatic Aberration Barrier in Transmission Electron Microscopy. *Ultramicroscopy*, 102(3):209–214, 2005.

[80] L. Y. Chang, A S. Barnard, L. C. Gontard, and R. E. Dunin-Borkowski. Resolving the Structure of Active Sites on Platinum Catalytic Nanoparticles. *Nano Lett.*, 10(8):3073–3076, 2010. PMID: 20666362.

[81] T. W. Hansen, J. B. Wagner, and R. E. Dunin-Borkowski. Aberration Corrected and Monochromated Environmental Transmission Electron Microscopy: Challenges and Prospects for Materials Science. *Mater. Sci. Technol.*, 26(11):1338–1344, 2010.

[82] R. Egerton. *Electron Energy-Loss Spectroscopy in the Eelectron Microscope*. Springer Science & Business Media, 2011.

[83] J. I. Goldstein, D. E. Newbury, P. Echlin, D. C. Joy, Ch. Fiori, E. Lifshin, et al. *Scanning Electron Microscopy and X-Rray Microanalysis. A Text for Biologists, Materials Scientists, and Geologists*. Plenum Publishing Corporation, 1981.

[84] F. Cavalca, Anders B. Laursen, B. E. Kardynal, R. E. Dunin-Borkowski, S. Dahl, J. B. Wagner, and T. W. Hansen. In Situ Transmission Electron Microscopy of Light-Induced Photocatalytic Reactions. *Nanotechnology*, 23(7):075705, 2012.

[85] J. F. Creemer, S. Helveg, G. H. Hoveling, S. Ullmann, A. M. Molenbroek, P. M. Sarro, and H. W. Zandbergen. Atomic-Scale Eelectron Microscopy at Ambient Pressure. *Ultramicroscopy*, 108(9):993–998, 2008.

[86] Q. Chen and L.-M. Peng. Fabrication and Electric Measurements of Nanostructures inside Transmission Electron Microscope. *Ultramicroscopy*, 111(7):948–954, 2011.

[87] Pratibha L Gai. Developments in In Situ Eenvironmental Cell high-Resolution Electron Microscopy and Applications to Catalysis. *Topics in catalysis*, 21(4):161–173, 2002.

[88] B. K. Miller and P. A. Crozier. System for In Situ UV-Visible Illumination of Environmental Transmission Electron Microscopy Samples. *Microscopy and Microanalysis*, 19(02):461–469, 2013.

[89] T. Kawasaki, T. Miura, H. Tsutsui, T. Matsutani, and T. Tanji. Development of a New Closed-type Environmental-cell Specimen Holder with High Gas Conductivity. *Microscopy and Microanalysis*, 16(S2):332–333, 2010.

[90] V. E. Cosslett. Radiation Damage in the High Resolution Electron Microscopy of Biological Materials: A Review. *Journal of microscopy*, 113(2):113–129, 1978.

[91] R. F. Egerton, P. Li, and M. Malac. Radiation Damage in the TEM and SEM. *Micron*, 35(6):399–409, 2004.

[92] D. B. Williams and C. B. Carter. *The Transmission Electron Microscope*. Springer, 1996.

[93] J. Cazaux. Mechanisms of Charging in Electron Spectroscopy. *Journal of Electron Spectroscopy and Related Phenomena*, 105(2):155–185, 1999.

[94] A. Lanzara, N. L. Saini, M. Brunelli, F. Natali, A. Bianconi, P. G. Radaelli, and S.-W. Cheong. Crossover from Large to Small Ppolarons Across the Metal-Iinsulator Transition in Manganites. *Phys. Rev. Lett.*, 81(4):878, 1998.

[95] M. Jaime, M. B. Salamon, M. Rubinstein, R. E. Treece, J. S. Horwitz, and D. B. Chrisey. High-Temperature Thermopower in $La_{2/3}Ca_{1/3}MnO_3$ Films: Evidence for Polaronic Transport. *Phys. Rev. B*, 54(17):11914–11917, Nov 1996.

[96] A. J. Millis, P. B. Littlewood, and B. I. Shraiman. Double Exchange Alone does not Explain the Resistivity of $La_{1-x}Sr_xMnO_3$. *Phys. Rev. Lett.*, 74(25):5144, 1995.

[97] S. Schramm, J. Hoffmann, and Ch. Jooss. Transport and Ordering of Polarons in CER Manganites PrCaMnO. *J. Phys.: Condens. Matter*, 20(39):395231, 2008.

[98] G. M. Zhao, Y. S. Wang, D. J. Kang, W. Prellier, M. Rajeswari, H. Keller, T. Venkatesan, C. W. Chu, and R. L. Greene. Evidence for the Immobile Bipolaron Formation in the Paramagnetic State of the Magnetoresistive Manganites. *Phys. Rev. B*, 62(18):R11949–R11952, Nov 2000.

[99] D. Louca, T. Egami, E. L. Brosha, H. Röder, and A. R. Bishop. Local Jahn-Teller Distortion in $La_{1-x}Sr_xMnO_3$ Observed by Pulsed Neutron Diffraction. *Phys. Rev. B*, 56(14):R8475–R8478, Oct 1997.

[100] I. G. Austin and N. F. Mott. Polarons in Crystalline and Non-Crystalline Materials. *Adv. Phys.*, 18(71):41–102, 1969.

[101] Ch. Hartinger, F. Mayr, A. Loidl, and T. Kopp. Polaronic Excitations in Colossal Magnetoresistance Manganite Films. *Phys. Rev. B*, 73:024408, Jan 2006.

[102] N. N. Loshkareva, L. V. Nomerovannaya, E. V. Mostovshchikova, A. A. Makhnev, Yu. P. Sukhorukov, N. I. Solin, T. I. Arbuzova, S. V. Naumov, N. V. Kostromitina, A. M. Balbashov, and L. N. Rybina. Electronic Structure and Polarons in $CaMnO_{3-\delta}$ Single Crystals: Optical Data. *Phys. Rev. B*, 70:224406, Dec 2004.

[103] V. N. Bogomolov and D. N. Mirlin. Optical Absorption by Polarons in Rutile (TiO_2) Single Crystals. *Phys. Stat. Sol. (b)*, 27(1):443–453, 1968.

[104] G. Saucke, J. Norpoth, Ch. Jooss, D. Su, and Y. Zhu. Polaron Absorption for Photovoltaic Energy Conversion in a Manganite-Titanate *pn* Heterojunction. *Phys. Rev. B*, 85:165315, Apr 2012.

[105] N. N. Kovaleva, A. M. Oleś, A. M. Balbashov, A. Maljuk, D. N. Argyriou, G. Khaliullin, and B. Keimer. Low-Energy Mott-Hubbard Excitations in $LaMnO_3$ probed by Optical Ellipsometry. *Physical Review B*, 81(23):235130, 2010.

[106] J. H. Jung, K. H. Kim, D. J. Eom, T. W. Noh, E. J. Choi, J. Yu, Y. S. Kwon, and Y. Chung. Determination of Eelectronic Band Structures of $CaMnO_3$ and $LaMnO_3$ Using Optical-Conductivity Analyses. *Phys. Rev. B*, 55:15489–15493, Jun 1997.

[107] J.-H. Park, C. T. Chen, S.-W. Cheong, W. Bao, G. Meigs, V. Chakarian, and Y. U. Idzerda. Electronic Aspects of the Ferromagnetic Transition in Manganese Perovskites. *Phys. Rev. Lett.*, 76:4215–4218, May 1996.

[108] P. Grossmann, I. Rajkovic, R. Moré, J. Norpoth, S. Techert, C. Jooss, and K. Mann. Time-Resolved Near-Edge X-Ray Absorption Fine Structure Spectroscopy on Photo-Induced Phase Transitions Using a Tabletop Soft-X-Ray Spectrometer. *Review of Scientific Instruments*, 83(5):053110, 2012.

[109] H. G. Reik and D. Heese. Frequency Dependence of the Electrical Conductivity of Small Polarons for High and Low Temperatures . *J. Phys. Chem. Solids*, 28(4):581 – 596, 1967.

[110] S. Fratini and S. Ciuchi. Optical Properties of Small Polarons from Dynamical Mean-Field Theory. *Phys. Rev. B*, 74:075101, Aug 2006.

[111] A. Machida, Y. Moritomo, and A. Nakamura. Spectroscopic Evidence for Formation of Small Polarons in Doped Manganites. *Phys. Rev. B*, 58:R4281–R4284, Aug 1998.

[112] S. Yoon, H. L. Liu, G. Schollerer, S. L. Cooper, P. D. Han, D. A. Payne, S.-W. Cheong, and Z. Fisk. Raman and Optical Spectroscopic Studies of Small-to-Large Polaron Crossover in the Perovskite Manganese Oxides. *Physical Review B*, 58(5):2795, 1998.

[113] P. Hohenberg and W. Kohn. Inhomogeneous Electron Gas. *Phys. Rev.*, 136:B864–B871, Nov 1964.

[114] W. Kohn and L. J. Sham. Self-Consistent Equations Including Exchange and Correlation Effects. *Phys. Rev.*, 140:A1133–A1138, Nov 1965.

[115] P. E. Blöchl. Projector Augmented-Wave Method. *Phys. Rev. B*, 50:17953–17979, Dec 1994.

[116] A. D. Becke. A New Mixing of Hartree-Fock and Local Density-Functional Theories. *J. Chem. Phys.*, 98(2):1372–1377, 1993.

[117] P. Novák, J. Kuneš, L. Chaput, and W. E. Pickett. Exact Exchange for Correlated Electrons. *Phys. Stat. Sol. (b)*, 243(3):563–572, 2006.

[118] F. Tran, P. Blaha, K. Schwarz, and P. Novák. Hybrid Exchange-Correlation Energy Functionals for Strongly Correlated Electrons: Applications to Ttransition-Metal Monoxides. *Phys. Rev. B*, 74:155108, Oct 2006.

[119] J. P. Perdew, K. Burke, and M. Ernzerhof. Generalized Gradient Approximation Made Simple. *Phys. Rev. Lett.*, 77:3865–3868, Oct 1996.

[120] D. Feinberg, S. Ciuchi, and F. de Pasquale. Sqeezing Phenomena in Interacting Electron-Phonon Systems. *Int. J. Mod. Phys. B*, 4(7):1317–1367, 1990.

[121] D. Emin. Phonon-Assisted Transition Rrates I. Optical-Phonon-Assisted Hopping in Solids. *Adv. Phys.*, 24(3):305–348, 1975.

[122] T. Kawasaki, Y. Ogimoto, N. Ogawa, K. Miyano, H. Tamaru, and M. Izumi. Charge- and Orbital-Ordering Patterns in Bi12Sr12MnO3 Thin Films Studied by Raman Scattering. *J. Appl. Phys.*, 101(12):123714, 2007.

[123] M. Rini, R. Tobey, N. Dean, J. Itatani, Y. Tomioka, Y. Tokura, R. W. Schoenlein, and A. Cavalleri. Control of the Electronic Phase of a Manganite by Mode-Sselective Vibrational Excitation. *Nature*, 449(7158):72–74, 2007.

[124] Y. A. Firsov. Form of the Absorption Curve for Interaction of Light with Small Polarons. *Phys. Sol. State, USSR [FIZ TVERD TELA+]*, 10(7):1537, 1969.

[125] E. K. Kudinov and Y.A. Firsov. Interband Optical Transitions in Low Mobility Semiconductors. *J. Exptl. Theoret. Phys. (U.S.S.R.)*, 47:601–614, 1965. [Sov. Phys. JETP-USSR 20, 400-408 (1965)].

[126] R. Sopracase, G. Gruener, E. Olive, Soret, and J.-C. Infrared Study of the Phonon Modes in $PrMnO_3$ and $CaMnO_3$. *Physica B: Condensed Matter*, 405(1):45 – 52, 2010.

[127] J. P. Hill, C. S. Nelson, M. v. Zimmermann, Y.-J. Kim, D. Gibbs, D. Casa, B. Keimer, Y. Murakami, C. Venkataraman, T. Gog, Y. Tomioka, Y. Tokura, V. Kiryukhin, T. Y. Koo, and S.-W. Cheong. Orbital Correlations in Doped Manganites. *Appl. Phys. A Mater. Sci. Process.*, 73(6):723–730, 2001.

[128] C. Cui and T. A. Tyson. Pressure Effects on Charge, Spin, and Metal-Insulator Transitions in the Narrow Bandwidth Manganite $Pr_{1-x}Ca_xMnO_3$. *Phys. Rev. B*, 70:094409, Sep 2004.

[129] V. Markovich, I. Fita, A. I. Shames, R. Puzniak, E. Rozenberg, C. Martin, A. Wisniewski, Y. Yuzhelevskii, A. Wahl, and G. Gorodetsky. Magnetic, Transport, and Electron Magnetic Resonance Properties of $Pr_{0.8}Ca_{0.2}MnO_3$ Single Crystals. *Phys. Rev. B*, 68:094428, Sep 2003.

[130] A. Antonakos, D. Palles, E. Liarokapis, M. Filippi, and W. Prellier. Evaluation of the Strains in Charge-Ordered $Pr_{1-x}Ca_xMnO_3$ Thin Films using Raman Spectroscopy. *J. Appl. Phys.*, 104(6):063508, 2008.

[131] N. C. Yeh, R. P. Vasquez, D. A. Beam, C. C. Fu, J. Huynh, and G. Beach. Effects of Lattice Distortion and Jahn-Teller Coupling on the Magnetoresistance of and Epitaxial Films. *J. Phys. Condens. Matter*, 9(18):3713, 1997.

[132] E. Dagotto. *Nanoscale Phase Separation and Colossal Magnetoresistance: the Physics of Manganites and Related Compounds*, volume 136. Springer - Verlag Berling Heidelberg, 2003.

[133] K. J. Thomas, J. P. Hill, S. Grenier, Y-J. Kim, P. Abbamonte, L. Venema, A. Rusydi, Y. Tomioka, Y. Tokura, D. F. McMorrow, G. Sawatzky, and M. van Veenendaal. Soft X-Ray Resonant Diffraction Study of Magnetic and Orbital Correlations in a Manganite Near Half Doping. *Phys. Rev. Lett.*, 92:237204, Jun 2004.

[134] S. G. Kaplan, M. Quijada, H. D. Drew, D. B. Tanner, G. C. Xiong, R. Ramesh, C. Kwon, and T. Venkatesan. Optical Evidence for the Dynamic Jahn-Teller Effect in $Nd_{0.7}Sr_{0.3}MnO_3$. *Phys. Rev. Lett.*, 77:2081–2084, Sep 1996.

[135] C. Roos, A. Köhn, J. Gauss, and G. Diezemann. The Temperature Dependence of Vibronic Lineshapes: Linear Electron-Phonon Coupling. *J. Chem. Phys.*, 141(15):154110, 2014.

[136] K. Ebata, M. Hashimoto, K. Tanaka, A. Fujimori, Y. Tomioka, and Y. Tokura. Temperature-Dependent Photoemission Spectra, Spectral Weight Transfer, and Chemical Ppotential Shift in $Pr_{1-x}Ca_xMnO_3$: Implications for Charge-Density Modulation. *Phys. Rev. B*, 76:174418, Nov 2007.

[137] L. I. Krishtalik. Energetics of Multielectron Reactions. Photosynthetic Oxygen Evolution . *Biochim. Biophys. Acta*, 849(1):162 – 171, 1986.

[138] K. N. Ferreira, T. M. Iverson, K. Maghlaoui, J. Barber, and S. Iwata. Architecture of the Photosynthetic Oxygen-Evolving Center. *Science*, 303(5665):1831–1838, 2004.

[139] J. Barber. Photosynthetic Energy Conversion: Natural and Artificial. *Chem. Soc. Rev.*, 38(1):185–196, 2009.

[140] H. Dau and I. Zaharieva. Principles, Efficiency, and Blueprint Character of Solar-Energy Conversion in Photosynthetic Water Oxidation. *Acc. Chem. Res.*, 42(12):1861–1870, 2009.

[141] J. Messinger. Evaluation of Different Mechanistic Proposals for Water Oxidation in Photosynthesis on the Basis of Mn_4O_xCa Structures for the Catalytic Site and Spectroscopic Data. *Phys. Chem. Chem. Phys.*, 6(20):4764–4771, 2004.

[142] G. F. Moore and G. W. Brudvig. Energy Conversion in Photosynthesis: a Paradigm for Solar Fuel Production. *Annu. Rev. Condens. Matter Phys.*, 2(1):303–327, 2011.

[143] F. E. Osterloh. Inorganic Materials as Catalysts for Photochemical Splitting of Water. *Chem. Mater.*, 20(1):35–54, 2008.

[144] B. Viswanathan, Ch. Venkateswara Rao, and U. V. Varadaraju. On the Search for Non-Noble Metal Based Electrodes for Oxygen Reduction Reaction. *Photo/Electrochemistry & Photobiology in the Environment, Energy and Fuel*, pages 43 – 101, 2006.

[145] E. M. Fernández, P. G. Moses, A. Toftelund, H. A. Hansen, J. I. Martinez, F. Abild-Pedersen, J. Kleis, B. Hinnemann, J. Rossmeisl, T. Bligaard, and J. K Nørskov. Scaling Relationships for Adsorption Energies on Transition Metal Oxide, Sulfide, and Nitride Surfaces. *Angew. Chem.*, 120:4761—4764, 2008.

[146] A. Vojvodic and J. K. Nørskov. Optimizing Perovskites for the Water-Splitting Reaction. *Science*, 334(6061):1355–1356, 2011.

[147] B. Raveau. The Crucial Role of Mixed Valence in the Mmagnetoresistance Properties of Manganites and Cobaltites. *Phil. Trans. R. Soc. A*, 366(1862):83–92, 2008.

[148] E. D. Boyes and P.L. Gai. Environmental High Resolution Electron Microscopy and Applications to Chemical Science. *Ultramicroscopy*, 67(1):219–232, 1997. Frontiers in Electron Microscopy in Materials Science.

[149] P. L. Hansen, J. B. Wagner, S. Helveg, J. R. Rostrup-Nielsen, B. S. Clausen, and H. Topsøe. Atom-Resolved Imaging of Dynamic Shape Changes in Supported Copper Nanocrystals. *Science*, 295(5562):2053–2055, 2002.

[150] S. Helveg, C. López-Cartes, J. Sehested, P. L. Hansen, B. S. Clausen, J. R. Rostrup-Nielsen, F. Abild-Pedersen, and J. K Nørskov. Atomic-Scale Imaging of Carbon Nanofibre Growth. *Nature*, 427(6973):426–429, 2004.

[151] K. H. Downing, M. R. McCartney, and R. M. Glaeser. Experimental Characterization and Mitigation of Specimen Charging on Thin Films with One Conducting Layer. *Microsc. Microanal.*, 10(06):783–789, 2004.

[152] F. Ramezanipour, J. E. Greedan, J. Siewenie, Th. Proffen, D. H. Ryan, A. P. Grosvenor, and R. L. Donaberger. Local and Average Structures and Magnetic Properties of Sr_2FeMnO_{5+y}, $y = 0.0, 0.5$. Comparisons with Ca_2FeMnO_5 and the Effect of the A-Site Cation. *Inorganic Chemistry*, 50(16):7779–7791, 2011. PMID: 21766787.

[153] G. Zampieri, M. Abbate, F. Prado, A. Caneiro, and E. Morikawa. XPS and XAS Spectra of $CaMnO_3$ and $LaMnO_3$. *Physica B: Condensed Matter*, 320(1):51 – 55, 2002. Proceedings of the Fifth Latin American Workshop on Magnetism, Magnetic Materials and their Applications.

[154] J. Kotakoski, C. H. Jin, O. Lehtinen, K. Suenaga, and A. V. Krasheninnikov. Electron Knock-On Damage in Hexagonal Boron Nitride Monolayers. *Phys. Rev. B*, 82:113404, Sep 2010.

[155] S. Mildner, M. Beleggia, D. Mierwaldt, T. W. Hansen, J. B. Wagner, S. Yazdi, T. Kasama, J. Ciston, Y. Zhu, and Ch. Jooss. Environmental TEM Study of Electron Beam Induced Electrochemistry of $Pr_{0.64}Ca_{0.36}MnO_3$ Catalysts for Oxygen Evolution. *The Journal of Physical Chemistry C*, ASAP, 2015.

[156] J. D. Ferguson, Y. Kim, L. F. Kourkoutis, A. Vodnick, A. R. Woll, D. A. Muller, and J. D. Brock. Epitaxial Oxygen Getter for a Brownmillerite Phase Transformation in Manganite Films. *Advanced Materials*, 23(10):1226–1230, 2011.

[157] S. Bakardjieva, P. Bezdicka, T. Grygar, and P. Vorm. Reductive Dissolution of Microparticulate Manganese Oxides. *J. Solid State Electrochem.*, 4(6):306–313, 2000.

[158] A. Nemudry, P. Rudolf, and R. Schöllhorn. Topotactic Electrochemical Redox Reactions of the Defect Perovskite $SrCoO_{2.5+x}$. *Chemistry of Materials*, 8(9):2232–2238, 1996.

[159] E. Beyreuther, S. Grafström, L. M. Eng, Ch. Thiele, and K. Dörr. XPS investigation of Mn Valence in Lanthanum Manganite Thin Films under Variation of Oxygen Content. *Phys. Rev. B*, 73:155425, Apr 2006.

[160] T. Grygar. Electrochemical Reactions of $La(Ni,Cr)O_3$ and $La(Ni,Fe)O_3$ in Acidic Aqueous Solutions. *J. Solid State Electrochem.*, 3(7-8):412–416, 1999.

[161] F. Calle-Vallejo, J. I. Martínez, J. M. García-Lastra, M. Mogensen, and J. Rossmeisl. Trends in Stability of Perovskite Oxides. *Angew. Chem.*, 49(42):7699–7701, 2010.

[162] E. M. Vass, M. Hävecker, S. Zafeiratos, D. Teschner, A. Knop-Gericke, and R. Schlögl. The Role of Carbon Species in Heterogeneous Catalytic Processes: an In Situ Soft X-Ray Photoelectron Spectroscopy Study. *J. Phys.: Condens. Matter*, 20(18):184016, 2008.

[163] C. Adamo and V. Barone. Toward Reliable Density Functional Methods without Adjustable Parameters: The PBE0 Model. *J. Chem. Phys.*, 110(13):6158–6170, 1999.

[164] https://www2.pt.tu-clausthal.de/paw/.

[165] D. W. Reagor, S. Y. Lee, Y. Li, and Q. X. Jia. Work Function of the Mixed-Valent Manganese Perovskites. *J. Appl. Phys.*, 95(12):7971–7975, 2004.

[166] K. Ebata, H. Wadati, M. Takizawa, A. Fujimori, A. Chikamatsu, H. Kumigashira, M. Oshima, Y. Tomioka, and Y. Tokura. Chemical Potential Shift and Spectral-Weight Transfer in $Pr_{1-x}Ca_xMnO_3$ revealed by Photoemission Spectroscopy. *Phys. Rev. B*, 74(6):064419, 2006.

[167] J. R. Sun, S. Y. Zhang, B. G. Shen, and H. K. Wong. Rectifying and Photovoltaic Properties of the Heterojunction Composed of $CaMnO_3$ and Nb-Doped $SrTiO_3$. *Appl. Phys. Lett.*, 86(5):053503, 2005.

[168] A. Filippetti and W. E. Pickett. Magnetic Reconstruction at the (001) $CaMnO_3$ Surface. *Phys. Rev. lett.*, 83(20):4184, 1999.

[169] E. Wiberg, N. Wiberg, and A. F. Holleman. *Inorganic Chemistry*. Academic Press, 2001.

[170] S.-W. Hu, Y. Wang, X.-Y. Wang, T.-W. Chu, and X.-Q. Liu. Gas-phase Reactions between Silane and Water: A Theoretical Study. *J. Phys. Chem. A*, 108(8):1448–1459, 2004.

[171] T. Riedl, T. Gemming, and K. Wetzig. Extraction of EELS White-Line Intensities of Manganese Compounds: Methods, Accuracy, and Valence Sensitivity. *Ultramicroscopy*, 106(4):284–291, 2006.

[172] M. Varela, M. P. Oxley, W. Luo, J. Tao, M. Watanabe, A. R. Lupini, S. T. Pantelides, and S. J. Pennycook. Atomic-Resolution Imaging of Oxidation States in Manganites. *Phys. Rev. B*, 79(8):085117, 2009.

[173] R. D. Leapman, L. A. Grunes, and P. L. Fejes. Study of the L_{23} Edges in the 3*d* Transition Metals and their Oxides by Electron-Energy-Loss Spectroscopy with Comparisons to Theory. *Phys. Rev. B*, 26(2):614, 1982.

[174] J. Lipkowski and P. N. Ross. *Frontiers in Electrochemistry. Electrocatalysis*. Wiley-VCH: New York, 1998.

[175] G. J. Hutchings, A. Desmartin-Chomel, R. Olier, and J.-C. Volta. Role of the Product in the Transformation of a Catalyst to its Active State. *Nature*, 368:41, 1994.

[176] L. Trotochaud and S. W. Boettcher. Precise Oxygen Evolution catalysts: Status and Opportunities. *Scr. Mater.*, 74:25–32, 2014.

[177] R. Arrigo, M. Hävecker, M. E.M Schuster, C. Ranjan, E. Stotz, A. Knop-Gericke, and R. Schlögl. In Situ Study of the Gas-Phase Electrolysis of Water on Platinum by NAP-XPS. *Angew. Chem.*, 52(44):11660–11664, 2013.

[178] F. Zheng, S. Alayoglu, J. Guo, V. Pushkarev, Y. Li, P.-A. Glans, J.-L. Chen, and G. Somorjai. In-Situ X-ray Absorption Study of Evolution of Oxidation States and Structure of Cobalt in Co and CoPt Bimetallic Nanoparticles (4 nm) under Reducing (H_2) and Oxidizing (O_2) Environments. *Nano Lett.*, 11(2):847–853, 2011.

[179] Y. Gorlin, B. Lassalle-Kaiser, J. D. Benck, S. Gul, S. M. Webb, V. K. Yachandra, J. Yano, and T. F. Jaramillo. In Situ X-Ray Absorption Spectroscopy Investigation of a Bifunctional Manganese Oxide Catalyst with High Activity for Electrochemical Water Oxidation and Oxygen Reduction. *J. Am. Chem. Soc.*, 135(23):8525–8534, 2013.

[180] T. W. Hansen, J. B. Wagner, P. L. Hansen, S. Dahl, H. Topsøe, and C. J. H. Jacobsen. Atomic-Resolution In Situ Transmission Electron Microscopy of a Promoter of a Heterogeneous Catalyst. *Science*, 294(5546):1508–1510, 2001.

[181] P. Schattschneider and B. Jouffrey. Plasmons and Related Excitations. In *Energy-Filtering Transmission Electron Microscopy*, pages 151–224. Springer, 1995.

[182] C.-K. Yang, Y. Yamazaki, A. Aydin, and S. M. Haile. Thermodynamic and Kinetic Assessments of Strontium-Doped Lanthanum Manganite Perovskites for Two-Step Thermochemical Water Splitting. *J. Mater. Chem. A*, 2(33):13612–13623, 2014.

[183] M. M. Najafpour, T. Ehrenberg, M. Wiechen, and P. Kurz. Calcium Manganese (III) Oxides ($CaMn_2O_4$ x H_2O) as Biomimetic Oxygen-Evolving Catalysts. *Angew. Chem.*, 49(12):2233–2237, 2010.

[184] Y. Matsumoto and E. Sato. Electrocatalytic Properties of Transition Metal Oxides for Oxygen Evolution Reaction. *Mater. Chem. Phys.*, 14(5):397–426, 1986.

[185] S. Raabe, D. Mierwaldt, J. Ciston, M. Uijttewaal, H. Stein, J. Hoffmann, Y. Zhu, P. Blöchl, and Ch. Jooss. In Situ Electrochemical Electron Microscopy Study of Oxygen Evolution Activity of Doped Manganite Perovskites. *Adv. Funct. Mater.*, 22(16):3378–3388, 2012.

[186] J.-C. Grenier, M. Pouchard, and A. Wattiaux. Electrochemical Synthesis: Oxygen Intercalation. *Current Opinion in Solid State and Materials Science*, 1(2):233–240, 1996.

[187] L. Samet, D. Imhoff, J.-L. Maurice, J.-P. Contour, A. Gloter, T. Manoubi, A. Fert, and C. Colliex. EELS Study of Interfaces in Magnetoresistive LSMO/STO/LSMO Tunnel Junctions. *Eur. Phys. J. B*, 34(2):179–192, 2003.

[188] M. Toth, M. R. Phillips, J. P. Craven, B. L. Thiel, and A. M. Donald. Electric Fields Produced by Electron Irradiation of Iinsulators in a Low Vacuum Environment. *J. Appl. Phys.*, 91(7):4492–4499, 2002.

[189] M. S. Chung and T. E. Everhart. Simple Calculation of Energy Distribution of Low-Energy Secondary Electrons Emitted from Metals under Electron Bombardment. *J. Appl. Phys.*, 45(2):707–709, 1974.

[190] J. Cazaux. Material Contrast in SEM: Fermi Energy and Work Function Effects. *Ultramicroscopy*, 110(3):242–253, 2010.

[191] B. L. Henke, J. Liesegang, and S. D. Smith. Soft-x-Ray-Induced Secondary-Electron Emission from Semiconductors and Insulators: Models and Measurements. *Phys. Rev. B*, 19(6):3004, 1979.

[192] H. Kathrein and F. Freund. Electrical Conductivity of Magnesium Oxide Single Crystal below 1200 K. *J. Phys. Chem. Solids*, 44(3):177–186, 1983.

[193] http://dbshino.nifs.ac.jp.

[194] T. Riedl, T. Gemming, W. Gruner, J. Acker, and K. Wetzig. Determination of Manganese Valency in $La_{1-x}Sr_xMnO_3$ using ELNES in the (S)TEM. *Micron*, 38(3):224–230, 2007.

[195] J. Kim and A. Manthiram. A Manganese Oxyiodide Cathode for Rechargeable Lithium Batteries. *Nature*, 390(6657):265–267, 1997.

[196] A. M Donald. The Use of Environmental Scanning Electron Microscopy for Imaging Wet and Insulating Materials. *Nat. Mater.*, 2(8):511–516, 2003.

[197] S. A. Wight. Experimental Data and Model Simulations of Beam Spread in the Environmental Scanning Electron Microscope. *Scanning*, 23(5):320–327, 2001.

[198] J. H. Paterson and O. L. Krivanek. ELNES of 3*d* Transition-Metal Oxides: II. Variations with Oxidation State and Ccrystal Structure. *Ultramicroscopy*, 32(4):319–325, 1990.

[199] H. Kurata and Ch. Colliex. Electron-Eenergy-Loss Core-Eedge Structures in Manganese Oxides. *Phys. Rev. B*, 48(4):2102, 1993.

[200] W. Luo, M. Varela, J. Tao, S. J. Pennycook, and S. T. Pantelides. Electronic and Ccrystal-Field Eeffects in the Fine Structure of Electron Energy-Loss Spectra of Manganites. *Phys. Rev. B*, 79(5):052405, 2009.

[201] M. J. Montenegro, T. Lippert, S. Müller, A. Weidenkaff, P. R. Willmott, and A. Wokaun. Pulsed Laser Deposition of Electrochemically Active Perovskite Films. *Appl. Surf. Sci.*, 197:505–511, 2002.

[202] M. J. Montenegro, M. Döbeli, T. Lippert, S. Müller, B. Schnyder, A. Weidenkaff, P. R. Willmott, and A. Wokaun. Pulsed Laser Deposition of $La_{0.6}Ca_{0.4}CoO_3$ (LCCO) Films. A Promising Metal-Oxide Catalyst for Air Based Batteries. *Phys. Chem. Chem. Phys.*, 4(12):2799–2805, 2002.

[203] F. M. F. de Groot, J. C. Fuggle, B. T. Thole, and G. A. Sawatzky. L2,3 X-Ray Absorption Spectra of d_0 Compounds: K^+, Ca^{2+}, Sc^{3+} and Ti^{4+} in O_h Symmetry. *Phys. Rev. B*, 41(928):152, 1990.

[204] M. T. Costello and M. Kasrai. Study of Surface Films of Overbased Sulfonates and Sulfurized Olefins by X-Ray Absorption Near Edge Structure (XANES) spectroscopy. *Tribology Letters*, 24(2):163–169, 2006.

[205] H. Lichte and M. Lehmann. Electron Holography - Basics and Applications. *Rep. Prog. Phys.*, 71(1):016102, 2008.

[206] M. P. Seah and W. A. Dench. Quantitative Electron Spectroscopy of Surfaces: a Standard Data Base for Electron Inelastic Mean Free Paths in Solids. *Surface and interface analysis*, 1(1):2–11, 1979.

[207] Y. Itikawa and N. Mason. Cross Sections for Electron Collisions with Water Molecules. *J. Phys. Chem. Ref. Data*, 34(1):1–22, 2005.

[208] M. Toth, B. L. Thiel, and A. M. Donald. On the Role of Electron-Ion Recombination in Low Vvacuum Scanning Electron Microscopy. *J. Microsc.*, 205(1):86–95, 2002.

[209] E. Castanier and C. Noguera. Oxygen Vacancies on MgO (100). *Surf. Sci.*, 364(1):1–16, 1996.

[210] G.B. Arfken, H.J. Weber, and F. Harris. *Mathematical Methods for Physicists*. 5th Edition Academic Press, 2000.

[211] S. Carter, A. Selcuk, R. J. Chater, J. Kajda, J. A. Kilner, and B. C. H. Steele. Oxygen Transport in Selected Non-Stoichiometric Perovskite-Structure Oxides. *Solid State Ionics*, 53:597–605, 1992.

[212] N. Folchert. Untersuchung Photoelektrischer Effekte in $Pr_{1-x}Ca_xMnO_3$ und $La_{1-x}Sr_xMnO_3$. Master's thesis, Institut für Materialphysik, Universität Göttingen, 2014.

[213] K. Stoerzinger, L. Qiao, M. D. Biegalski, H. M. Christen, and Y. Shao-Horn. Enhanced Oxygen Evolution Activity of IrO_2 and RuO_2 (100) Surfaces. *Journal of Physical Chemistry*, 5, 2014.

[214] A. Ramírez, P. Hillebrand, D. Stellmach, M. M. May, P. Bogdanoff, and S. Fiechter. Evaluation of MnO_x, Mn_2O_3, and Mn_3O_4 Electrodeposited Films for the Oxygen Evolution Reaction of Water. *The Journal of Physical Chemistry C*, 118(26):14073–14081, 2014.

[215] A. Reller, J. M. Thomas, D. A. Jefferson, and M. K. Uppal. Superstructures Formed by the Ordering of Vacancies in a Selective Oxidation Catalyst: Grossly Defective $CaMnO_3$. In *Proceedings of the Royal Society of London A: Mathematical, Physical and Engineering Sciences*, volume 394, pages 223–241. The Royal Society, 1984.

[216] K. R Poeppelmeier, M. E. Leonowicz, and J. M. Longo. $CaMnO_{2.5}$ and $Ca_2MnO_{3.5}$: New Oxygen-Defect Perovskite-Type Oxides. *Journal of Solid State Chemistry*, 44(1):89–98, 1982.

[217] H. S. Horowitz and J. M. Longo. Phase Relations in the Ca-Mn-O System. *Materials Research Bulletin*, 13(12):1359–1369, 1978.

[218] L. V. Kulik, B. Epel, W. Lubitz, and J. Messinger. Electronic Structure of the Mn4O x Ca cluster in the S0 and S2 States of the Oxygen-Evolving Complex of Photosystem II based on Pulse 55Mn-ENDOR and EPR Spectroscopy. *Journal of the American Chemical Society*, 129(44):13421–13435, 2007.

[219] H. Dau, A. Grundmeier, P. Loja, and M. Haumann. On the Structure of the Manganese Complex of Photosystem II: Extended-Range EXAFS Data and Specific Atomic-Resolution Models for Four S-states. *Philosophical Transactions of the Royal Society B: Biological Sciences*, 363(1494):1237–1244, 2008.

[220] P. E. M. Siegbahn. Water Oxidation Mechanism in Photosystem II, Including Oxidations, Proton Release Pathways, O-O Bond Formation and O_2 Release. *Biochimica et Biophysica Acta (BBA)-Bioenergetics*, 1827(8):1003–1019, 2013.

[221] C. Jooss, S. Mildner, M. Beleggia, D. Mierwaldt, and V. Roddatis. ETEM Studies of Electrodes and Electro-Catalysts. In J. B. Wagner and T. W. Hansen, editors, *Controlled Atmosphere Transmission Electron Microscopy - Principles and Practice*. Springer, 2015, accepted.

Author Contributions

This thesis is composed of three articles:

1. *Temperature and Doping Dependent Optical Absorption in the Small Polaron System* $Pr_{1-x}Ca_xMnO_3$, accepted for publication in Phys. Rev. B (2015)- Chapter 2

2. *In situ electrochemical electron microscopy study of oxygen evolution activity of doped manganite perovskites*, Adv. Funct. Mater. **22** (2012), DOI: 10.1002/adfm.201103173 - Chapter 3

3. *Environmental TEM Study of Electron Beam Induced Electrochemistry of* $Pr_{0.64}Ca_{0.36}MnO_3$ *Catalysts for Oxygen Evolution*, J. Phys. Chem. C **119** (2015), DOI:10.1021/jp511628c - Chapter 4

The latter two articles are published in the peer-reviewed journals *Avanced Functional Materials* (chapter 3) and *Journal of Physical Chemistry C* (chapter 4)[1]. The first article compiled in the chapter 2 has been accepted for publication in *Physical Review B* on June 12, 2015 and is currently under production. All articles present original research by the author.
A pronounced part of the presented results, particularly in the articles 2 and 3, are produced at external laboratories (Brookhaven National Laboratory, the synchrotron radiation facility BESSY II Berlin and the Technical University of Denmark) in collaboration with the named coauthors. In the following paragraph the author contributions to the respective article will be disclosed.

In *article 1* (chapter 2) the data collection, fitting and analysis of the optical absorption and the temperature dependent resistivity data were conducted by the author at the Max-Plack Institute for Biophysical Chemistry under the guidance of Prof. Simone Techert. The studied thin film samples were prepared characterized by the author. Band structure calculations (Fig. 2.9) and input concerning the interpretation of the optical results were provided by Prof. Peter Blöchl. Furthermore, Dr. Jörg Hoffmann, Prof. Christian Jooss and Prof. Peter Blöchl have contributed to the interpretation and understanding of the optical data in the framework of polaron physics as well as the development of the manuscript.

TEM-imaging, diffraction, STEM, EELS and inside-ETEM mass spectrometry and electrical biasing experiments in *article 2* presented in chapter 3 were conducted by Prof. Christian Jooss, Dr. Jim Ciston and the author. Data presented in the Figs. 3.3, 3.4a, 3.5, 3.6, 3.11, 3.15 were measured at the Center for Functional Nanomaterials (CFN) at Brookhaven National Laboratory under guidance of Prof. Yimei Zhu. Analysis of TEM, EELS, EDX and cyclovoltammetry experiments was carried out by the author.

[1] Accordingly, the requirements in the doctoral degree regulations for a cumulative thesis are fulfilled.

Daniel Mierwaldt and Helge Stein prepared the PCMO thin film samples for the cyclovoltammetry measurements and performed the cyclovoltammetry measurements themselves (Figs. 3.1, 3.8). The chronoamperometry data in Fig. 3.9 were produced by Daniel Mierwaldt, who also conducted the in situ XANES experiments (Fig. 3.4b) at the synchrotron radiation facility BESSY II Berlin. Electronic band structure calculations in Fig. 3.12 were carried out by Matthé Uijttewaal and Prof. Peter Blöchl. The manuscript text and figures were developed by the author in collaboration with Prof. Christian Jooss, Dr. Jörg Hoffmann as well as Daniel Mierwaldt.
Additional researchers like Dr. Rosa Arrigo, Dr. Axel Knop-Gerricke, Dr. Peter Bogdanoff and Prof. Sebastian Fiechter contributed with ancillary experimental support to article 2. Thus, they are not listed as coauthors but acknowledged within in the article 2.

The conduction of the (S)TEM imaging, diffraction, EELS, EDX and electron holography experiments shown in *article 3* (chapter 4) was carried out by the author. The TEM specimen were prepared by the author including previous thin film sample preparation and pre-characterization. Production of ETEM and EELS data (Figs.4.2, 4.3, 4.9a) was performed at the Center for Electron Nanoscopy (CEN), Technical University of Denmark, where the electron microscope was operated by Dr. Thomas W. Hansen, Prof. Jakob B. Wagner under supervision of the author. Off-axis electron holography experiments (Fig. 4.6), likewise performed at the CEN (TU Denmark), were conducted by the author together with Dr. Takeshi Kasama, Dr. Sadegh Yazdi and Prof. Marco Beleggia. Prof. Marco Beleggia also carried out the electrostatic modeling of the electron phase images presented in Fig. 4.6 and Sec. 4.6.8 with the support of Prof. Christian Jooss and the author. Theoretical modeling of beam induced potentials on the basis of the secondary electron yield (Secs. 4.6.4 and 4.6.6) was elaborated by the author in collaboration with Prof. Marco Beleggia and Prof. Christian Jooss. The electrical biasing experiments in Sec. 4.6.7 were performed by Daniel Mierwaldt and the author. The TEM and EELS data shown in the Figs. 4.4, 4.8, 4.9b,c and 4.13 were produced at the CFN (Brookhaven Nat. Lab.) by Dr. Jim Ciston and the author with the support from Prof. Yimei Zhu. Daniel Mierwaldt carried out the cyclovoltammetry measurement illustrated in Fig. 4.1. The manuscript was prepared by the author in collaboration with Prof. Christian Jooss, Prof. Marco Beleggia and Daniel Mierwaldt.

The photoresistance measurements presented in the Appendix are conducted and analyzed by Nils Folchert and the author.

Acknowledgments

Many colleagues at the Institute for Materials Science, relatives and friends, who I would like to express my gratitude, have been supporting the completion and success of the present thesis.
First of all, I would like to name Prof. Christian Jooss who supervised my doctoral education with pronounced commitment and the right proportion of guidance, individual responsibility and confidence. I am very grateful for the inspirational discussions and his appreciation as well as his continual patience and support of my doctoral study with children during the past years.
I also thank Prof. Simone Techert for her appreciation and the numerous encouraging and interesting discussions from the chemical point of view.
Furthermore, my thanks go to Prof. Michael Seibt who has kindly agreed to be the co-referee of this thesis.
Dr. Jörg Hoffmann provided substantial support and enlightened me about polarons in PCMO by comprehensible reports and discussions about polaron physics and transport.
I greatly appreciate the conversations with Prof. Peter Blöchl who enriched my understanding of the optical absorption in PCMO by giving me new insights into the relation between polaron physics and the electronic band structure of PCMO.
Moreover, I would like to express my thanks to the current and former PhD, master and bachelor students of my working group for contributing to a comfortable working atmosphere with humor and exciting philosophical conversations. In particular, I want to mention Daniel Mierwaldt, Jonas Norpoth, Malte Scherff, Björn-Uwe Meyer and Bruno Jasper for numerous exciting hours at the TEM. Notably, the collaboration with Daniel Mierwaldt in (biasing and analytical) ETEM experiments has generated important results incorporated in chapter 3. I thank Nils Folchert for the pleasant and fruitful collaboration concerning the time-dependent photoresistance experiments.
I also want to honor the generous willingness and sacrifice of my parents Renate and Bernd Raabe as well as my stepparents Angelika and Burkhard Mildner to take care of my children at any day or night time and support my work in every situation.
Last but not least, I am so thankful to my husband Thomas and my children Lilli and Tim for keeping my balance, demanding me in family issues and reminding me of the life beside the PhD work.

I also thank the DFG for the financial support.